An analysis of cryovolcano plumes on Enceladus by light scattering and polarimetry

by

Claudia Domenica Morello

B.S., Embry-Riddle Aeronautical University, 2018

AN ABSTRACT OF A DISSERTATION

submitted in partial fulfillment of the requirements for the degree

DOCTOR OF PHILOSOPHY

Department of Physics
College of Arts and Sciences

KANSAS STATE UNIVERSITY
Manhattan, Kansas

2024

Abstract

Enceladus, the sixth largest moon of Saturn, is known to be a geologically active icy body. Observations by NASA's Cassini spacecraft show that Enceladus has cryovolcanoes on its south pole as well as a global subsurface ocean hidden beneath its frozen crust. Photographs from Cassini during flybys of Enceladus document Enceladus's surface and the cryovolcano plumes. It is known that larger particles ejected from the cryovolcanoes deposit on the surface, while smaller particles escape into Saturn's E-ring. Cassini observations of the sunlight scattered by the plume particles on the surface may provide information about the plume composition and potentially the dynamics of the ocean below. This work removes the coupling between orbital position and scattered plume intensity to use more of the Cassini intensity data than ever before and, with the Q-space method, shows that the particles are on average greater than 2 μm in radius and likely non-spherical. This work also presents Enceladus' surface disk-averaged degree of linear polarization (DoLP). The plume intensities and surface DoLP are compared to spherical, spheroidal, cylindrical, and hexagonal water ice particles simulated by light scattering codes Amsterdam Discrete Dipole Approximation (ADDA) and T-Matrix for both single scattering and using a multiple-scattering approximation. The Pearson correlation coefficient is used to quantify the fit of each morphology to the Cassini data in the clear CLR (611 nm), GRN (569 nm), and MT2 (727 nm) wavelength filters and to refine the simulations. The intensity analysis of Enceladus' plumes and the polarization of Enceladus' surface imply the particles are likely non-spherical, and possibly occur in a size distribution with a large standard deviation and near a mean of 2 μm in radius.

An analysis of cryovolcano plumes on Enceladus by light scattering and polarimetry

by

Claudia Domenica Morello

B.S., Embry-Riddle Aeronautical University, 2018

A DISSERTATION

submitted in partial fulfillment of the requirements for the degree

DOCTOR OF PHILOSOPHY

Department of Physics
College of Arts and Sciences

KANSAS STATE UNIVERSITY
Manhattan, Kansas

2024

Approved by:

Major Professor
Dr. Matthew J. Berg

Copyright

Abstract

Enceladus, the sixth largest moon of Saturn, is known to be a geologically active icy body. Observations by NASA's Cassini spacecraft show that Enceladus has cryovolcanoes on its south pole as well as a global subsurface ocean hidden beneath its frozen crust. Photographs from Cassini during flybys of Enceladus document Enceladus's surface and the cryovolcano plumes. It is known that larger particles ejected from the cryovolcanoes deposit on the surface, while smaller particles escape into Saturn's E-ring. Cassini observations of the sunlight scattered by the plume particles on the surface may provide information about the plume composition and potentially the dynamics of the ocean below. This work removes the coupling between orbital position and scattered plume intensity to use more of the Cassini intensity data than ever before and, with the Q-space method, shows that the particles are on average greater than 2 μm in radius and likely non-spherical. This work also presents Enceladus' surface disk-averaged degree of linear polarization (DoLP). The plume intensities and surface DoLP are compared to spherical, spheroidal, cylindrical, and hexagonal water ice particles simulated by light scattering codes Amsterdam Discrete Dipole Approximation (ADDA) and T-Matrix for both single scattering and using a multiple-scattering approximation. The Pearson correlation coefficient is used to quantify the fit of each morphology to the Cassini data in the clear CLR (611 nm), GRN (569 nm), and MT2 (727 nm) wavelength filters and to refine the simulations. The intensity analysis of Enceladus' plumes and the polarization of Enceladus' surface imply the particles are likely non-spherical, and possibly occur in a size distribution with a large standard deviation and near a mean of 2 μm in radius.

Table of Contents

List of Figures

List of Tables

Acknowledgements

This research was supported by the US Air Force Office of Scientific Research grants FA9550-19-0078 and FA9550-21-1-0339, the National Science Foundation grant 2107715, and the US Army Research Office grant W911NF2120053. I would like to acknowledge my advisor Dr. Matthew Berg, as well as the members of my committee, Dr. Matthew Brueseke, Dr. Chris Sorensen, and Dr. Gary Wysin. I would also like to acknowledge Dr. Luke Dones, Dr. Justin Maughan, Dr. Gorden Videen, Dr. Bob West, and Dr. Evgenij Zubko for all their help and support.

Dedication

This dissertation is dedicated to every person who has ever supported me and my scientific goals.

Thank you.

Chapter 1 - Introduction to Light Scattering

Light is important for everything relating to life as we know it, and because of this, it has been the subject of interest for millennia. Ancient civilizations knew the power of the sun to grow crops or dry out a city and worshipped it accordingly. They used it to tell time, predict the future, and calculate the size of the earth [1]. Sunlight is studied, even now thousands of years later, in this paper to explain celestial phenomena.

Scattering is a convenient use of light because it can be seen in many situations. With it, we can determine shapes, sizes, and compositions of the particles we want to study. Every sunset is an example of light scattering, as is every foggy drive. This dissertation will discuss how light scattering works and will be used to study particles on Saturn's moon, Enceladus.

When light interacts with a phase boundary, such as the surface of a particle in the air, several different processes can occur, including reflection, refraction, and diffraction. When the boundary encloses a discrete volume or when it has structure within itself, these processes are considered "scattering". This is why analysis of the scattered light can help reveal the properties of the structure [2].

1.1 Basics of Light

To use light scattering, one must understand what light is and how it works. Light in free space is a transverse electromagnetic wave that propagates in a direction perpendicular to the plane of vibration, i.e. the plane in which the electric and magnetic waves oscillate. It is both parts electric field and magnetic field, and the interactions between those fields and matter are the subjects of interest. A beam of light will propagate unaffected through a vacuum at a phase velocity of 3×10^8 m/s, or the "speed limit of the universe".

When matter is placed into the path of the beam of light, the light can slow down through it, bounce off, or both. Light is made up of photons, so one might think that scattering is only due to the photons bouncing off the particle in question. However, the particle wave duality of light cannot be ignored in these cases due to interference. Light is a wave with a frequency, wavelength, and a phase, all of which come into play.

As matter contains charges, the electromagnetic wave will interact with the charges and cause them to oscillate. Oscillations cause continuous acceleration and thus cause the charges to radiate. It would be much simpler if only the fields from the incident beam cause the charges to oscillate, but the radiated fields from all the other charges within the particle do as well. The scattered field is therefore the sum of all these radiated fields. Some of the energy from the incident beam may also be converted into other forms such as thermal energy, which is known as absorption. Emission occurs as a complementary process to absorption and is when matter releases thermal energy. In this work, emission is neglected because it has a very small effect and occurs at different wavelengths than the ones measured. The total amount of energy removed from the incident beam by either scattering or absorption is referred to as extinction [3].

1.2 Principles of Scattering

As previously mentioned, light is a combination of electric and magnetic fields. Every electromagnetic wave must obey Maxwell's Equations [4]. In a current and charge free space they are as follows:

Gauss' Law for Electric Fields:

$$\nabla \cdot \mathbf{E} = 0 \qquad (1.1)$$

Gauss' Law for Magnetic fields:

$$\nabla \cdot \mathbf{B} = 0 \qquad (1.2)$$

Faraday's Law:

$$\nabla \times \mathbf{E} = -\frac{\partial \mathbf{B}}{\partial t} \quad (1.3)$$

Ampere's Law:

$$\nabla \times \mathbf{B} = \mu_0 \varepsilon_0 \frac{\partial \mathbf{E}}{\partial t} \quad (1.4)$$

Where μ_0 and ε_0 are the permeability and permittivity of free space respectively and are related to the speed of light:

$$c = \frac{1}{\sqrt{\mu_0 \varepsilon_0}} = 299792458 \, \frac{\mathrm{m}}{\mathrm{s}} \quad (1.5)$$

The electromagnetic wave equation is a second order, partial differential equation that describes the propagation of electromagnetic waves. It is a three-dimensional form of the wave equation for travelling or standing waves in standard physics. The homogenous form for the **E** and **B** fields is:

$$\left(\nabla^2 - \frac{1}{c^2}\frac{\partial^2}{\partial t^2}\right)\mathbf{E}(\mathbf{r}, t) = 0 \qquad (1.6)$$

$$\left(\nabla^2 - \frac{1}{c^2}\frac{\partial^2}{\partial t^2}\right)\mathbf{B}(\mathbf{r}, t) = 0 \qquad (1.7)$$

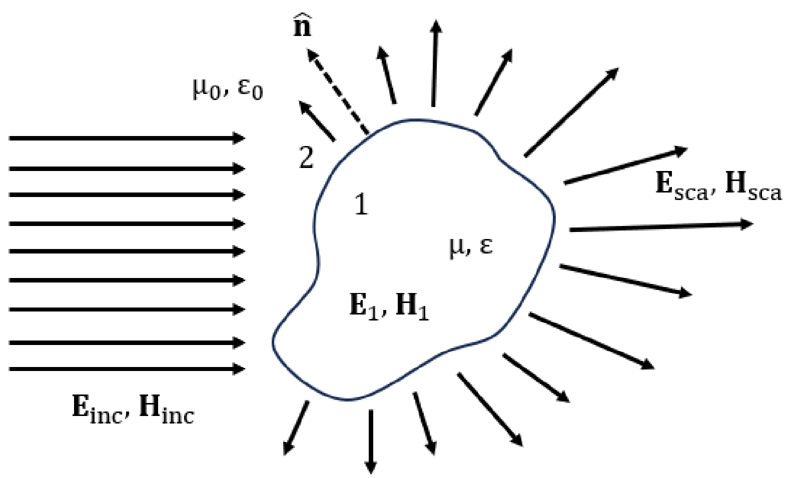

Figure 1.1**.** Geometry of scattering of a particle showing the incident (inc) and scattered (sca) fields, the two locations (1 and 2) and the permittivity and permeability of free space.

For an arbitrary particle illuminated by monochomatic, arbitarily polarized light, the general formulation of the scattering is as follows. This work follows the derivation from [3], and only considers plane harmonic waves as opposed to the Fourier components of an arbitrary field. This simplification will be explained later in this section. For the contet of this problem, it is more convenient to use

$$\mathbf{H} = \frac{\mathbf{B}}{\mu} \qquad (1.8)$$

as opposed to **B** fields.

To explain the electromagentic scattering properties of a particle, it is necessary to consider the electric and magenetic fields at all points inside and outside of the particle. The external electric field is the sum of the incident and scattered electric fieds, and same for the magnetic field.

$$\mathbf{E}_2 = \mathbf{E}_{\text{inc}} + \mathbf{E}_{\text{sca}} \qquad (1.9)$$

$$\mathbf{H}_2 = \mathbf{H}_{\text{inc}} + \mathbf{H}_{\text{sca}} \qquad (1.10)$$

And as each field is an electromagnetic wave, they can be expressed as exponentials.

$$\mathbf{E}_{\text{inc}} = \mathbf{E}_0 \exp(i\mathbf{k} \cdot \mathbf{x} - i\omega t) \quad (1.11)$$

$$\mathbf{H}_{\text{inc}} = \mathbf{H}_0 \exp(i\mathbf{k} \cdot \mathbf{x} - i\omega t) \quad (1.12)$$

Following the notation of [3], the fields inside and outside will be referred to as (1) and (2) for their respective regions. The incident fields $(\mathbf{E}_{\text{inc}}, \mathbf{H}_{\text{inc}})$ give rise to the fields $(\mathbf{E}_1, \mathbf{H}_1)$ inside the particle and $(\mathbf{E}_{\text{sca}}, \mathbf{H}_{\text{sca}})$ in the surrounding medium.

The fields obey the Maxwell Equations at all points where μ and ε are continuous. If we assume a time dependence of $\exp(-i\omega t)$ for all fields, then we can ignore it and combine Eqs. (1.1)-(1.12) to derive a more convenient and more general version of the Maxwell Equations for this problem:

$$\nabla \cdot \mathbf{E} = 0 \qquad (1.13)$$

$$\nabla \cdot \mathbf{H} = 0 \qquad (1.14)$$

$$\nabla \times \mathbf{E} = i\omega\mu\mathbf{H} \qquad (1.15)$$

$$\nabla \times \mathbf{H} = -i\omega\varepsilon\mathbf{E} \qquad (1.16)$$

The curls of Faraday's and Ampere's Laws are:

$$\nabla \times (\nabla \times \mathbf{E}) = i\omega\mu\nabla \times \mathbf{H} = \omega^2\varepsilon\mu\mathbf{E} \quad (1.17)$$

$$\nabla \times (\nabla \times \mathbf{H}) = i\omega\mu\nabla \times \mathbf{E} = \omega^2\varepsilon\mu\mathbf{H} \quad (1.18)$$

Using the following vectory identity (Eq. (119)) on Eq. (1.17) and (1.18) to transform the curl into a gradient and divergence:

$$\nabla \times (\nabla \times \mathbf{A}) = \nabla(\nabla \cdot \mathbf{A}) - \nabla \cdot (\nabla\mathbf{A}), \quad (1.19)$$

and using the first two Maxwell Equations:

$$\nabla \cdot \mathbf{E} = 0 \qquad (1.1)$$

$$\nabla \cdot \mathbf{H} = 0\ , \qquad (1.14)$$

gives:

$$(\nabla^2 + k^2)\mathbf{E} = 0 \qquad (1.20)$$

$$(\nabla^2 + k^2)\mathbf{H} = 0 \qquad (1.21)$$

as the first term on the right goes to 0. Here, $\nabla^2 = \vec{\nabla} \cdot \vec{\nabla}$ and $k = \omega\varepsilon\mu$. This means $\mathbf{E}$ and $\mathbf{H}$ satisfy the vector wave equations.

The electromagnetic field must satisfy the Maxwell Equations at all points where μ and ε are continuous. The boundary of the particle (from region 1 to region 2) is a discontinuity, so boundary conditions are needed.

$$[\mathbf{E}_2(\mathbf{x}) - \mathbf{E}_1(\mathbf{x})] \times \hat{\mathbf{n}} = 0\ , \qquad (1.22)$$

$$[\mathbf{H}_2(\mathbf{x}) - \mathbf{H}_1(\mathbf{x})] \times \hat{\mathbf{n}} = 0\ , \qquad (1.23)$$

where $\hat{\boldsymbol{n}}$ is the outward directed normal to the surface of the particle and *x* is on the surface S of the particle. A simple way to take the discontinuity into account is to use the conservation of energy. If we enclose the boundary in a closed surface A, still with outward normal $\hat{n}$, then the rate at which electromagnetic energy is transferred near A in region 1 is:

$$\int \mathbf{S}_1 \cdot \hat{\mathbf{n}}\, dA = \int \hat{\mathbf{n}} \cdot (\boldsymbol{E}_1 \times \mathbf{H}_1)\ dA\ , \quad (1.24)$$

and near A in region 2:

$$\int \mathbf{S}_2 \cdot \hat{\mathbf{n}}\, dA = \int \hat{\mathbf{n}} \cdot (\mathbf{E_2} \times \mathbf{H}_2)\ dA\ , \quad (1.25)$$

where $\boldsymbol{S}_1$ and $\boldsymbol{S}_2$ are the time-averaged Poynting vectors (the directional energy flux of an electromagnetic field) in each region, generally written as:

$$\mathbf{S} = \mathbf{E} \times \mathbf{H} \qquad (1.26)$$

Imposing the boundary conditions means that

$$\mathbf{E}_2 \times \hat{\mathbf{n}} = \mathbf{E}_1 \times \hat{\mathbf{n}} \qquad (1.27)$$

$$\mathbf{H}_2 \times \hat{\mathbf{n}} = \mathbf{H}_1 \times \hat{\mathbf{n}} \qquad (1.28)$$

so Eq. (1.24) - (1.25) can be written as

$$\int \mathbf{S}_1 \cdot \hat{\mathbf{n}}\, dA = \int \hat{\mathbf{n}} \cdot (\mathbf{E}_1 \times \mathbf{H}_1)\ dA = \int \hat{\mathbf{n}} \cdot (\mathbf{E}_2 \times \mathbf{H}_2)\ dA \qquad (1.29)$$

$$\int \mathbf{S}_2 \cdot \hat{\mathbf{n}}\, dA = \int \hat{\mathbf{n}} \cdot (\mathbf{E}_2 \times \mathbf{H}_2)\ dA = \int \hat{\mathbf{n}} \cdot (\mathbf{E}_1 \times \mathbf{H}_1)\ dA\ , \ (1.30)$$

meaning that

$$\int \mathbf{S}_1 \cdot \hat{\mathbf{n}}\, dA = \int \mathbf{S}_2 \cdot \hat{\mathbf{n}}\, dA\ , \qquad (1.31)$$

or the requirement for tangential components of the electromagetic field being continuous across a boundary is a sufficient condition for energy conservation across the boundary as well.

To fully explain scattering, we need to derive solutions to the Maxwell equations inside and outside the particle that satisfy the boundary conditions at S. If the incident electromagnetic field is an arbitrary field that can be Fourier analyzed into a superposition of plane harmonic waves, then the solution can be constructed by superimposing fundamental solutions of waves as well. This can be done because both the Maxwell equations and the boundary conditions are linear.

If two fields are solutions to the field equations and boundary conditions, then their sum is, too. Therefore:

$$(\mathbf{E_2} - \mathbf{E_1}) \times \hat{\mathbf{n}} = 0 \quad (1.32)$$

and not just at $\boldsymbol{x}$ on S in Eq. 1.31 (the boundary conditions).

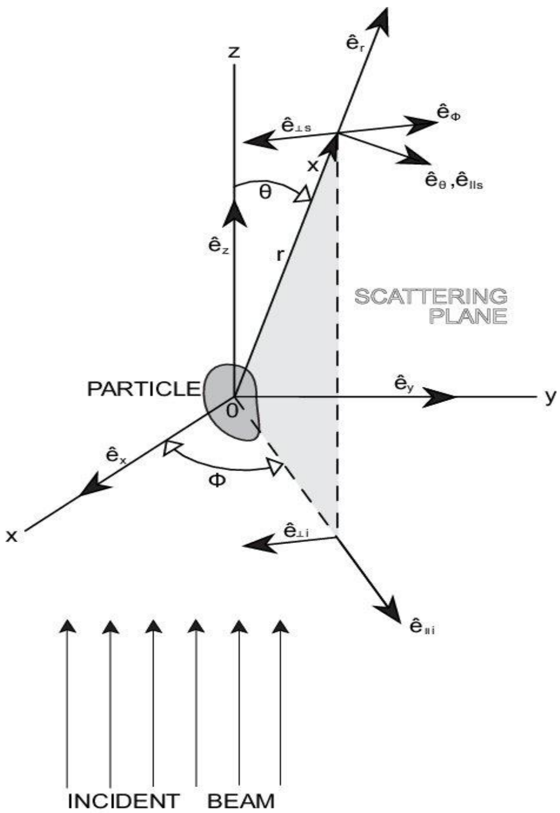

Figure 1.2**.** Scattering from a particle showing the geometry of the system and the definition of the scattering plane. The incident beam defines the positive *z*-direction. [3], [5]

Common scattering convention has the incident light propagating in the *z*-direction, so that it defines the *z*-axis. Any point inside the particle is taken to be the origin. The scattering direction $\hat{\boldsymbol{e}}_r$ and the forward direction $\hat{\boldsymbol{e}}_z$ define the scattering plane. The azimuthal angle ϕ uniquely determines the scattering plane except when $\hat{\boldsymbol{e}}_r = \pm\hat{\boldsymbol{e}}_z$. In that case, the scattering plane is any plane containing the *z*-axis. To make the scattering geometry simpler, the incident electric field $\boldsymbol{E}_{\text{inc}}$ is normally split into components that are parallel and perpendicular to the scattering plane, $\vec{E}_{\parallel\text{inc}}$ and $\vec{E}_{\perp\text{inc}}$, respectively. To be more explicit:

$$\mathbf{E}_{\text{inc}} = (E_{\parallel 0}\hat{\boldsymbol{e}}_{\parallel\text{inc}} + \mathrm{E}_{\perp 0}\,\hat{\mathbf{e}}_{\perp\text{inc}})exp\,(ikz - iwt) \qquad (1.33)$$

Assuming the time dependence as before and simplifying gives:

$$\mathbf{E}_{\text{inc}} = E_{\parallel\text{inc}}\hat{\boldsymbol{e}}_{\parallel\text{inc}} + E_{\perp\text{inc}}\,\hat{\boldsymbol{e}}_{\perp\text{inc}} \qquad (1.34)$$

Here, $k = \frac{2\pi n}{\lambda}$, where *n* is the refractive index of the medium surrounding the particle. Also, $\hat{\mathbf{e}}_{\parallel\text{inc}}$, $\hat{\mathbf{e}}_{\perp\text{inc}}$, and $\hat{\boldsymbol{e}}_z$ form an orthonormal basis and follow the right-hand rule. Compared with the original Cartesian coordinates $\hat{\boldsymbol{e}}_x$, $\hat{\boldsymbol{e}}_y$, and $\hat{\boldsymbol{e}}_z$:

$$\hat{\boldsymbol{e}}_{\parallel\text{inc}} = \sin\theta\hat{\boldsymbol{e}}_{\text{x}} + \cos\theta\hat{\mathbf{e}}_{\text{y}} \qquad (1.35)$$

$$\hat{\boldsymbol{e}}_{\perp\text{inc}} = \sin\theta\hat{\boldsymbol{e}}_{\text{x}} - \cos\theta\hat{\boldsymbol{e}}_{\text{y}} \qquad (1.36)$$

And compared with the basis in spherical coordinates, $\hat{\boldsymbol{e}}_r$, $\hat{\boldsymbol{e}}_\theta$, and $\hat{\boldsymbol{e}}_\phi$,

$$\hat{\boldsymbol{e}}_{\parallel\text{inc}} = \sin\theta\hat{\boldsymbol{e}}_{\text{r}} + \cos\theta\hat{\boldsymbol{e}}_{\theta} \qquad (1.37)$$

$$\hat{\boldsymbol{e}}_{\perp\text{inc}} = -\hat{\boldsymbol{e}}_{\phi} \quad (1.38)$$

This means the incident field can be expressed as

$$E_{\parallel\text{inc}} = \cos\phi E_{\text{xinc}} + \sin\phi E_{\text{yinc}} \qquad (1.39)$$

$$E_{\perp\text{inc}} = \sin\phi E_{\text{xinc}} + \cos\phi E_{\text{yinc}} \qquad (1.40)$$

At a very large distance from the origin, we can assume that for the scattered electric field $\hat{\boldsymbol{e}}_r \cdot \mathbf{E}_{\text{sca}} \cong 0$, or that it is transverse in the far field region. Thus, the scattered field can be written similarly to the incident field (Eq. (1.39) - (1.40))

$$\mathbf{E}_{\text{sca}} = E_{\parallel\text{sca}}\hat{\boldsymbol{e}}_{\parallel\text{sca}} + E_{\perp\text{sca}}\,\hat{\boldsymbol{e}}_{\perp\text{sca}} \qquad (1.41)$$

With basis vectors

$$\hat{\boldsymbol{e}}_{\parallel\text{sca}} = \hat{\boldsymbol{e}}_{\theta} \qquad (1.42)$$

$$\hat{\boldsymbol{e}}_{\perp\text{sca}} = -\hat{\boldsymbol{e}}_{\phi} \qquad (1.43)$$

$$\hat{\boldsymbol{e}}_{\perp\text{sca}} \times \hat{\boldsymbol{e}}_{\parallel\text{sca}} = \hat{\boldsymbol{e}}_{\text{r}} \; (1.44)$$

This means that the incident and scattered fields are defined relative to different sets of basis vectors. Since the boundary conditions are linear, the amplitude of the scattered field is a linear function of the amplitude of the incident field. When expressed in matrix form for simplicity, they are called the amplitude matrix:

$$\begin{pmatrix} E_{\parallel \mathrm{sca}} \\ E_{\perp \mathrm{sca}} \end{pmatrix} = \frac{e^{ik(r-z)}}{-ikr} \begin{pmatrix} S_2 & S_3 \\ S_4 & S_1 \end{pmatrix} \begin{pmatrix} E_{\parallel \mathrm{inc}} \\ E_{\perp \mathrm{inc}} \end{pmatrix} \quad (1.45)$$

Some notations use S_{11}, S_{12}, S_{21}, and S_{22} instead, but this notation follows from the convention of [3], so as not to get confused with the scattering matrix elements.

1.3 The Mueller Scattering Matrix

The Mueller scattering matrix is another important scattering quantity and is an output of most scattering codes including ADDA and T-matrix, which are used in this work. Since we now know the incident and scattered electric fields, we can find the Poynting vector at any point inside or outside the particle. However, we only care about the scattering outside the particle. The time averaged Poynting vector in the medium around the particle can be written as the sum of three terms; the incident Poynting vector, the scattered Poynting vector, and the Poynting vector for the interactions between them. Using the notation from Figure 1.1:

$$\mathbf{S} = \frac{1}{2}\mathrm{Re}\{\mathbf{E}_2 \times \mathbf{H}_2^*\} = \mathbf{S}_{\mathrm{inc}} + \mathbf{S}_{\mathrm{sca}} + \mathbf{S}_{\mathrm{ext}}\ , \quad (1.46)$$

where

$$\mathbf{S}_{\mathrm{inc}} = \frac{1}{2}\mathrm{Re}\{\mathbf{E}_{\mathrm{inc}} \times \mathbf{H}_{\mathrm{inc}}^*\} \quad (1.47)$$

$$\mathbf{S}_{\mathrm{sca}} = \frac{1}{2}\mathrm{Re}\{\mathbf{E}_{\mathrm{sca}} \times \mathbf{H}_{\mathrm{sca}}^*\} \quad (1.48)$$

$$\mathbf{S}_{\mathrm{ext}} = \frac{1}{2}\mathrm{Re}\{\mathbf{E}_{\mathrm{inc}} \times \mathbf{H}_{\mathrm{sca}}^* + \mathbf{E}_{\mathrm{sca}} \times \mathbf{H}_{\mathrm{inc}}^*\} \quad (1.49)$$

The Poynting vector accociated with the incident wave, $\mathbf{S}_{\mathrm{inc}}$ is independent of position if the surrounding medium is non-absorbing, which is the case of this work. It is computationally useful to describe the scattering in terms of Stokes parameters [6], or a convenient mathematical representation of the polarization state. It is important to note that the letters *I*,*Q*,*U*, and *V* are not abbreviations. The Stokes parameters for the light scattered by particle are therefore:

$$I_{\mathrm{sca}} = \langle E_{\parallel\mathrm{sca}} E^*_{\parallel\mathrm{sca}} + E_{\perp\mathrm{sca}} E^*_{\perp\mathrm{sca}} \rangle \qquad (1.50)$$

$$Q_{\mathrm{sca}} = \langle E_{\parallel\mathrm{sca}} E^*_{\parallel\mathrm{sca}} - E_{\perp\mathrm{sca}} E^*_{\perp\mathrm{sca}} \rangle \qquad (1.51)$$

$$U_{\mathrm{sca}} = \langle E_{\parallel\mathrm{sca}} E^*_{\perp\mathrm{sca}} + E_{\perp\mathrm{sca}} E^*_{\parallel\mathrm{sca}} \rangle \qquad (1.52)$$

$$V_{\mathrm{sca}} = i\langle E_{\parallel\mathrm{sca}} E^*_{\perp\mathrm{sca}} - E_{\perp\mathrm{sca}} E^*_{\parallel\mathrm{sca}} \rangle \qquad (1.53)$$

Here, the multiplicative factor $\frac{k}{2\pi\mu}$ is omitted. If the Stokes parameters are described as a column vector, the 4x4 Mueller scattering matrix relates the scattered Stokes vector (the Stokes vector describing the wave of scattered light) to the incident Stokes vector (the Stokes vector describing the wave of incident light).

$$\begin{pmatrix} I_{\mathrm{sca}} \\ Q_{\mathrm{sca}} \\ U_{\mathrm{sca}} \\ V_{\mathrm{sca}} \end{pmatrix} = \frac{1}{k^2r^2} \begin{pmatrix} S_{11} & S_{12} & S_{13} & S_{14} \\ S_{21} & S_{22} & S_{23} & S_{24} \\ S_{31} & S_{32} & S_{33} & S_{34} \\ S_{41} & S_{42} & S_{43} & S_{44} \end{pmatrix} \begin{pmatrix} I_{\mathrm{inc}} \\ Q_{\mathrm{inc}} \\ U_{\mathrm{inc}} \\ V_{\mathrm{inc}} \end{pmatrix} \qquad (1.54)$$

The coefficients S_{ij} of the Mueller matrix follow from the elements of the amplitude matrix (Eq. 1.45).

$$S_{11} = \frac{1}{2}(|S_1|^2 + |S_2|^2 + |S_3|^2 + |S_4|^2) \qquad (1.55)$$

$$S_{12} = \frac{1}{2}(|S_2|^2 - |S_1|^2 + |S_4|^2 - |S_3|^2) \qquad (1.56)$$

$$S_{13} = \mathrm{Re}\{S_2S_3^* + S_1S_4^*\} \qquad (1.57)$$

$$S_{14} = \mathrm{Im}\{S_2S_3^* - S_1S_4^*\} \qquad (1.58)$$

$$S_{21} = \frac{1}{2}(|S_2|^2 - |S_1|^2 - |S_4|^2 + |S_3|^2) \qquad (1.59)$$

$$S_{22} = \frac{1}{2}(|S_2|^2 + |S_1|^2 - |S_4|^2 - |S_3|^2) \qquad (1.60)$$

$$S_{23} = \mathrm{Re}\{S_2S_3^* - S_1S_4^*\} \qquad (1.61)$$

$$S_{24} = \mathrm{Im}\{S_2 S_3^* + S_1 S_4^*\} \qquad (1.62)$$

$$S_{31} = \mathrm{Re}\{S_2 S_4^* + S_1 S_3^*\} \qquad (1.63)$$

$$S_{32} = \mathrm{Re}\{S_2 S_4^* - S_1 S_3^*\} \qquad (1.64)$$

$$S_{33} = \mathrm{Re}\{S_1 S_2^* + S_3 S_4^*\} \qquad (1.65)$$

$$S_{34} = \mathrm{Im}\{S_2 S_1^* + S_4 S_3^*\} \qquad (1.66)$$

$$S_{41} = \mathrm{Im}\{S_2^* S_4 + S_3 S_1^*\} \qquad (1.67)$$

$$S_{42} = \mathrm{Im}\{S_2^* S_4 - S_3 S_1^*\} \qquad (1.68)$$

$$S_{43} = \mathrm{Im}\{S_1 S_2^* - S_3 S_4^*\} \qquad (1.69)$$

$$S_{44} = \mathrm{Re}\{S_1 S_2^* - S_3 S_4^*\} \qquad (1.70)$$

In certain cases, the 16 scattering elements in the Mueller matrix are no longer independent. In general, though, all components S_{ij} are independent of ϕ for any particle that is rotationally symmetric about the *z*-axis.

1.4 Polarization

Polarization refers to the orientation of the oscillations of a wave's field. For transverse waves like light, the direction of the oscillation is perpendicular to the motion of the wave. As light is an electromagnetic wave, the polarization direction is defined as the direction of the oscillation of the electric field vector [7]. Sunlight is naturally unpolarized, meaning it contains a mix of polarization directions. The degree of linear polarization (DoLP) is defined as how much of the light is oriented in one direction, and can be expressed in different ways. By definition:

$$\mathrm{DoLP} = \frac{I_\mathrm{p}}{I}, \qquad (1.71)$$

where I_p is the polarized component of the intensity, and *I* is the total intensity.

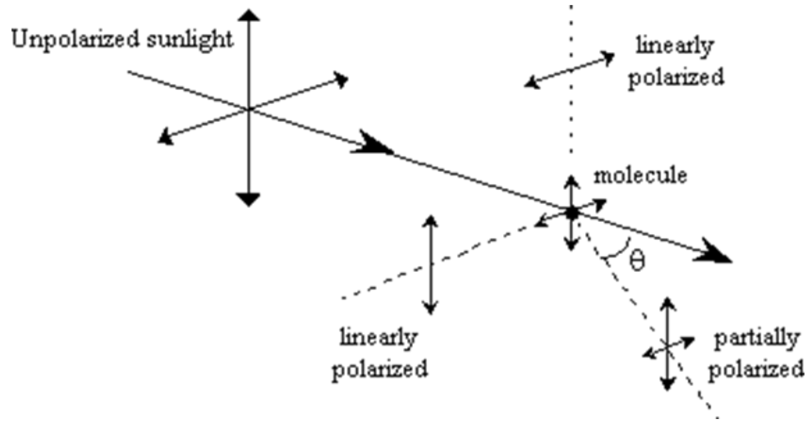

Figure 1.3**.** The geometry of linear polarization caused by unpolarized sunlight scattering off a particle. This image is taken from [8].

If an electromagentic wave propagates in the *z*-direction, it can be described as

$$\mathbf{E} = \mathrm{Re}(\tilde{E}_\mathrm{x})\hat{\boldsymbol{x}} + \mathrm{Re}(\tilde{E}_\mathrm{y})\hat{\boldsymbol{y}}\,, \quad (1.72)$$

where $\tilde{E}_x$, and $\tilde{E}_y$ are the time dependent complex electric field components:

$$\tilde{E}_\mathrm{x} = E_\mathrm{ox}e^{i(kz-\omega t)} \quad (1.73)$$

$$\tilde{E}_\mathrm{y} = E_\mathrm{oy}e^{i(kz-\omega t)}\,, \quad (1.74)$$

and where $k = \frac{2\pi}{\lambda}$ is the wavenumber and ω is the frequency. If the amplitudes $E_\mathrm{ox} \neq 0$, and $E_\mathrm{oy} = 0$, then the light is linearly polarized in the *x*-direction. If $E_\mathrm{ox} = 0$, and $E_\mathrm{oy} \neq 0$, then the light in linearly polarized in the *y*-direction. If both components are equal to each other, then the light is unpolarized. The light can also be circularly or elliptically polarized, but that is unrelated to this paper. This work deals with sunlight, which is naturally unpolarized.

The Stokes parameters for a wave propagating in the *z*-direction like the one described above are then:

$$I = \langle E_\mathrm{0x}^2\rangle - \langle E_\mathrm{0y}^2\rangle \quad (1.75)$$

$$Q = \langle E_\mathrm{0y}^2\rangle - \langle E_\mathrm{0x}^2\rangle \quad (1.76)$$

$$U = \langle 2E_{\mathrm{ox}}E_{\mathrm{oy}}\cos\varepsilon \rangle \quad (1.77)$$

$$V = \langle 2E_{\mathrm{ox}}E_{\mathrm{oy}}\sin\varepsilon \rangle\ , \quad (1.78)$$

where ε is the difference in phase between the *x* and *y* components of the electromagnetic wave [9]. The degree of polarization P is then:

$$P = \frac{\sqrt{Q^2 + U^2 + V^2}}{I}$$

(1.79)

And the degree of linear polarization (DoLP) is then:

$$\mathrm{DoLP} = \frac{\sqrt{Q^2 + U^2}}{I}$$

(1.80)

The DoLP provides novel insight into the particles on Enceladus' surface. Much like for Titan [10] and other planetary bodies, knowing the polarization can hint at certain particle morphologies. For example, small particles (compared to λ) polarize more strongly than larger particles due to the interactions of the internal fields. In addition, spherical particles under unpolarized illumination have a near zero DoLP at small scattering angles due to symmetry [3], [11], [12].

Because a Mueller matrix mathematically explains how an object transforms light via matrix multiplication, polarization simplifies much of the math because the light oscillates in only one direction.

The number of independent elements in the Mueller matrix can be reduced with certain assumptions about the symmetries of the particles within a scattering volume. Reference [13] lists the assumptions, with the main one being that the scattering volume contains particles and their mirror images in equal number and in random orientations, or, the particles in the scattering volume have a plane of symmetry and are randomly oriented. This work uses a single particle, averaged over thousands of orientations to satisfy the assumption. If this is the case, the 16 elements reduce to 6 independent elements.

$$\begin{pmatrix} I_{\text{sca}} \\ Q_{\text{sca}} \\ U_{\text{sca}} \\ V_{\text{sca}} \end{pmatrix} = \frac{1}{k^2r^2} \begin{pmatrix} S_{11} & S_{12} & 0 & 0 \\ S_{12} & S_{22} & 0 & 0 \\ 0 & 0 & S_{33} & S_{34} \\ 0 & 0 & -S_{34} & S_{44} \end{pmatrix} \begin{pmatrix} I_{\text{inc}} \\ Q_{\text{inc}} \\ U_{\text{inc}} \\ V_{\text{inc}} \end{pmatrix}$$

(1.81)

If the incident light is unpolarized, like sunlight, then the DoLP can be expressed in terms of Mueller matix elements as

$$\text{DoLP} = \frac{-S_{12}}{S_{11}}$$

(1.82)

because $I = S_{11}I_{\text{inc}}$ and $Q = -S_{12}I_{\text{inc}}$. This representation of the DoLP is therefore the most useful for this work as it can be easily computed from the light scattering simulations. This simplification works as long as $S_{13} = 0$, which means that the assumption that every particle has a mirror image along the scattering plane and/or every particle has a plane of symmetry has to apply.

1.5 Special Cases

Light scattering is very math intensive because it is based on electromagnetic theory. Fortunately, there are some approximations that can be made for special cases which simplify the calculations. Mie theory is one of those cases.

Mie theory, also known as Lorenz-Mie theory, corresponds to the theory of scattering by a sphere of any size and refractive index. It is an exact solution for all sizes of spheres for all refractive indices and incident wavelengths. Phenomena like rainbows and glories are from Mie scattering. It is named after Gustav Mie who derived it in 1908 for electromagnetism [14], although it was derived non-electromagnetically by Ludvig Lorenz earlier in 1890 [15], [16]. Mie theory is the simplest case of scattering due to spheres' infinite degrees of symmetry. Mie scattering has two limits: 3D diffraction (Rayleigh-Debye-Gans), and 2D diffraction.

The Mie solution is the expansion of an electromagnetic plane wave as discussed in Section 1.1 into spherical vector functions with matching spherical boundary conditions. Mie theory calculates the complex Mie scattering coefficients a_n and b_n, below:

$$a_n = \frac{m\psi_n(mkR)\psi_n'(kR) - m\psi_n(kR)\psi_n'(mkR)}{m\xi_n(mkR)\psi_n'(kR) - \xi_n(xkR)\psi_n'(mkR)}$$

(1.83)

$$b_n = \frac{\psi_n(mkR)\psi_n'(kR) - m\psi_n(kR)\psi_n'(mkR)}{\xi_n(mkR)\psi_n'(kR) - m\xi_n(kR)\psi_n'(mkR)}$$

(1.84)

where *m* is the refractive index, *k* is the wavenumber, *R* is the radius of the sphere. Here, ψ_n and ξ_n are the Riccati-Bessel functions, which come from the spherical Bessel functions of the first and second kind, j_n and y_n, respectively. For more information on the Bessel functions, see [17]. They are related via:

$$\psi_n(x) = xj_n(x) \qquad (1.85)$$

$$\xi_n(x) = xj_n(x) + ixy_n(x) \qquad (1.86)$$

The coefficients describe the multipole expansions of the electric (a_n) and magnetic (b_n) fields of the scattered wave. The dipole term corresponds to $n = 1$, whereas $n = 2$ is the quadrupole term and so on. The complex scattering coefficients are coefficients in different infinite sums that are used for calculating the two, scattering angle dependent, non-zero complex elements of the scattering amplitude matrix S_1 and S_2, as well as the total extinction and scattering cross sections C_{ext} and C_{sca}. The amplitude matrix is the same as in Eq. (1.45) and the elements are:

$$S_1(\theta) = \sum_{n=1}^{\infty} \frac{2n+1}{n(n+1)} \big(a_n \pi_n(\theta) + b_n \tau_n(\theta)\big)$$

(1.87)

$$S_2(\theta) = \sum_{n=1}^{\infty} \frac{2n+1}{n(n+1)} \big(a_n \tau_n(\theta) + b_n \pi_n(\theta)\big)$$

(1.88)

where π_n and τ_n are angle dependent scattering functions as obtained from recursion relations in the infinite sum. They are defined as:

$$\pi_n = \left(\frac{2n-1}{n-1}\cos\theta\right)\pi_{n-1} - \frac{n}{n-1}\pi_{n-2} \quad (1.89)$$

$$\tau_n = n\cos\theta\pi_n - (n+1)\pi_{n-1}\,, \qquad (1.90)$$

starting with $\pi_0 = 0$ and $\pi_1 = 1$. These can also be expressed in terms of Legendre polynomials. The cross sections are related via:

$$C_{\text{ext}} = C_{\text{sca}} + C_{\text{abs}}\,, \quad (1.91)$$

meaning that the total extinction cross section is the sum of the scattering cross section and the absorption cross section. This makes sense because the total amount of extinguished light is the sum of the scattered and absorbed light. From Mie theory:

$$C_{\text{ext}} = \frac{2\pi}{k^2} \sum_{n=1}^{\infty} (2n+1)\text{Re}\{a_n + b_n)$$

(1.92)

$$C_{\text{sca}} = \frac{2\pi}{k^2} \sum_{n=1}^{\infty} (2n+1)\text{Re}\{|a_n|^2 + |b_n|^2)$$

(1.93)

The total absorption cross section can then be found via subtraction once the scattering and extinction cross sections are known.

The amplitude matrix for scattering by a sphere can now be written as Eq. (1.94), with S_3 and S_4 equal to 0, and the other two elements defined above.

$$\begin{pmatrix} E_{\parallel s} \\ E_{\perp s} \end{pmatrix} = \frac{e^{ik(r-z)}}{-ikr} \begin{pmatrix} S_2 & 0 \\ 0 & S_1 \end{pmatrix} \begin{pmatrix} E_{\parallel i} \\ E_{\perp i} \end{pmatrix}$$

(1.94)

Like in Section 1.1, with the amplitude matrix we can derive the Mueller scattering matrix for a sphere of any size.

$$\begin{pmatrix} I_{\text{sca}} \\ Q_{\text{sca}} \\ U_{\text{sca}} \\ V_{\text{sca}} \end{pmatrix} = \frac{1}{k^2 r^2} \begin{pmatrix} S_{11} & S_{12} & 0 & 0 \\ S_{12} & S_{11} & 0 & 0 \\ 0 & 0 & S_{33} & S_{34} \\ 0 & 0 & -S_{34} & S_{33} \end{pmatrix} \begin{pmatrix} I_{\text{inc}} \\ Q_{\text{inc}} \\ U_{\text{inc}} \\ V_{\text{inc}} \end{pmatrix}$$

(1.95)

This Mueller matrix only has four elements,

$$S_{11} = \frac{1}{2}(|S_1|^2 + |S_2|^2) \qquad (1.96)$$

$$S_{12} = \frac{1}{2}(|S_2|^2 - |S_1|^2) \qquad (1.97)$$

$$S_{33} = \frac{1}{2}(S_1 S_2^* + S_2 S_1^*) \qquad (1.98)$$

$$S_{34} = \frac{i}{2}(S_1 S_2^* - S_2 S_1^*) \qquad (1.99)$$

One special case related to size is Rayleigh scattering. Rayleigh scattering happens when particles of any shape are much smaller than the wavelength of light. More explicitly, when $kR \ll 1$. Rayleigh scattering results from the electric polarizability of the particles. The oscillating electric field of an incident light wave acts on the charges within a particle, causing them to oscillate at the same frequency. The particle, therefore, becomes a small radiating dipole whose radiation is then seen as scattered light. In general, the scattered irradiance of any particle that is small compared to the wavelength of the incident light, regardless of shape, is inversely proportional to the wavelength to the fourth power, or:

$$I_{\mathrm{sca}} \sim 1/\lambda^4 \quad (1.100)$$

Because the scattering by small particles is so wavelength dependent, the particles in the atmosphere scatter shorter wavelengths of solar radiation (blue) more strongly. Some of the radiation is absorbed by compounds in the air, which is why the sky is not violet. The particles in this work do not obey the size criteria for Rayleigh scattering.

The second special case relating to size is the geometric optics approximation. To be in the geometric optics regime, the particle size must be much larger than the wavelength of light, or kR>>1. Geometric optics utilizes ray tracing. Light rays incident on a surface can be refracted or reflected according to the Fresnel equations and Snell's law in weakly absorbing media, which simplify a lot of the calculations. More generalized forms of these are required when the refractive index has a large imaginary part [18]. The particles in this work also do not obey the size criteria for the geometric optics regime.

The last special case or approximation is the Rayleigh-Debye-Gans (RDG) limit, which applies to optically soft particles. Optically soft is defined as the particle having a refractive index similar to that of the surrounding medium. A common light scattering quantity, the phase shift parameter ρ, is defined as

$$\rho = 2kR_{\mathrm{Veq}}|m-1| \quad (1.101)$$

where k is the wave number, R_{Veq} is the volume-equivalent radius, and m is the refractive index. When ρ<1, the scattering is said to be RDG limit. In the 3D RDG limit, we consider the particle to be discretized into smaller scattering elements with volume dV. The scattering elements can be considered weakly scattering so in a first approximation they are considered to scatter independently. With ρ < 1, the field at each element can be taken as the incident field, as the phase shift is therefore small within the particle.

	By Shape:	**By Size:**		**By Composition:**
	Mie Scattering	Rayleigh Scattering	Geometric Optics	RDG
Criteria	Spheres of any size or refractive index	Particles of any shape and refractive index as long as kR<<1	Particles of any shape and refractive index as long as kR>>1	Optically soft particles of any shape or size

Table 1.1. A summary of the different approximations for special cases and their criteria.

1.6 Introduction to Q-space Analysis

Q-Space analysis is an analysis of diffraction. When the internal coupling parameter ρ', defined below, is less than 1, the scattering is in the 3D diffraction limit. When ρ'>30, the scattering reaches the 2D diffraction limit. It can be defined as the square root of the ratio of the scattering in the forward direction for the two limits.

$$\rho' = 2kR\sqrt{F(m)} = 2kR\left|\frac{m^2-1}{m^2+2}\right| \qquad (1.102)$$

where *k* is the wave number, *R* is the radius of gyration, and *m* is the complex refractive index,

$$m = n + i\kappa, \qquad (1.103)$$

where *n* is the real part of the refractive index and κ is the absorption coefficient. The function *F(m)* is the square of the Lorentz-Lorenz function of the complex refractive index and is equal to:

$$F(m) = \left|\frac{m^2-1}{m^2+2}\right|^2 \qquad (1.105)$$

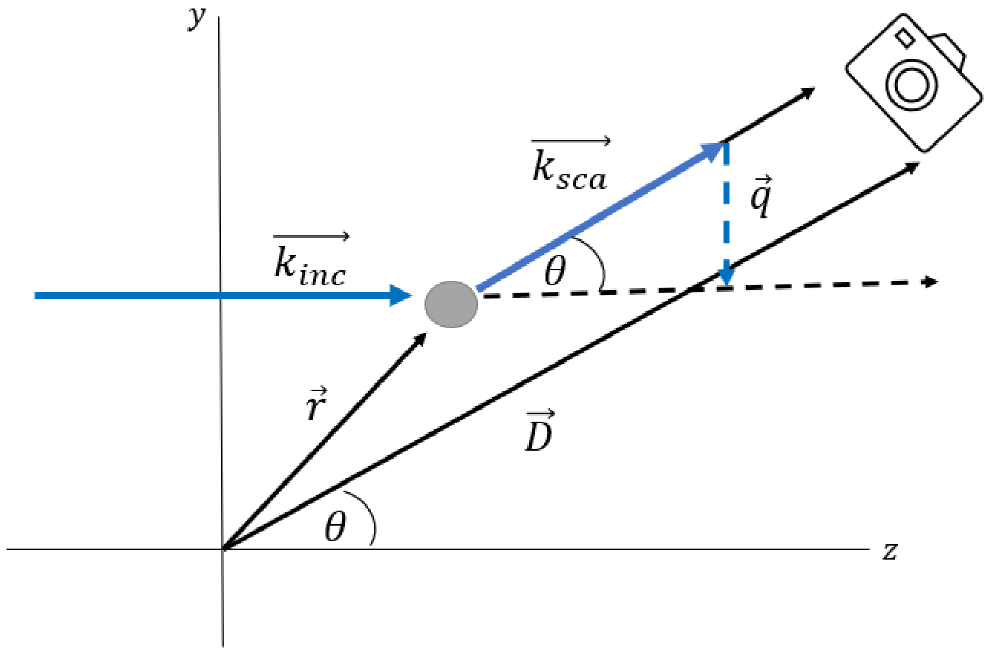

Figure 1.4. Geometry of scattering of a volume element with the definition of q explained. The incident beam defines the positive z-direction. [3], [5]**.**

Whereas most light scattering analysis plots scattered intensity I vs scattering angle Θ, Q-space analysis plots intensity against the scattering wave vector magnitude, defined as:

$$q = 2k \sin\left(\frac{\theta}{2}\right), \qquad (1.106)$$

where k is the wavenumber and θ is the scattering angle.

Plotting the scattered intensity versus q on a log-log plot reveals power-law descriptions of the scattering with length scale dependent crossovers between power-law regimes. It also describes the magnitude of the scattered intensity and the interference ripple structure that often comes with those power laws [19]. The analysis can apply to many particle shapes, ranging from spheres, cylinders, and fractal aggregates to more complex geometries. Q-space analysis uncovers hidden information and can be used to estimate particle size and sometimes shape as well. It can be helpful in remote sensing problems due to the typical lack of precision in the measurements because Q-space deals with behavior and trends and not individual data points. This work applies Q-space to the cryovolcano observations of Enceladus. Using Q-space to figure out the size of particles is called the “scaling approach”, as mentioned in [19], [20].

1.7 Summary of Light Scattering Behavior

It is difficult to determine exactly what kind of particle is scattering light just from looking at a plot of its intensity or polarization. However, certain behaviors arise in certain specific situations and some basic rules include:

1. The scattering amplitude in the forward direction is proportional to the cross-sectional area of the particle regardless of shape and refractive index due to scalar diffraction theory in the small wavelength limit [3].
2. The larger the particle, the more light is peaked in the forward direction which makes it harder to differentiate between incident and scattered light [3].
3. Larger particles (relative to λ) create more ripples in the scattering curve.
4. Orientation averaging a particle or averaging over a particle size distribution removes ripples due to interference.

This is all important for preliminary analysis because inverse problems have so many unknowns. It is important to narrow down the amount of possible particle morphologies before starting simulations in order to save on time and computational resources.

1.8 Light Scattering Codes

This work is a computational project consisting of detailed light-scattering simulations of the proxy plume-particles. Several light scattering codes exist, but this work uses T-Matrix and ADDA as they are open source and very well documented and accepted. Both T-Matrix and ADDA are powerful light scattering models each with their own merits and drawbacks which will be discussed in depth in this chapter.

The Amsterdam Discrete Dipole Approximation (ADDA) code is an open source light scattering code created by Maxim Yurkin and Alfons Hoekstra at the University of Amsterdam in 2006. Instead of calculating the fields' interactions with matter explicitly, ADDA approximates particles as multiple point dipoles using the discrete dipole approximation (DDA). It is a general method to calculate scattering and absorption of electromagnetic waves by particles of arbitrary geometry. The volume of the scatterer is divided into small cubical sub-volumes, or dipoles. Dipole interactions are approximated based on the integral equation for the electric field [21]:

$$\mathbf{E}(r) = \mathbf{E}_{\text{inc}}(r) + \int_{V|V_0}^{\cdot} d^3r^3\overline{\mathbf{G}}(r,r') \cdot \boldsymbol{\chi}(r') \cdot \mathbf{E}(r') + M(V_0,r) - \overline{L}(\partial V_0,r)\boldsymbol{\chi}(r') \cdot \mathbf{E}(r') \tag{1.107}$$

where $\mathbf{E}_{\text{inc}}(r)$ and $\mathbf{E}(r)$ are the incident and total electric fields at location r, $\boldsymbol{\chi}(r) = \frac{\boldsymbol{\varepsilon}(r)-\mathbf{1}}{4\pi}$ is the susceptibility of the medium at point r, with ε(r) as the permittivity of free space. V is the volume of the particle, and V_0 is a smaller volume inside *V*. $\overline{\mathbf{G}}\,(r,r')$ is the free space dyadic Green's function, *M* is an integral associated with the finiteness of V_0, and $\overline{L}$ is the "self term dyadic".

Equation (1.107) is the basis for how ADDA works, and [21], [22] explain more in depth about solving the singularities that arise. It is important to note that ADDA solves for the coupling of the internal fields exactly. It is only an approximation due to the discretization of the scatterer into point dipoles. A high number of dipoles increase the exactness of the result, and the simulations in this paper use a resolution of 15 dipoles/wavelength, which is agreed to be high enough resolution by the developers of ADDA [23].

The T-Matrix method is a technique for computing the electromagnetic scattering of single, homogenous particles of arbitrary shape using the Huygens principle proposed by Peter Waterman [24]. It expands the incident and scattered waves in terms of vector spherical wave functions and relates them using a transition, or T, matrix. It reduces exactly to the Lorenz-Mie theory when the scatterer is a homogenous sphere made of isotropic materials [11].

Like Mie theory, the T-matrix method is a solution to Maxwell's equations for scatterers of a size of the order of the illuminating wavelength. However, unlike Mie theory it can compute scattering from a variety of geometries including spheroids, Chebyshev particles, cylinders, etc. The method uses an infinite expansion of vector spherical wave functions that are evaluated numerically and then truncated when converged to a sufficient accuracy. The resulting matrix is a complete numerical solution to Maxwell's equations over the entire scatterer geometry and provides the scattered field over the entire solid angle (4π) for both polarizations. In principle, the method is applicable to any particle geometry, but in practice at least one axis of symmetry is usually required for efficient computation. Furthermore, particles much larger than the wavelength, or that are highly non-spherical, may accumulate excessive rounding error that prevents convergence. An overview of the T-matrix computation is provided by [11].

As previously mentioned, both ADDA and T-Matrix are widely used light-scattering codes, each with their own advantages and drawbacks; one method may be more suitable for certain particle geometries than the other. Both methods accommodate particles in fixed random orientations and T-Matrix analytically averages over orientations as well. T-Matrix performs well for nearly spherical particles, such as spheres, spheroids, cylinders, and Chebyshev particles with size parameters *kR*<20. T-Matrix is extremely fast for small particles and slower with increasing size parameters and can average over size distributions easily. ADDA is well suited for arbitrary shaped particles as described by a shape file, including basic shapes like spheres and spheroids. However, ADDA is comparatively slower, especially for particle size-distributions as each size in the distribution must be calculated separately and then averaged. Here, ADDA is used to simulate the hexagonal prisms.

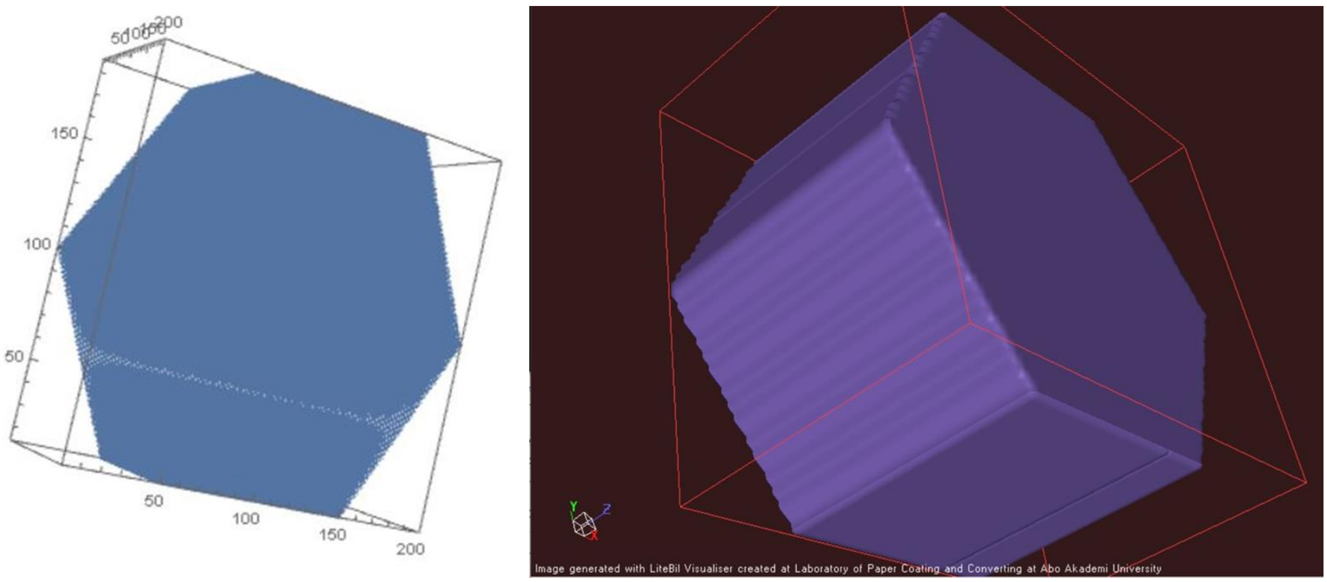

Figure 1.5. A hexagonal prism of aspect ratio of distance to length D/L=1 as a lattice of points in Wolfram Mathematica and visualized in ADDA's sister software, LiteBil [25], [26]. The prism has been rotated between the two images to show that the width and length are equal.

Both codes compute the Mueller scattering matrix, which is used here to calculate the equivalent width and DoLP. Because of these computational characteristics, T-Matrix is used for most of the simulations in this paper, and ADDA is used only for the hexagonal prisms, which cannot be considered with T-Matrix.

With any code, it is important to ensure that the results are legitimate. T-matrix and ADDA are both well-established codes, and rigorous testing shows that ADDA and T-Matrix agree on the geometries they both can compute, with an example shown in Fig. 1.6, below.

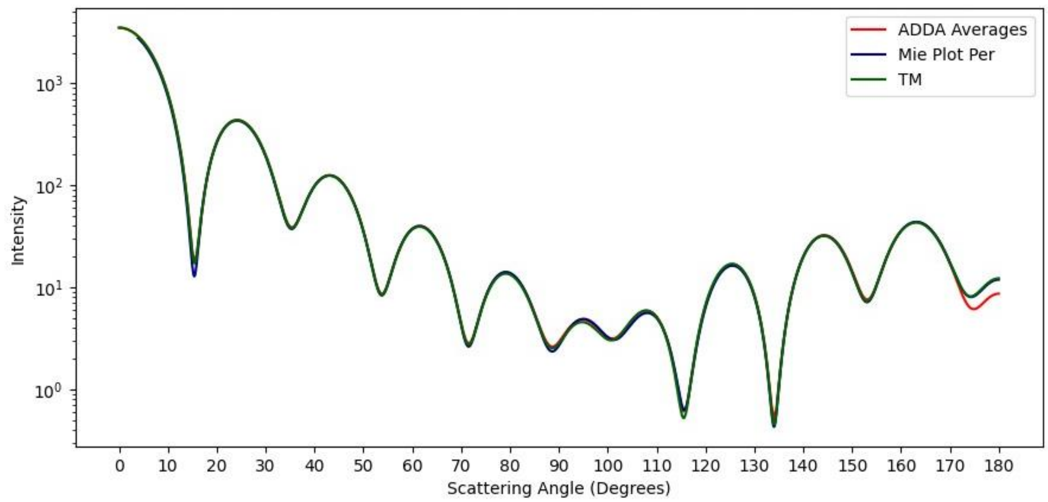

Figure 1.6. An example of T-Matrix, ADDA, and MiePlot, a simple Mie scattering code [27], agreeing for a log normal distribution of spheres.

Simulations are needed to analyze Enceladus' polarization data and form conclusions. The low DoLP implies that there is multiple scattering occurring. However, ADDA and T-Matrix are both single-scattering codes. Due to computational limitations, this model uses these single scattering codes to compute a normalized DoLP, in order to approximate multiple scattering. This approach is based on that of [28], as polarization from multiple-scattering is approximately an order of magnitude lower than polarization from single scattering. This process is spoken about in depth in Chapter 6.

1.9 Particle Size Distributions

Aerosols in nature tend to follow lognormal size distributions [11], meaning that the size ranges contain more small particles than larger particles. A lognormal distribution is simply the natural logarithm of a normal (Gaussian) distribution, so it is still described by mean, μ, and standard deviation, σ [29]. All size distributions simulated in this work are lognormal.

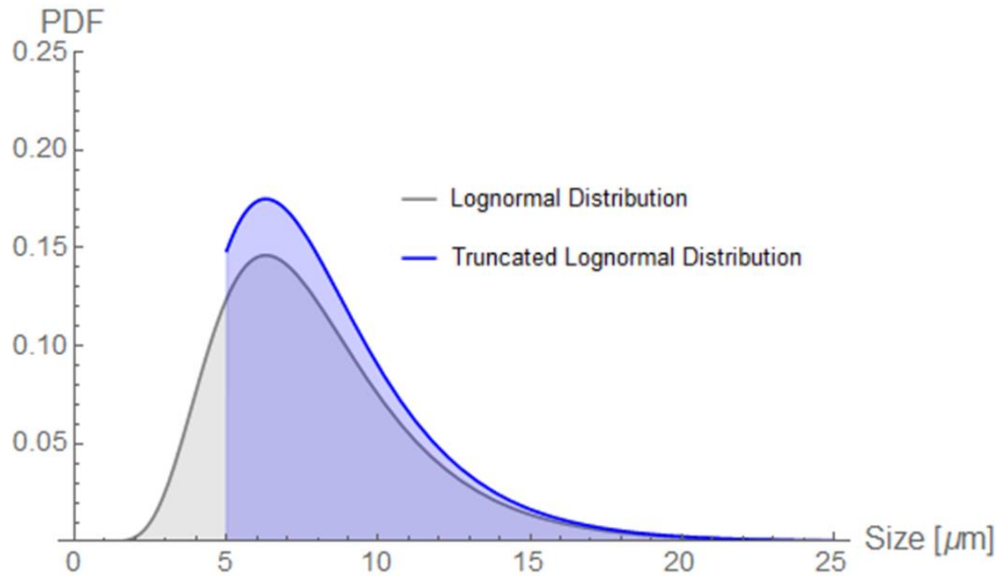

Figure 1.7. The Probability Density Functions (PDF) of example lognormal and truncated lognormal distributions as created with Wolfram Mathematica [25]. The truncated distribution pictured here only has a lower limit, although it is possible to truncate with an upper limit as well.

Fig. 1.7 shows example lognormal distributions with size on the *x*-axis and the Probability Density Function (PDF) on the *y*-axis. The PDF is the statistical likelihood that the respective size occurs in the distribution [30]. The PDF under the curve must add to 1, which is why creating a lower limit increases the PDF at all points in the new distribution. T-matrix analytically creates lognormal distributions, but for ADDA, the particle sizes are created with Python's NumPy lognormal distribution generator [11], [31]. Chapters 6 and 7 explain the effects of truncating the simulated distributions as well as the effects of changing their input parameters with regard to matching the Cassini data.

Chapter 2 – Enceladus

Enceladus is Saturn’s sixth largest moon and was discovered by William Herschel in 1789. Not much was known about it until Voyagers I and II flew by Enceladus while studying Saturn in 1980 and 1981, respectively. The most information on Enceladus, and all of the data used in this work, come from NASA’s Cassini spacecraft which observed Enceladus from 2004-2017 [32].

2.1 Context

Enceladus is one of the most reflective bodies in the solar system, as it is covered in a thick crust of ice. Due to its proximity to Saturn and Jupiter, and the fact that it is only about 500 kilometers across, tidal forces have a large effect on it. In addition, it is in a 2:1 orbital resonance with Dione, the fourth largest moon of Saturn [33], which generates a compound tidal effect on the moon. The gravitational pull on Enceladus by these bodies causes it to contain a significant amount of internal energy. Much like how volcanoes on Earth release the energy caused by radioactive decay and thermal convection in the mantle, Enceladus’s internal energy is also released through volcanism [34]. However, as Enceladus is past the solar system’s ice line, this energy is released through cryovolcanoes, or large geysers on its surface that spray various ice and dust particles. This energy is also thought to cause Enceladus to have a large subsurface liquid ocean that feeds the geysers, although Enceladus’ surface temperature is about 70 K, meaning that its crust is fully frozen [35].

Cryovolcanoes do not only exist on Enceladus, but they have been heavily documented there by Cassini during flybys of Saturn. They are known to exist on other celestial bodies as well, such as Jupiter’s moon Europa, Neptune’s moon Triton, and on the asteroid Ceres. Not much is known about the cryovolcano vents themselves, or of the particles that are released. However, most research agrees that they contain ice and volatiles.

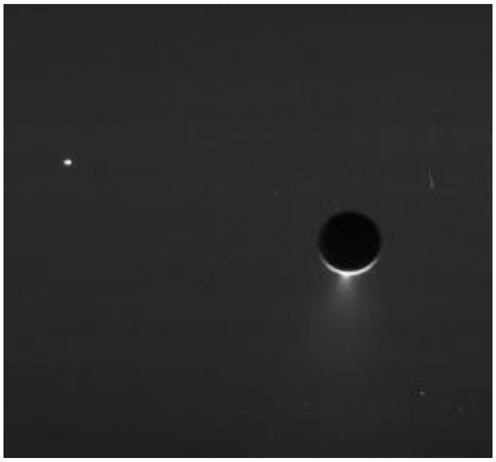

Figure 2.1. Enceladus and cryovolcanoes as viewed by Cassini. The plumes are visible on the south pole, and Dione, another moon of Saturn is visible in the background [36].

Enceladus is situated in Saturn's E-Ring. The E-ring is the most diffuse of the rings as it is comparatively dim yet covers a large volume [37]. Saturn has over one hundred confirmed moons, and these all apply forces on Enceladus at varying amounts along its orbit. Enceladus is thus geologically active, caused by a surplus of internal energy due to tidal friction [38]. Like Earth, this internal energy is released via volcanism, though unlike Earth, the cryovolcanoes on Enceladus are congregated at the moon's south pole. It is believed that Enceladus "paves" the E-ring as it orbits [36].

In 2004, the Cassini spacecraft first observed these cryovolcanoes, or geysers, whereafter, further flybys were conducted. In the literature, the words geysers and cryovolcanoes are used interchangeably, as there is no conclusive evidence thus far on the nature of the eruption mechanism, which is what differentiates the terms. It is known, however, that they are not like terrestrial volcanoes, emitting a mixture of ice, dust, and gas as opposed to lava and ash [39]. They are also congregated along Enceladus' South Polar Terrain (SPT) in fissures called "tiger stripes" [36].

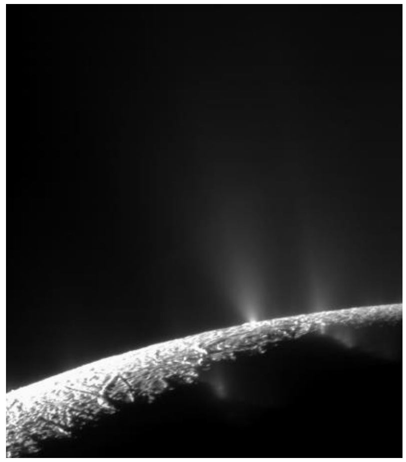

Figure 2.2. The surface of Enceladus as photographed by Cassini. This was one of the first records of geologic activity coming from the SPT. Multiple tiger stripes are easily visible, and the plumes eject a mist [36].

Moreover, Cassini's magnetometer shows evidence that Enceladus has a subsurface ocean. As Enceladus is situated past the solar system's ice line, which lies between Mars and Jupiter, its surface is entirely frozen. This means that Enceladus is a rocky body with a global ocean, all enveloped by an icy crust. Given that the origin of life on Earth is thought to be the geothermal vents, Enceladus is thus of interest as a possible host for life due to the similar geology [40].

It is known that smaller plume-particles escape to Saturn's E-ring and larger particles fall back to Enceladus' surface [39], [41]. Water ice [42], [43], silica [44], and ammonia hydrate [45], [46] have been detected, but many unanswered questions about the particles remain. The size distributions and possible particle geometries found by different studies vary, and no clear consensus exists. An improved understanding of the cryovolcano plumes may provide further insight for the subsurface dynamics.

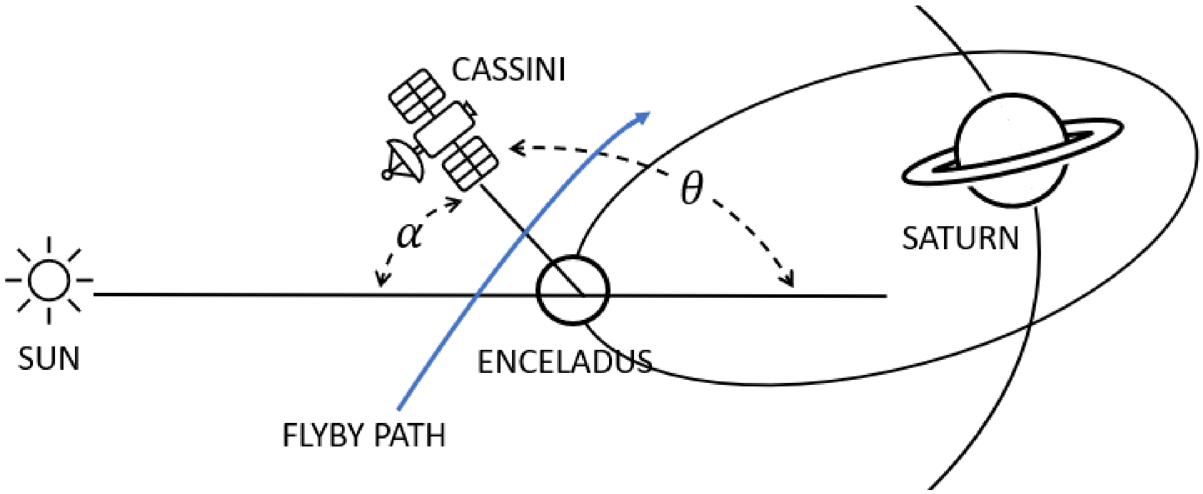

Figure 2.3: Geometry of the Sun-Enceladus-Cassini-Saturn system. Saturn orbits the sun, Enceladus orbits Saturn, and during a flyby, Cassini orbits Enceladus. In the diagram, Enceladus resides at the apocenter of its orbit around Saturn. It is important to note that Enceladus is situated in the rings of Saturn, and is not as distant as the diagram depicts. The phase angle α is the Sun-Enceladus-detector angle, and the scattering angle Θ is the angle through which sunlight is scattered. Thus, we see that $\Theta=180° - \alpha$. The cryovolcano plumes on Enceladus are only visible at scattering angles of $\Theta<40°$, but images are recorded at a much larger range of angles.

2.2 Equivalent Width

Equivalent Width (EW) is a quantity that is confusing to beginners and experts alike. It is primarily only used in planetary rings studies and is often used because it accounts for the background subtraction of other illuminated objects, as well as issues such as a celestial object being smaller than the resolution of the detector.

Imagine a cloud of scatterers in space illuminated by sunlight as viewed by a detector. The power emitted from the cloud in a narrow solid angle as subtended by the detector must equal the power received by the detector. Using this definition, we can mathematically write the equivalence of the power as:

$$\frac{IA_{\mathrm{d}}dA}{D^2} = \frac{\pi FNA_{\mathrm{p}}Q_{\mathrm{sca}}A_{\mathrm{d}}P(\theta)}{4\pi D^2}$$

(2.1)

with the left side of the equation corresponding to the detector and the right side corresponding to the cloud. The received intensity in the detector is denoted by *I*, A_d is the detector area, *dA* is the area the detector subtends, and *D* is the distance from the cloud to the detector. That makes the left side the intensity of the detector times its solid angle.

The right side of Eq. (2.1) is more complicated; *F* is defined to be the flux emitted by the particles, with a factor of π to make it directional, *N* is the number of scattering particles in the cloud, each with particle area A_p, *P(θ)* is the scattering phase function, and Q_{sca} is the scattering efficiency. The right side is also multiplied by the subtended solid angle to become a power quantity. Ingersoll and Ewald define the EW as [41]:

$$\mathrm{EW}(\Theta, \mathrm{N}) = \int \frac{\mathrm{I}}{\mathrm{F}} \mathrm{dx} = \frac{\mathrm{N A_p Q_{sca} P(\theta)}}{4} \quad (2.2)$$

The EW can be treated as an intensity, even though it has units of distance. It is an integral of the reflectance of the scatterers, see [47] for a more in-depth explanation and derivation beyond what is covered in this section.

The plume data in this dissertation is from [41], [48], where the authors measure the *I/F* values in a line of pixels perpendicular to Enceladus' rotation axis and then multiply by the projected pixel size, perpendicular to the line of sight at the distance to Enceladus center, in km. Therefore, *x* is the distance along the line of pixels, so EW is given in units of km. As the plumes are optically thin, the EW accounts for all the light from the particles in a horizontal plane one projected pixel thick at the altitude of the line of pixels in the image.

This project is an inverse problem, so the measured intensities of the plumes are compared to intensities of light scattering simulations. That means that EW must be in a form that can be calculated from the outputs of ADDA and T-Matrix. Using the formulas for the scattering quantities such as the scattering efficiency $Q_{\text{sca}}$and phase function $P(\theta)$ allow us to reduce the EW in Eq. (2.2) further [3].

$$Q_{\text{sca}} = \frac{C_{\text{sca}}}{A_{\text{p}}}$$

(2.3)

$$\text{and}\;\; P(\theta) = \frac{4\pi S_{11}(\theta)}{C_{\text{sca}}k^2}$$

(2.4)

Combining Eqs. (2.2)-(2.4) and simplifying gives:

$$\text{EW}(\theta, N) = \int \frac{I}{F}dx = \frac{NA_{\text{p}}\frac{C_{\text{sca}}}{A_{\text{p}}}4\pi S_{11}(\theta)}{4C_{\text{sca}}k^2}$$

(2.5)

or

$$\text{EW}(\theta, N) = \int \frac{I}{F}dx = \frac{N\pi S_{11(\theta)}}{k^2}$$

(2.6)

Eq. (2.6) is now in terms of the S_{11} element of the Mueller scattering matrix, which is calculated by the light scattering simulation codes, ADDA and T-Matrix, as described in Chapter 1 [22], [49]. This is necessary for comparing the satellite data to light scattering simulations and removes the particle area term, which is an unknown quantity. The wavenumber *k* is known because the central wavelength λ of each Cassini filter is known. The number of particles, *N*, creates a problem, however, as the particles present in an image are not countable, a complication addressed in the next sections.

2.3 Internal Energy and Tidal Forces

There are many mechanisms to create internal energy, including cooling, tidal forces, and resonances. Earth experiences tidal forces, especially from the moon and sun, but as mentioned earlier, most of Earth's internal energy, and thus volcanism, is left over from its formation. Because of Earth's size and composition, its crust cooled much more quickly than its core can. For a smaller body that can fully cool quickly, such as the moon, this would not be a problem, but Earth is still cooling to this day. As the crust cools, it hardens, so the heat inside the planet builds up, and escapes through fissures it creates in the crust [50]. On Enceladus, the internal energy is from a different source. The constant variable stress on Enceladus due to the other moons in Saturn's system as well as Saturn itself heat up Enceladus's rocky body [38].

In the literature, the words geysers and cryovolcanoes are used interchangeably in the context of Enceladus, as there is no conclusive evidence thus far on the nature of the eruption mechanism, which is what differentiates the terms. Geysers erupt due to the conversion of thermal to kinetic energy during decompression. On Earth, what happens is that water deep underground is heated up by the surrounding hot rock, and under certain conditions, the pressure is the rock is released causing the water to erupt as either water or steam depending on the temperature and how the gas behaves. Geysers are very closely related to hot springs, and often are found near each other [51]. Terrestrial volcanoes erupt due to the mantle of the earth being so hot that it melts the rock into magma. Since the magma is less dense than the surrounding rock, it pushes through cracks and fissures to the surface as lava. The amount of gas released and the explosivity of a volcanic eruption depends on the consistency of the magma and varies from volcano to volcano [52]. On Enceladus, cryovolcanoes would involve melting the surrounding ice which then gets ejected whereas geysers heat up water surrounded by rock. Since there is no conclusive evidence on the vents or the thickness of the ice shell inside of Enceladus, both processes are possible.

Tidal forces vary over Enceladus's orbit, so knowing where Enceladus is over the orbit is important. In [48], the authors discovered a decadal variability in the number of particles being ejected from the cryovolcanoes. As shown in Eq. (2.6), the intensity of the particles in the photographs is dependent on both the viewing geometry and the number of particles in the photo, θ and N, respectively. That means they are coupled, so one must understand the mean anomaly and the orbital dynamics of the system before understanding the data.

Johannes Kepler, with data from Tycho Brahe and the ideas of Copernicus, derived three laws of planetary motion [53]:

1. A planet orbits in an ellipse with its sun at one focus.
2. A line segment joining a planet and its sun sweeps out the same area of the ellipse in equal intervals of time.
3. The square of a planet's orbital period is proportional to the cube of its orbital semi-major axis length.

These laws can be extrapolated to any orbiting and host bodies, such as Enceladus around Saturn. With these laws, an object's position along its orbit can be fully described by the Keplerian elements: eccentricity, semi-major axis length, inclination, ascending node location, longitude of the ascending node, argument of periapsis, and true anomaly, which describe everything about the orientation of the elliptical orbit in space [53].

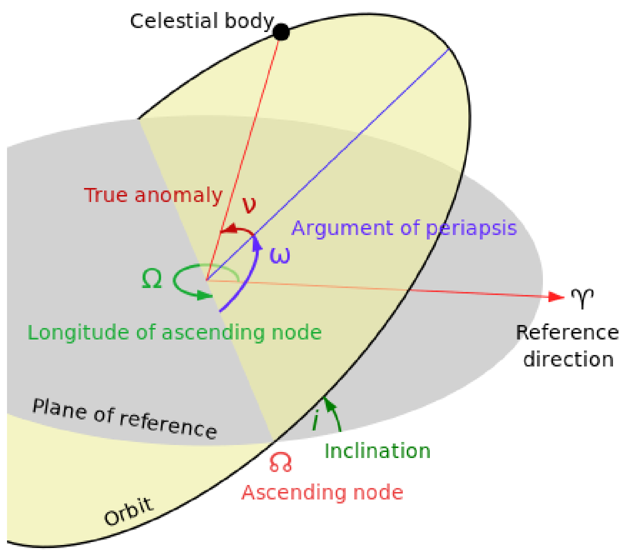

Figure 2.4: The Keplerian elements of a planet's elliptical orbit, taken from [54].

However, as Enceladus and Saturn are roughly in the same reference plane, as well as in the reference plane of the solar system, the main Keplerian elements that describe Enceladus' location around Saturn are its eccentricity and true anomaly. It is often easier to work in mean anomaly M as opposed to true anomaly υ because an object's speed varies along an elliptical orbit [fastest nearest to the host (pericenter) and slowest farthest from the host (apocenter)].

One can describe an object's position in an orbit by mapping its elliptical orbit onto a circular orbit via averaging the elliptical orbit speeds to one constant speed. Mean anomaly therefore is the angular distance from pericenter where a fictitious body would have moved in a circular orbit, with constant speed, in the same orbital period as the actual body in its elliptical orbit. As an angular distance, mean anomaly is expressed between 0-360 degrees as measured from the closest point to the host body. Mean anomaly at an arbitrary time t is defined as:

$$M = \frac{360}{T}(t - \tau) \qquad (2.7)$$

where T is the period of the orbit and τ is the time at which the orbiting body is at pericenter. If the eccentricity is low, such as for Enceladus' orbit around Saturn, then the mean anomaly is very close to the true anomaly. However, there is sufficient eccentricity for Enceladus' distance from Saturn to vary and cause variable tidal stresses on the moon.

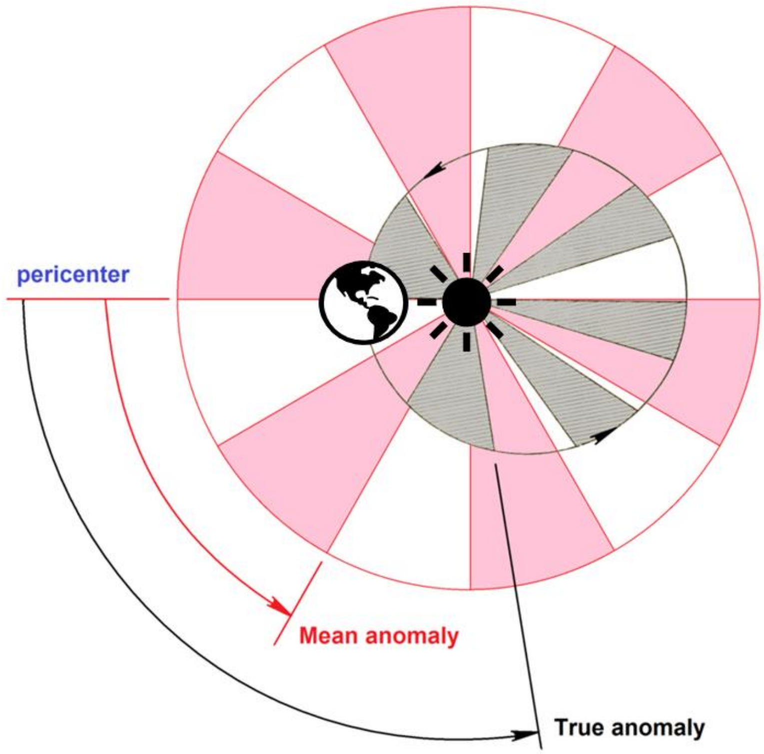

Figure 2.5: A pictorial representation of mean anomaly, *M*, demonstrated by the Earth in its orbit around the sun. Each shaded region represents one month of the year as each one represents 1/12 of the total orbit. Notice how the true anomaly is larger than the mean anomaly in this case. That will switch when the Earth is closer to apocenter[48]. This image is taken from [50] and modified for simplicity.

Because Saturn has over 100 moons, there are many sources of tidal forces. As Cassini flies by Enceladus multiple times, the satellite records data at multiple orbit locations and records the mean anomaly *M*. All intensity data of Enceladus' plumes for the duration of Cassini's mission as analyzed by [48] is shown in Fig. 2.6.

Plotting EW versus *M*, Fig. 2.6 below, shows the systematic behavior of the plumes as Enceladus orbits. Enceladus orbits Saturn in ~33 hours, and Saturn orbits the sun in around 29 years. Previous papers such as [41], [56], [57] have found that the amount of particles released from the cryovolcano vents varies over time. Reference [41] found that there is a decadal variability in the amount of particles released. This work assumes that the number of particles released depends on the orbital position due to the tidal forces causing the vents to eject more in some places over others. This needs to be accounted for and is done by fitting and dividing out the mean anomaly curve. This is explained more in Chapter 5.

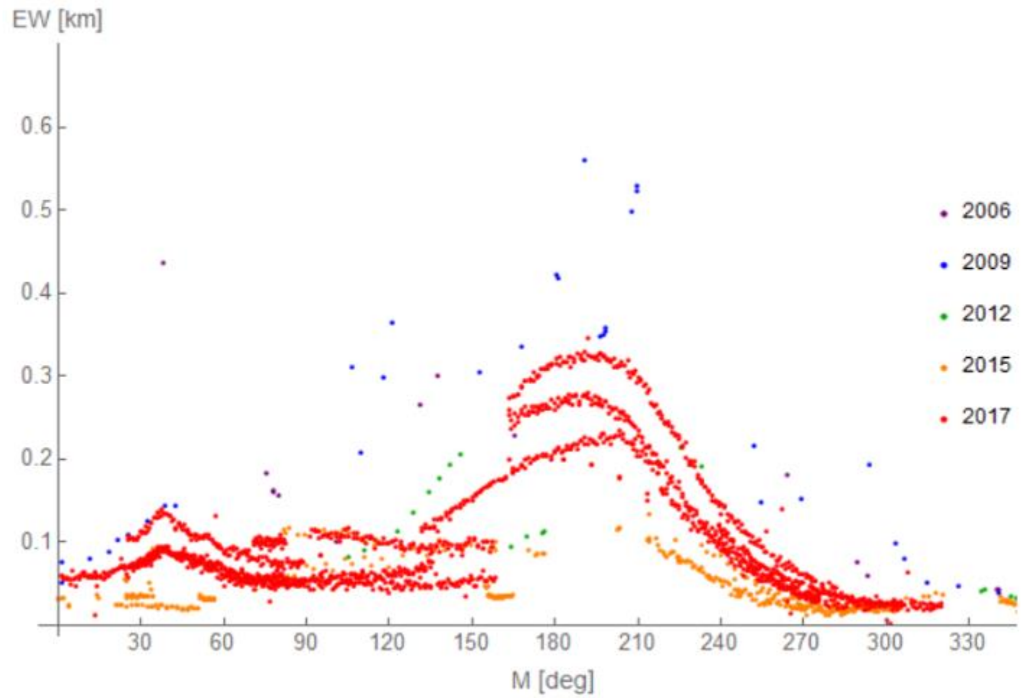

Figure 2.6. The Equivalent Width *EW* as a function of mean anomaly *M* as collected and analyzed by [48]. Each color represents a different year's dataset. If *EW* was only dependent on Θ and not *M* as well, the above plot would look random. Also, if the increase in cryovolcano activity as demonstrated by *EW* was only due to Saturn, there would be a maximum at M=0°. Instead, the dual-peaked nature is most likely due to tidal resonances from Dione and other moons.

If the tidal forces only come from Saturn, one would expect the greatest *EW* at pericenter, as that is when Enceladus is closest to Saturn. However, models such as [58] show that the stress on the faults of Enceladus' South Pole may peak near apoapsis. The fact that the *EW* peaks when Enceladus is furthest from Saturn implies that there are multiple effects causing the cryovolcanoes to erupt beyond simple tidal heating from Saturn.

The variation in *EW* between years likely comes from several sources, including Enceladus' 2:1 resonance with Dione [59], [60]. Other possible sources may include Saturn's orbit around the sun or internal factors such as the structure of the vents [48]. The vents may open and close due to tidal stresses or even clog at certain points along the orbit. There is currently no full explanation for the smaller first peak, either.

Orbital resonances compound tidal forces, and often are sources of large amounts of internal energy, especially in the case of Enceladus where there are so many bodies in Saturn's ring system [38]. However, because Saturn's rings contain many bodies, it is difficult to calculate all the tidal forces acting on Enceladus at different times. One Saturn year takes 29.5 Earth years, and the planet precedes as it orbits [61]. As Enceladus is in the plane of Saturn's rings, Saturn's precession causes Enceladus to enter and exit the orbital plane of the solar system. Although, the effects of Saturn's orbital eccentricity and obliquity are much smaller than the effects of the other moons such as Dione [57].

2.4 Cassini

NASA launched its Cassini Spacecraft in 1997, with only four flybys of Enceladus originally planned. However, cryovolcanoes were discovered in 2004, and 32 total flybys were scheduled. Cassini had many instruments on it but here only the Imaging Science Subsystem (ISS) is considered. Other instruments, such as the Ultraviolet Imaging Spectrograph (UVIS) and the Visual and Infrared Mass Spectrometer (VIMS), are used in the studies listed in Table 3.1. Fig. 2.7 shows all of the scientific instruments on Cassini [62].

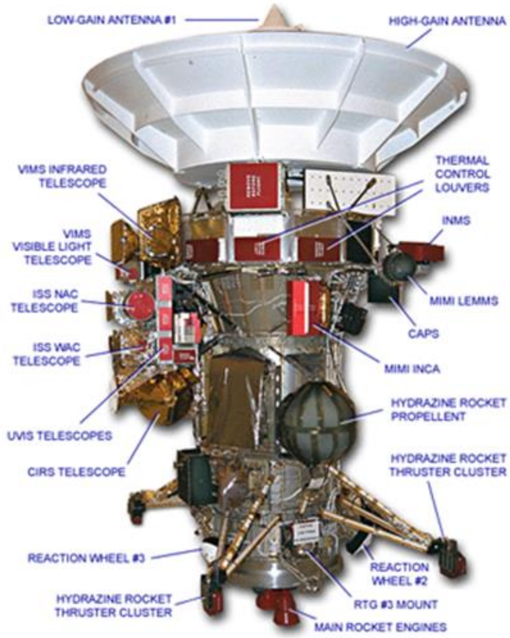

Figure 2.7. An overview of the instruments on the Cassini spacecraft. This work uses the ISS NAC telescope (left middle) as its main source of data. Data from other instruments are used in papers such as those listed in Table 3.1 This image is taken from [62].

The Cassini ISS was one of the instruments on the Cassini spacecraft. It contained the Narrow Angle Camera (NAC) and Wide Angle Camera (WAC), which both had filter wheels of various colors filters as well as polarizing filters. Both the intensity data and the polarization data in this work come from NAC images.

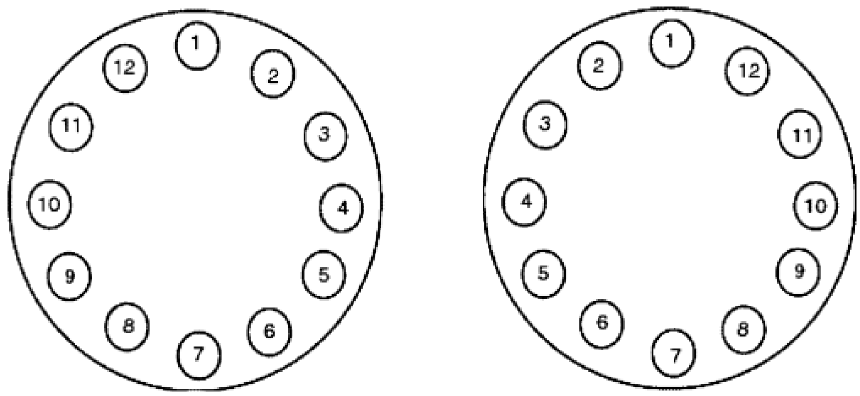

NAC Filters

(Wavelengths, in nm, are central wavelengths computed using the full system transmission function.)

Filter Wheel #1	Filter Wheel #2
1) CL1 (611W)	1) CL2 (611W)
2) Red (650W)	2) GRN (568W)
3) BL1 (451W))	3) UV3 (338W)
4) UV2 (298W)	4) BL2 (440M)
5) UV1 (258W)	5) MT2 (727N)
6) IRP0 (746W)	6) CB2 (750N)
7) P120 (617W)	7) MT3 (889N)
8) P60 (617W)	8) CB3 (938N)
9) P0 (617W)	9) MT1 (619N)
10) HAL (656N)	10) CB1 (619N)
11) IR4 (1002LP)	11) IR3 (930W)
12) IR2 (862W)	12) IR1 (752W)

Figure 2.8. An overview of the NAC filter wheels from the Cassini spacecraft showing the central wavelengths of the filters. Not every available filter was used during the Enceladus flybys. This image is taken from [62].

This work analyzes the polarization photos from the NAC. The NAC polarizer consists of polaroid material that spans the wavelength range. The NAC had 0°, 60°, and 120° polarizing filters, whereas the WAC only had two: 0° and 90° [63]. The NAC first started taking polarization images of Enceladus in late 2004 and stopped in 2017. All images are free to access on NASA's SETI OPUS webpage. There, 1398 NAC polarization images of Enceladus were listed in sets of three angles. These NAC images were also in three different filters, GRN, UV3, and MT2. The wavelengths for the three filters are 569 nm, 343 nm, and 727 nm respectively. Because the images must be used in sets of three, there are 466 total sets divided between the three filters, with the most being in GRN and the least amount taken in the MT2 filter. Before this work, the Cassini polarization images had never been processed.

There are many coordinate systems used in this work, including the scattering plane, as explained in Chapter 1. A representation of the spacecraft frame (sp), camera frame (cam), and image frame (im) is shown in Fig. 2.9. The diagram is based off that found in [62]. By using the location of the sun either in the image (sun-image-azimuth angle) or Cassini's measured phase angle, it is possible to transform to the scattering plane.

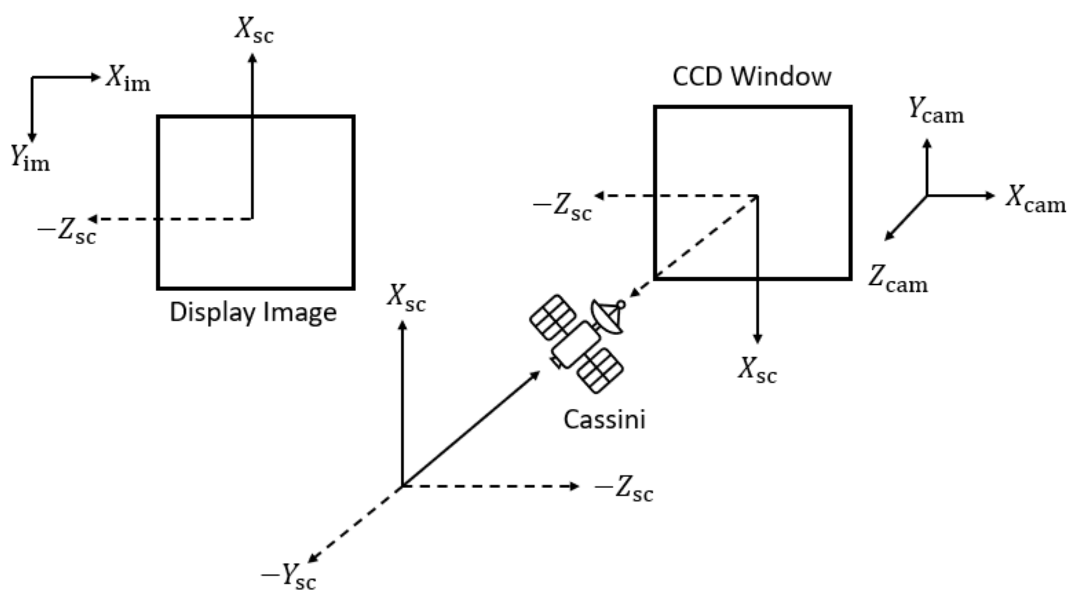

Figure 2.9. The three coordinate systems for Cassini's Imaging Science Subsystem cameras: the spacecraft coordinate system (sc), the camera coordinate system (cam), and the image coordinate system (im). Here, the ISS camera is oriented along the -*Y*-axis of the spacecraft. The optics of the cameras rotate the image. This image is based on a diagram from [62].

Chapter 3- Summary of Current Knowledge

3.1 Research Purpose

The main reason why Enceladus is of high interest in planetary science is due to its subsurface liquid ocean. Many scientists believe life on earth started at the hydrothermal vents, i.e. the volcano vents on the ocean floor [64]. As there is liquid water on Enceladus due to heat from the cryovolcano vents, there is a non-zero possibility of life there. Unfortunately, there have been no probes or manned missions sent to the surface of Enceladus and there will not be any until the planned Orbilander in 2038 [65] so the only way to know what is going on under the surface is to study the particles in the cryovolcano plumes.

Earth's hydrothermal vents were originally discovered at the Galapagos Rift in 1977 and have been discovered in many other locations since then [66]. Many hydrothermal vents are in the deep ocean, and thus were one of the few places on the early Earth protected from solar radiation and meteor bombardments. Some vents can also be found much shallower at mid-ocean ridges at divergent plate boundaries. Also, complex organic molecules and the most primitive organic organisms on Earth, Archaea, have been found there. Over 300 species of organisms, many of which do not exist elsewhere on Earth, have been documented at the vents [67]. Many scientists believe a similar environment can exist on Enceladus [44].

The Cassini ISS NAC photographed much of Enceladus from various viewing geometries meaning that there are many images over a range of scattering angles and resolutions. In addition, Cassini flew through the plumes, allowing for the cryovolcanoes to be imaged closeup and not just as part of the entire surface of the moon. The intensities used in this project come from these photographs. Polarization data comes from NAC polarizer images of the surface of Enceladus, while cryovolcano intensities come from photographs of the plumes themselves. No polarization data was taken of the plumes, but that is recommended for the next mission. Chapters 4-6 talk about the analysis of these photographs in depth.

Unfortunately, like with many remote sensing problems, there is a limited amount of data on Enceladus until future missions launch. Ground-based telescopes are limited to a narrow range of angles due to the geometry of the solar system which is also why there is so little data. This work uses the limited data sets in a new way and expands on the light scattering studies that have been done before by other researchers as listed in Table 3.1.

3.2 Literature Review

It is known that the cryovolcanoes are not like terrestrial volcanoes, and they emit a mixture of ice, dust, and gas as opposed to lava and ash [39]. Existing studies attempt to estimate the size and shape of the plume particles, using methods like mass spectroscopy and plume particle trajectory calculations [36], [45], [46], [68]. Most studies that involve light scattering analysis model the plume particles as spheres, or sphere-like shapes such as ellipsoids or aggregated spheres [40], [69], [70], [71]. Yet, the frozen character of the particles suggests more complex particle morphology.

Particle sizes have been estimated between nanometers to millimeters, but most papers agree they are likely on the order of microns. Some groups have neglected the mean anomaly dependence, meaning that only data points recorded at the same mean anomaly are used. While this avoids the problem of the mean anomaly dependence, it severely limits the amount of data that can be compared.

It is proposed that there is some amount of crystalline ice present in the plumes. Because the vent structure is unknown, all we know is that the ice must freeze somewhere between the liquid ocean layer and Enceladus's surface. At the temperatures present in the system (70 K or -

100 C), it is unlikely for the ice to clump together or form many of the more complicated ice shapes found on Earth [72]. The temperatures imply the ice is most likely hexagonal columns.

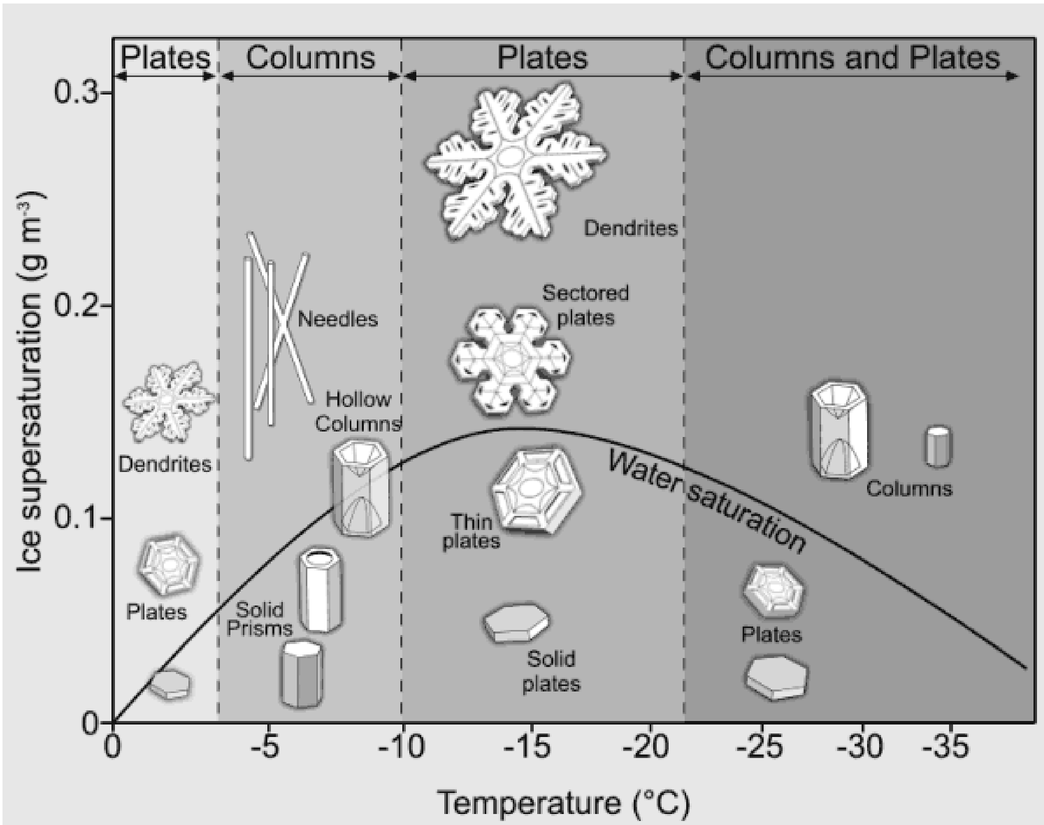

Figure 3.1. Ice shapes as a function of temperature and supersaturation, taken from [72]. Because Enceladus' surface temperature is so cold, it is far to the right of this graph. Even if the ice does not freeze close to the surface, it still will probably be a hexagonal column as opposed to a more complicated geometry.

However, if there is any flash-freezing happening in the vents, which is also possible, then the ice will not be able form lattices. This ice is amorphous and can be considered glassy. It is important to note that not all amorphous solids are glassy, e.g. silica forming as common opal versus as obsidian [73]. Amorphous ice can be modelled as a Chebyshev particle, and is not simulated in this work but may be in the future. The simulations in this dissertation only model crystalline ice.

Size Range (µm)	How they know	Assumed Composition	Year	Title
>2	Cosmic Dust Analyzer inferences (no simulations)	dust/ water ice	2006	Cassini Ion and Neutral Mass Spectrometer: Enceladus Plume Composition and Structure [43]
40-60	Spectral models of ammonia ice	ammonia hydrate	2006	Near-infrared spectra of the leading and trailing hemispheres of Enceladus. [46]
2-200 (mean 20)	Spectral models of water ice	water ice	2007	Distribution of icy particles across Enceladus' surface as derived from Cassini-VIMS measurements [42]
0.1-1	Impact ionization mass spectra of Saturn's E-ring particles	crystalline ice/ amorphous	2007	The E-ring in the vicinity of Enceladus: II. Probing the moon's interior—The composition of E-ring particles [74]
0.1-2	Scattering simulations of spheres	water ice	2009	A redetermination of the ice/vapor ratio of Enceladus' plumes: Implications for sublimation and the lack of a liquid water reservoir [75]
45-1000	UV spectral models of water ice with UVIS data	ice, ammonia hydrate	2009	The surface composition of Enceladus: clues from the Ultraviolet [45]
3.1+- 0.5 (median)	Simulations of spheres	water ice	2011	Total particulate mass in Enceladus plumes and mass of Saturn's E ring inferred from Cassini ISS images [41]
~70	Spectral water ice band analysis from VIMS	water ice	2012	Saturn's icy satellites and rings investigated by Cassini–VIMS: III – Radial compositional variability [56]
0.1-3	Scattering of spheres using VIMS data	water ice	2014	Tidally Modulated Eruptions on Enceladus: Cassini ISS Observations and Models [70]
0.006-.009	Mass spectroscopy of E ring	silica	2015	Ongoing hydrothermal activities within Enceladus [44]
0.2-20	Simulations of aggregated spheres	water ice	2015	Aggregate particles in the plumes of Enceladus [69]
0.125-2	Trajectory integration models and E-ring perturbation data	water ice	2015	Tracking the Geysers of Enceladus into Saturn's E-Ring [39]
0.01-10	Simulations of spheres	water ice	2017	Could It Be Snowing Microbes on Enceladus? Assessing Conditions in Its Plume and Implications for Future Missions [40]
submicron-micron	IR spectroscopy from VIMS	water ice	2017	Deciphering Sub-Micron Ice Particles on Enceladus' Surface [76]

0.6-15	Plume dynamics calculations and sphere simulations	water ice	2018	Surface deposition of the Enceladus plume and the zenith angle of emissions [77]
few microns	Lab polarimetry of ice (spheres, angular grains), MiePlot	water ice	2018	Polarimetry of Water Ice Particles Providing Insights on Grain Size and Degree of Sintering on Icy Planetary Surfaces [71]
>1	Surface brightness analysis (no simulations)	water ice	2020	Photometric analyses of Saturn's small moons: Aegaeon, Methone and Pallene are dark; Helene and Calypso are bright. [78]
10-100	Discrete Element Method (DEM) of powders	water ice	2022	The icy regoliths of Enceladus and Europa: experimental and numerical study [79]

Table 3.1. A review of the sizes and compositions found in the literature from 2006 to 2022. Most scattering research assumes water ice and spherical particles.

A graphical representation of the table is shown below.

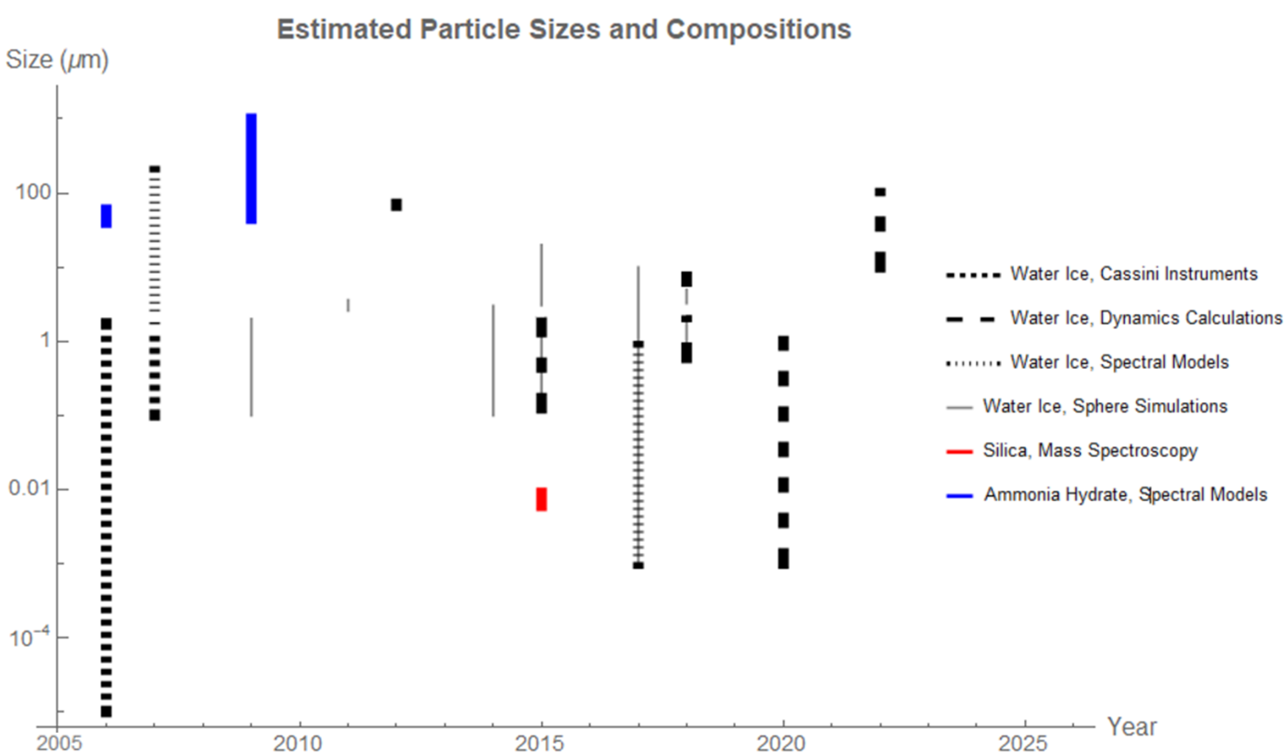

Figure 3.2. A timeline of the size ranges found in the papers listed in Table 3.1. The plot shows the years on the *x*-axis, and the size ranges in microns on the *y*-axis on a logarithmic scale.

The sizes above span a large range, and some do not overlap. This is due to many research groups using different methods, all with their own advantages and drawbacks. Previous light scattering studies on Enceladus have only used spheres and spheroids, but this work expands the simulations to other geometries like cylinders and hexagonal prisms. In addition, other scattering studies use limited intensity data as they remove the mean anomaly dependence by using points measured at the same mean anomaly but different scattering angles. This work uses all the available intensity data as well as the polarimetry data, which had never been analyzed before this project.

Chapter 4- Light Scattering Analysis

As mentioned in Chapter 1, light scattering is a useful tool for remote sensing problems, as well as for studying types of small particles like ice and dust. Because of these two reasons, it makes sense to apply it to the cryovolcanoes on Enceladus.

4.1 Initial Data Reduction

We know that the intensity of the particles' scattered light covered in Chapter 1 depends not only on scattering angle (viewing geometry) but also on the number of particles in the field of view. This is because more particles scatter more light than fewer particles do, like the Tyndall Effect of seeing your breath on a cold day [80].

Since the detector on Cassini cannot resolve each individual particle, it is impossible to know how many particles are present in the image. This means that the intensity's dependence on particle number must be neglected somehow.

Here we assume that the plume intensities vary with respect to mean anomaly M due to the changing tidal forces. The forces enhance or suppress the cryovolcano activity at certain points in the orbit, so that the intensity data is coupled with position. Ideally, EW should be a function only of Θ, but rather, it is a function of both Θ and N, see Eq. (2.6). Thus, the pixel intensities are dependent on the activity of the cryovolcanoes. The more active they are, the more particles are present in the detector's line of sight, meaning that the images contain higher intensities. In other words:

$$EW(\theta, N) = EW(N) \times EW(\theta) \qquad (4.1)$$

This must be uncoupled before any further light scattering analysis. In this work, this is done by deriving a correction factor from the 2017 data in Fig. 2.4 to apply to the data throughout the mission.

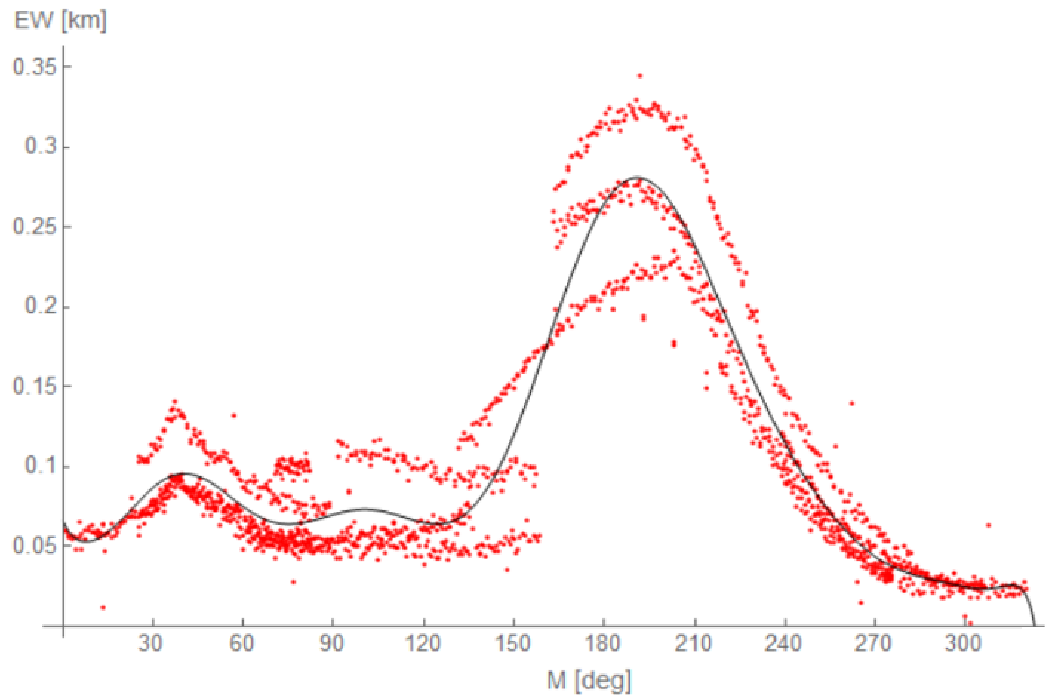

Figure 4.1. The 2017 data from Fig. 2.4 now plotted and fit with a high-order polynomial curve. The fit is calculated using Wolfram Mathematica's built-in fitting function [25]. The fitted curve represents the behavior of the cryovolcano activity with respect to orbital position, and accounts for tidal resonances and other variable forces Enceladus experiences during its orbit.

In Fig. 4.1, we fit the 2017 data from Fig. 2.4 with a polynomial of order 15. Data from 2017 is used because the 2017 curve is nestled between the other years, implying a possible near average value in the decadal variability of the tidal forces. The 2017 data also contains 1704 out of the total ~2500 data points, meaning high resolution for the fit. This specific polynomial was chosen by using Mathematica's built in fitting function, "Fit", and iterating through every order up to order 30. Order 15 was chosen by checking the residuals, and picking the lowest order polynomial that gave acceptable residuals and displayed convergence. This method is inspired by the one used in [48]. To uncouple the data, we assume the number of particles, *N*, depends on the mean anomaly *M* due to tidal forces. As *M* is a measured quantity and *N* is not, only *EW(M)* is known, not *EW(N(M))*. We assume *EW(M)* to depend linearly on *N*:

$$EW(M) = CN(M) \qquad (4.2)$$

where C is some constant.

We define a new quantity, "New Equivalent Width", or EW', to demonstrate the elimination of the mean anomaly dependence.

$$EW'(\theta) = \frac{EW(\theta,N)}{EW(M)} \quad (4.3)$$

We can combine Eqs. (4.2) - (4.3) into Eq. (4.4).

$$EW'(\theta) = C\,\frac{EW(\theta,N)}{N} \quad (4.4)$$

Plugging in Eq. (2.6) for $EW(\Theta,N)$ and simplifying results in Eq. (4.5), where EW' is now only a function of Θ and has no dependence on the orbital position of Enceladus nor the number of particles present in the plume.

$$EW'(\theta) = C\,\frac{\pi S_{11}(\theta)}{k^2} \quad (4.5)$$

Therefore, dividing every years' data in Fig. 2.4 by the equation of the fitted curve in Fig. 4.1, *EW(M),* causes the particle number dependence to no longer be an issue. If the EW was only a function of N (or M), then dividing by the curve in Fig. 4.1 would reduce everything to 1. However, this does not happen because of the dependence on scattering angle θ.

This reduction works only if the behavior of the resulting curves is considered, such as the slopes in certain regimes, not the actual values of EW' due to the constant that was introduced. Q-space analysis commonly utilizes normalized intensity values, meaning that the introduction of the constant C will not complicate this analysis.

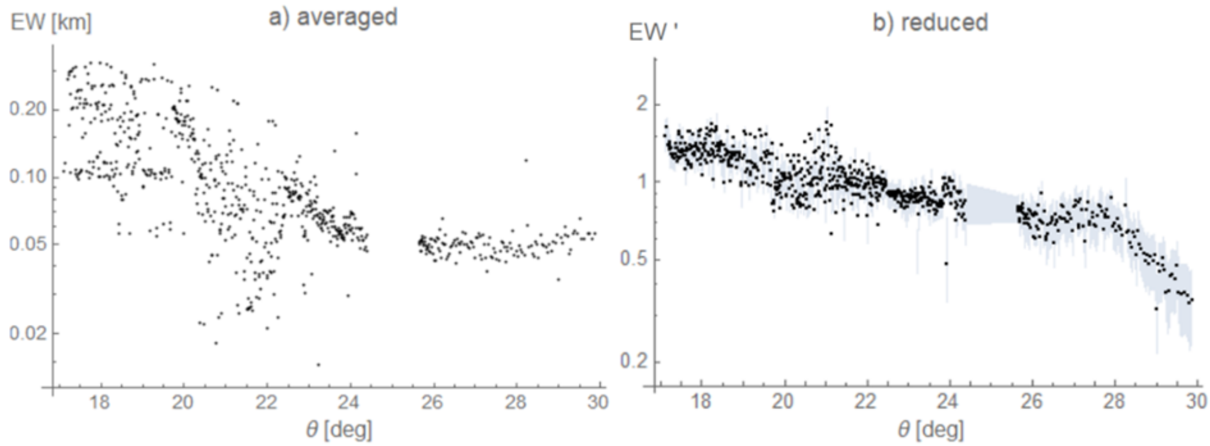

Figure 4.2. The *EW* 2017 data from Fig. 2.4, before and after the division of the curve in Fig. 4.1, now plotted logarithmically against Θ. Plot (a) has duplicate scattering angle measurements averaged to a single point. Plot (b) has error bounds added, where the error ranges from 20-40% of the *EW'* value. Plot (a) does not resemble a typical light scattering curve due to its high amount of scatter between the points. Plot (b) is much cleaner, and follows the expected shape of a light scattering curve. Unfortunately, the 2017 data does not contain measurements at very low Θ.

As mentioned in Chapter 3, diving out the mean anomaly dependence partially reduces the data. However, there are other effects going on that must be accounted for. For example, there are multiple Cassini measurements at the same angle in the same year. These must be averaged together to make one data point.

The *EW'* versus Θ plot in Fig. 4.2 (b) is much cleaner than the 2017 plot of the original averaged data, Fig. 4.2 (a). To apply the curve reduction in Fig. (4.1) to other years, the errors are binned by scattering angle. This accounts for the narrow range of angles measured in the 2017 data and allows application to years with smaller angles. The error is propagated and comes from three sources: the Cassini detector intensities themselves, the Equivalent Width measurements from [41], [48], and the fitting of the mean anomaly curves.

The first error is calculated from the standard deviation of the multiple measurements at the same angle. However, not every angle had multiple measurements and they occurred at different angles every year. In addition, the data got better and better as time went on, meaning that 2017 had the most data points. Because of this, the error in the early years' measurements was hard to calculate, but if one assumes that the detector was just as operational during the whole mission, then the 2017 data can be used to calculate the error in all years. This is done by averaging all points from the same angle in 2017 and calculating the standard deviation of those measurements. Some angles had only one measurement, most had two, and some had up to 18 measurements. Then, the errors were binned by angle, and the earlier years' errors were calculated from those bins. This is assuming that camera error is angle dependent, which makes sense as the difference in light at different angles can cause different problems in the camera. High intensity measurements cause "shot noise", whereas low intensity measurements have low signal to noise ratios (SNR).

The second type of error was listed in [48] as 10%, so that was trivial to add to the propagation. The third type comes from dividing out the fit of the mean anomaly curve, so that was simple statistics. The curve fits better at some points than others which is accounted for using the root-mean-square error (RMSE). Points outside three standard deviations of the mean are considered outliers and removed.

$$\mathrm{RMSE} = \sqrt{\frac{\sum(x_i - \widehat{x_i})^2}{N}} \quad (4.6)$$

where $\widehat{x_i}$ is the mean of the points in the angle bin, x_i is any point in the angle bin, and N is the total number of points in the bin. All three errors are propagated to calculate the errors in each data point.

4.2 Q-Space Analysis of Enceladus

Small angles offer insight into the so-called Guinier regime, which allows for simple estimation of the average particle size of by identifying the Guinier point, or where the points plateau at the smallest angle [20]. The data sets with the smallest recorded scattering angles are 2006 CLR, 2009 CLR, 2012 CLR, and 2012 BL1. The Cassini CLR filter is centered at λ=611 nm, whereas the BL1 filter is centered at λ=451 nm [62]. The four data sets with the smallest measured scattering angles are plotted in Fig. 4.3.

These plots do not show such Guinier behavior, however, implying that the particles are larger than the minimum inverse q present in the data. Here, the smallest q is $q_{\min} = 0.43\ \mu\text{m}^{-1}$, corresponding to particle sizes $>1/q_{\min} \simeq 2\ \mu\text{m}$. The particles in Enceladus' plumes are most likely present in a size distribution as opposed to being monodisperse. This simple estimation sets the minimum average size for the particles in the distribution to be greater than 2 μm.

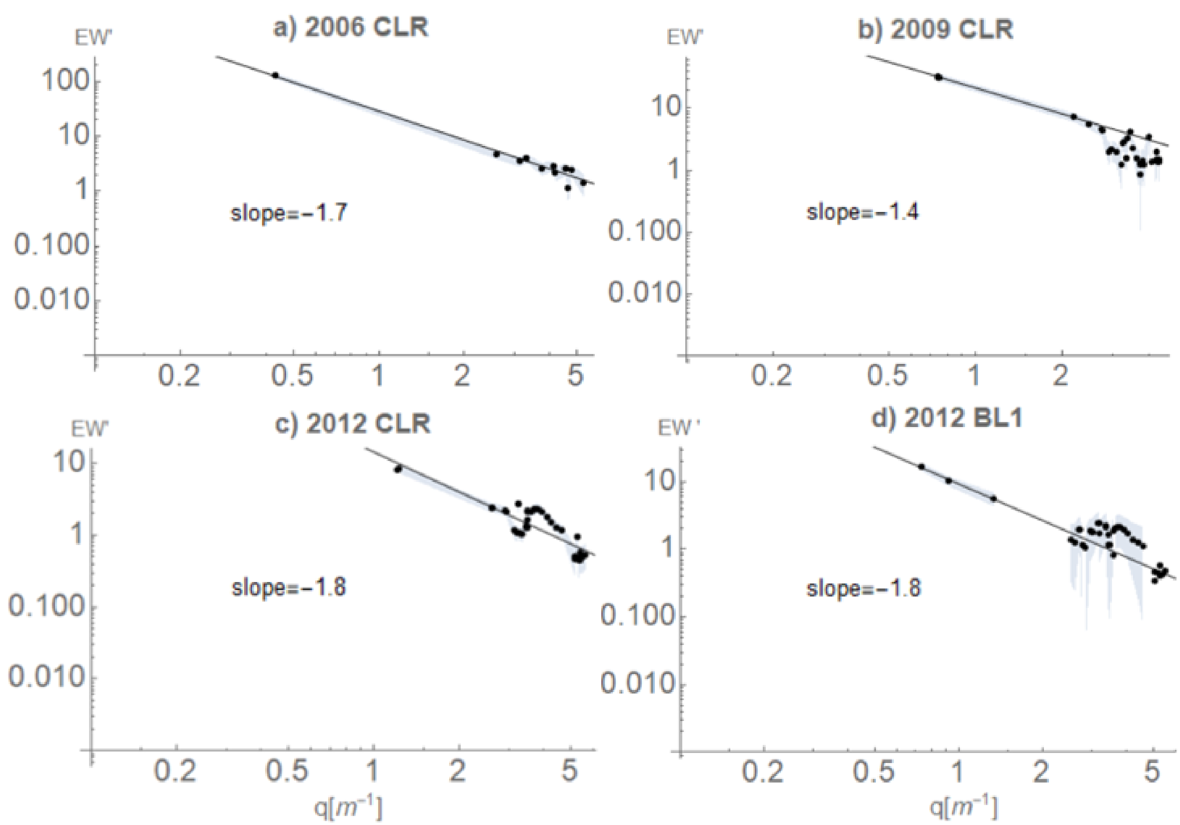

Figure 4.3. The datasets with the smallest measured scattering angles as plotted on a log-log scale in Q-space. The 2006 CLR filter has a minimum scattering angle of 2.4°, and the 2009 CLR, 2012 CLR, and 2012 BL1 data sets have minimum angles of 4.11°, 6.76°, and 4.15° respectively. The slopes of the plots (a)-(d) are -1.7, -1.4, -1.8, and -1.8. These slopes imply a possibility of the

particles being fractal aggregates or hexagonal columns, according to [81], [82], but more work is needed to justify such conclusions.

Another important quantity for Q-space analysis is the internal coupling parameter of a sphere ρ', as explained in Section 1.6 and Eq. (1.102). When ρ' <1, the electromagnetic coupling within a particle is weak. In other words, internal multiple scattering is weak, and thus the scattering is in the Rayleigh-Debye-Gans limit, which corresponds to diffraction from the volume of the particle, as explained in Chapter 1. As ρ' increases, so does the coupling and the scattering corresponds to diffraction from the particle's projected area (profile), i.e. 2D diffraction, see [20].

The ρ' parameter is helpful to compare slopes of different particles in Q-space by separating them into coupling regimes. Assuming the particles in the cryovolcanoes are ice ($m = 1.309 + 7.096 \times 10^{-9} i$ at λ=0.611 μm) [83], and constraining R>2 μm, gives ρ' > 7.92. Comparing to Fig. 1 in [81] shows that these particles potentially are not spherical, as spheres have slopes of -2 in ρ' regimes less than 10, and the slopes from the Cassini data range from -1.4 to -1.8. Even if the particles are not ice, spheres follow the same general behaviors in Q-space regardless of m. Spheres with ρ'=8 with varying refractive indices are plotted below (Fig. 4.4), with lines of slope = -2 and -3 for reference. A solid line with slope -1.7 is also plotted, as a reference to the curves in Fig. 4.3. Slopes between -1 and -2 have been found to occur for various types of irregular particles such as Saharan dust or minerals [82].

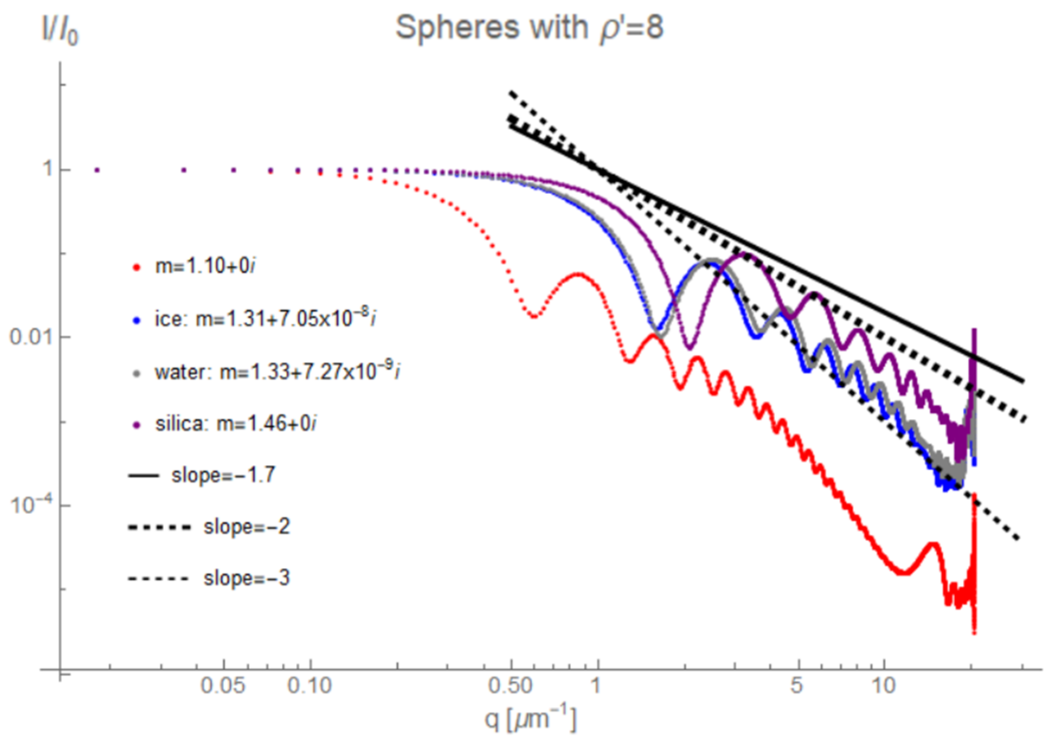

Figure 4.4. Spheres of varying refractive indices from silica to liquid water and water ice [83], plotted in Q-space with normalized intensity for ρ'=8 . These substances were chosen because they may be present in the plumes. A curve for m=1.1+0*i* is also plotted, to show that the slopes are not dependent on *m* even for low *m*. These were simulated in Philip Laven's MiePlot [27] using λ=611 nm (Cassini's CLR filter), and varying radius *R*. Slight size distributions (20% variation) were used to reduce the interference ripples. This plot builds off Fig. 1 in [81], which finds that spheres in various ρ' regimes have slopes of -2 and -3, regardless of *R*. It is important to note that solid materials with *m*<1.1 are not naturally occurring [84].

Chapter 5 –Polarization Analysis

As previously mentioned, Cassini had both a Wide-Angle Camera (WAC) and Narrow Angle Camera (NAC) which took images during flybys of Enceladus. Both contained polarizing filters, but this work only discusses the NAC data. The only previous polarization data of Enceladus's surface comes from the Crimean Astrophysical Observatory and is shown in Fig. 5.1. The narrow range of phase angles is due to the geomety constraints of a ground-based telescope [85]. This means there is much to expand on in terms of the polarization of Enceladus' surface.

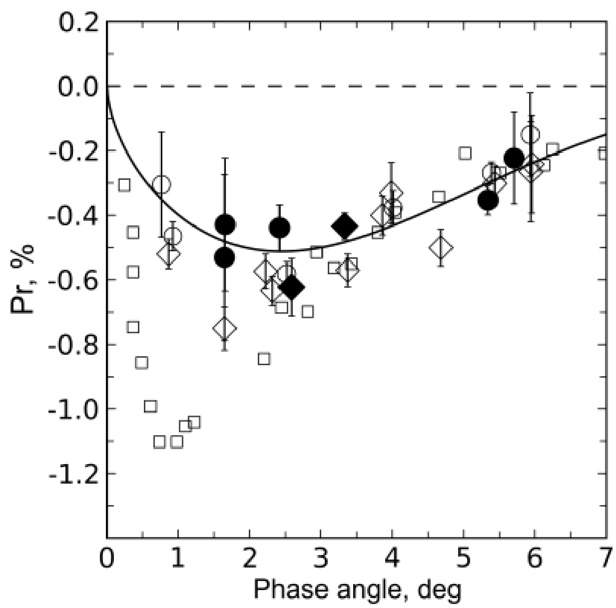

Figure 5.1. The polarization data of Enceladus's surface from the Crimean Astrophysical Observatory [85], where the y-axis denotes the percentage DoLP (Pr %). Enceladus' data is shown as the filled circles and diamonds. Enceladus was found to have a very low level of DoLP compared to other bodies in the solar system.

5.1 Image Reduction

Using the IDL code of West et al., and process created for Saturn's moon, Titan, the disk averaged percent of linear polarization is calculated for Enceladus [63]. Dividing the original 1398 NAC images into sets of three angles results in 466 total sets of images. The set of three angles is necessary to compute the total intensity I, the degree of linear polarization (DoLP), and the angle θ_p of the electric field vector that the polarized light makes with the NAC y-axis. The images are calibrated based on the transmission values calculated from the amount of light transmitted through the perpendicular and parallel components of the NAC. West et al. [63] shows how to derive the polarized and unpolarized components of the intensity from the measurements, under the idealization that all polarizers have the same transmission for polarized light:

$$I = I_{\mathrm{u}} + I_{\mathrm{p}} = \frac{2(I_0 + I_{60} + I_{120})}{3(T_1 + T_2)}$$

(5.1)

and

$$\theta = \frac{1}{2}\mathrm{Arctan}\left(\frac{3(I_{120} - I_{60})}{2\sin(120)\,(-2I_0 + I_{60} + I_{120})}\right)$$

(5.2)

where I is the total intensity of the image, I_u is the unpolarized component of the intensity, I_{p} is the polarized component, I_0, I_{60}, I_{120} are the intensities of each image of each respective angle, and T_1 and T_2 are the transmission values. The process of calibrating the transmission values for the Cassini polarizers which do not have identical transmission values and whose principal transmission axes are not perfectly aligned is explained in reference [86]. The IDL code incorporates these non-ideal factors.

Images are then sorted based on resolution, and no images worse than 2.5 km/pixel resolution are used due to their signal being too low. Images sets are also rejected if any image of the three in the set had detector readout issues such as missing lines. Saturated pixels, rings in the way of Enceladus' surface, and blurriness are all other reasons for rejection. If the saturated pixels were not on the disk of Enceladus, then the images were kept. If the saturated pixels were on the surface of Enceladus, then the image was unusable as saturation makes the polarization calculation inaccurate.

Because all three images in a set must be used together, many sets were unusable due to corruption of one or more of the images in the set. The list of images used in this work is provided in the appendix.

5.2 Polarization Calculations

The IDL code calculates the angle of the electric field vector as seen from the camera, not in terms of the scattering plane. The azimuthal angle of the sun in the image is used to convert the image plane to the reference plane of the scattered sunlight. The coordinate system used is that described in Fig. 2.9. The total polarization angle is the sun-image-azimuth angle plus the polarization angle in the camera θ_{p}. The sun-image-azimuth angle is different for each image, and is available in the image metadata on NASA's Planetary Data System (PDS) Outer Planet's Unified Search (OPUS) website [87]. This method was validated by replicating Titan's polarization in [86]. If the resulting angle is $\pm$ 0°, 180°, the polarization is considered negative (parallel to the scattering plane), and if it is $\pm$90°, 270°, then the polarization is consided positive (perpendicular to the scattering plane).

Enceladus' low level of polarization makes it difficult to tell if results are "real", so a second level of noise diagnostics and data removal is applied. If the resulting angles are close to the diagnonals of a polar plot (45°, 135°, 225°, or 315°), then those points were removed. The idea is that those points are neither perpendicular nor parallel to the scattering plane, so the polarization is not clearly positive or negative and results are probably due to noise. Out of the original 466 total sets of three, only 98 data points remain after data culling (46 GRN, 30 UV3, and 22 MT2).

The resulting polarization plots are shown in Fig. 5.2. Enceladus' surface has been found to have a low percent of linear polarization, due to its highly reflective nature. Even though both scattering and reflection polarize the incoming sunlight, the low amount of polarization is likely due to multiple scattering effects. In general, reflectivity and polarization are inversely proportional on planetary surfaces [88], [89]. This is called the Umov effect, and has been documented for planets, asteroids, as well as clouds of space dusts [90].

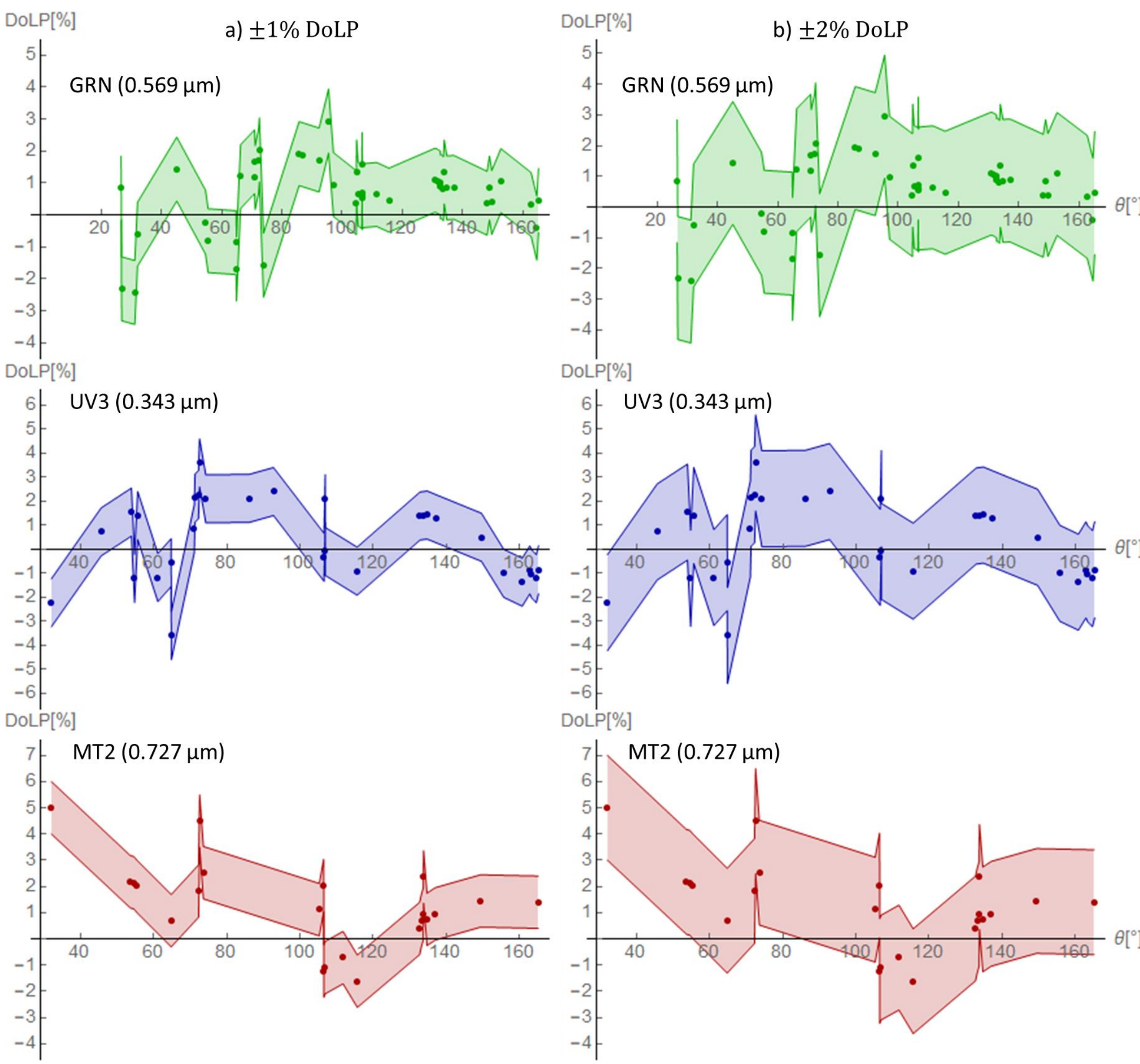

Figure 5.2. Disk-averaged percent DoLP of Enceladus' surface as photographed in three filters from the Cassini ISS NAC. The plots in column a) have constant error of $\pm$ 1% added, and plots in column b) have an error of $\pm$ 2%. We estimate the polarization uncertainty to be between $\pm$ 1-2% based on multiple measurements of Saturn's moon Titan (Fig. 12 of [86]). For the analysis in this work, $\pm$2% error is used.

Chapter 6- Results

The results of the simulations are discussed in this chapter for both the intensity data of the plumes and the disk averaged DoLP of Enceladus' surface. Several geometries and size distributions are simulated in ADDA and T-Matrix for both the light scattering and polarization studies.

6.1 Light Scattering Simulations

Using Q-Space analysis, [91] show that the particles in the cryovolcano plumes are likely to be larger than 2 μm in size, on average. This is talked about in depth in Section 4.2. Several size distributions for various geometries are simulated and compared to the CLR filter intensity data. We assume the particles are purely water-ice for computational simplicity. The spheres, spheroids, and cylinders are simulated with the single particle orientation-averaged T-Matrix code [49]. The hexagonal prisms are simulated in ADDA [22]. *EW'* is calculated from the outputted Mueller matrix.

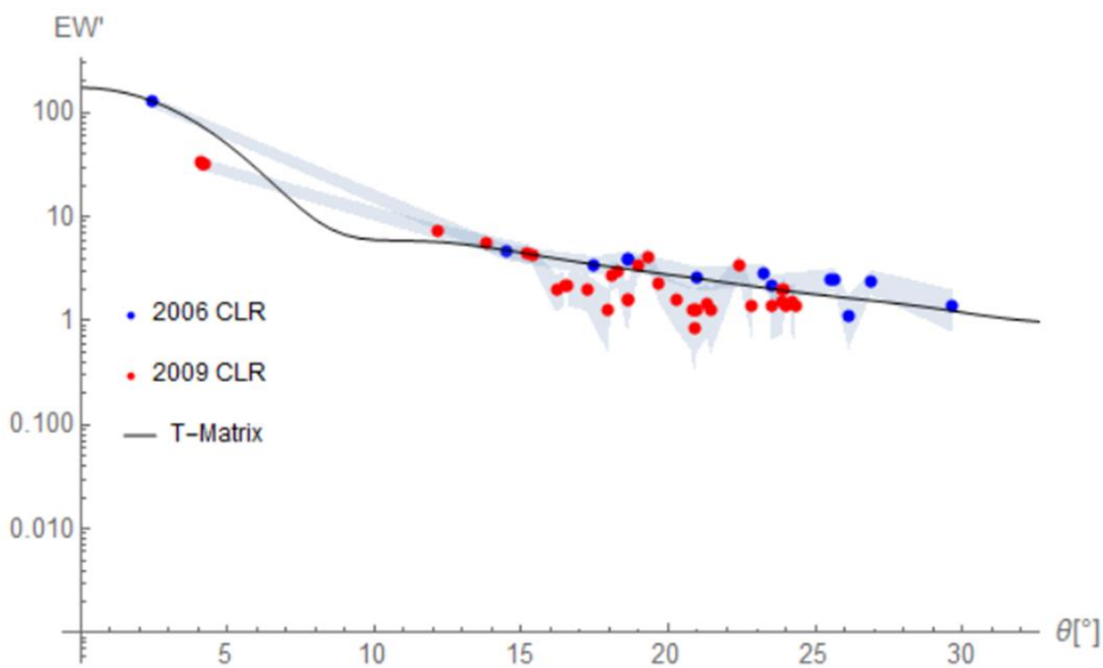

Figure 6.1. Polydisperse spheres made of water ice (m =1.309 + 3.4$\times 10^{-7}i$ [92]) simulated in T-Matrix for the Cassini NAC CLR filter (λ = 0.611 μm) compared to the CLR 2006 and CLR 2009 data. The size distribution shown is with mean μ=2 μm, standard deviation σ=20%, and size range r=0.001-8 μm. The Pearson correlation coefficients for this distribution are listed in Tables 6.1-6.2.

A metric is needed to quantify the goodness of fit of the simulated curves to the CLR data. The goodness of fit metric chosen is the Pearson correlation coefficient, c_{p}, which measures the strength and direction of the linear relationship between two data sets [93]. In signal processing, for example, Pearson coefficients are used with time lags to determine the cross-correlation between two signals [94]. It is normally denoted as r, but due to the variables used in this work, it will be referred to as c_{p}. For two data sets, x and y, the coefficient c_{p} is defined as:

$$c_{\mathrm{p}} = \frac{\sum(x_i - \bar{x})(y_i - \bar{y})}{\sqrt{\sum(x_i - \bar{x})^2 \sum(y_i - \bar{y})^2}}$$

(6.1)

Where x_i, y_i are values in the x and y samples, and $\bar{x}$, $\bar{y}$ are the means of the two data sets. The Pearson correlation coefficient can be explained as the ratio of the covariance of the data and the product of the two standard deviations. The correlation coefficient is normalized by the division of the standard deiviations so it ranges from -1 to +1. A value of 1 implies that the signals, in this case the simulated scattering curves and the Cassini data are identical, and a value of -1 implies that the signals are exactly opposite. The c_{p} values for different shapes and size distributions are listed in Tables 6.1-6.2. The CLR data from 2006 and 2009 are used for comparison due to having the largest observed scattering angle ranges.

As T-Matrix is designed for polydisperse particle simulations, it required no optimization beyond modifying the tolerances and parameters for each larger run. However, ADDA requires more computational resources for the largest simulations. Even on Kansas State University's high performance computing cluster, Beocat, simulating a hexagonal prism of volume equivalent radius r =4 µm takes several weeks. To speed up the process for large sizes, a Quasi-Monte-Carlo (QMC) orientation averaging scheme is applied. ADDA uses a lattice orientation averaging scheme by default, meaning it loops through nested lists of a predefined number of apha, beta, and gamma Euler angles. With the lattice method, thousands of single orientations are averaged, which drastically slows down the simulation time.

QMC orientation averaging schemes are much faster (10×-20×) than lattice schemes due to using quasi-random angles that optimize the orientation averaging so fewer single orientations are needed [95]. This idea is based off the work of [95], but applied to hexagonal prisms. The QMC scheme used here is a Halton sequence, i.e., a combination of two van der Corput sequences [96]. Van der Corput sequences are low-discrepancy sequences, also known as quasirandom, meaning that the points are close to being equidistributed. Quasirandom numbers cover the domain of interest more quickly and evenly than pure random numbers [97]. Halton sequences are useful because adding resolution simply involves adding more points to the end of the sequence, which is one of the reasons they are often used in Monte Carlo simulations. The van der Corput sequences used in this work are base two and base three.

In general, to rotate a simulated fixed-orientation particle, the particle is spun using the Euler angles: alpha, beta, and gamma. A lattice orientation average scheme loops over the angles to calculate thousands of orientations of the particle [22]. By choosing few specific orientations instead of looping through many, QMC averaging schemes require fewer computational resources.

With QMC, each orientation of the simulated particle can be calculated from the Halton sequence by converting each point to a pair of beta and gamma angles. Due to symmetry, beta ranges from 0°-180°, and gamma ranges from 0°-360°. Iterating over the alpha angle is computationally cheap, so it remains untouched from the lattice orientation averaging scheme and continues to loop over the pairs of angles [22]. The Halton sequence points, in conjunction with the alpha angle loop, provide many orientations which speed up the averaging process.

As [95] used spherical aggregates, testing was needed to ensure that the approximation held for hexagonal prisms. This work uses the same metric as their work to calculate the error in the approximation. The Mean Absolute Residual Error (MARE) is defined in Eq. (6.2):

$$\mathrm{MARE} = \frac{1}{181}\sum_{\theta=0}^{180^\circ} \frac{\left|S_{11}(\theta) - \widehat{S_{11}}(\theta)\right|}{S_{11}(\theta)} \tag{6.2}$$

Using the same notation as their work, $S_{11}(\theta)$ is the lattice orientation averaged S_{11}, and $\widehat{S_{11}}(\theta)$ is the QMC S_{11}. The differences are summed over 180° and divided by the number of points. The MARE of hexagonal prisms of various volume equivalent radii are shown in the contour plot of Fig. 6.7. The error is very small for a large number of sequence points. For each hexagonal prism in the size distribution larger than *r*=4 in this work, thirty QMC points are used.

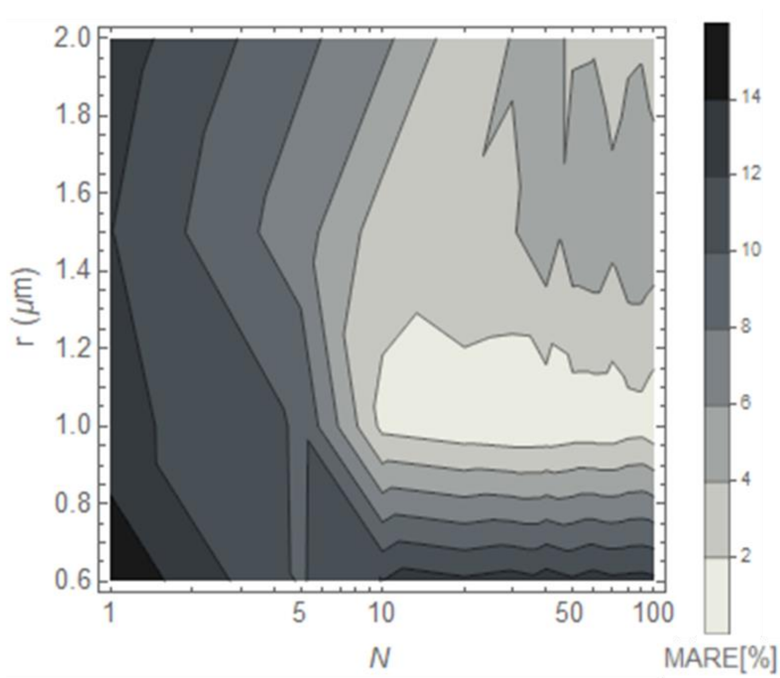

Figure 6.2. A contour plot showing the percent error in the approximation, calculated by simulating multiple hexagonal prisms of volume-equivalent radii from 0.6-2 μm with QMC points from 1-100 and comparing to ADDA's lattice orientation averaging scheme. This is based on Fig. 4 in [95]. Darker shading corresponds to higher error and vice versa. The MARE tends to decrease as size increases, as well as when the number of averaging points N increases for larger sizes.

2006 CLR	***μ*=2 μm, *σ*=20% *r*=0.001-8 μm**	***μ*=4 μm, *σ*= 20% *r*=2-8 μm**
Sphere	0.674	0.548
Spheroid (*D/L*=0.5)	0.685	0.561
Spheroid (*D/L*=2)	0.667	0.574
Cylinder (*D/L*=1)	0.681	0.559
Hexagonal Prisms (*D/L*=1)	0.629	0.561

Table 6.1. The Pearson correlation coefficients of the curves for polydisperse geometries made of water ice, m =1.309 + 3.4$\times 10^{-7} i$ [92]. These are simulated with λ = 0.611 μm, or the Cassini NAC CLR filter in ADDA and T-Matrix.

2009 CLR	***μ*=2 μm, *σ*=20% *r*=0.001-8 μm**	***μ*=4 μm, *σ*= 20% *r*=2-8 μm**
Sphere	0.698	0.761
Spheroid (*D/L*=0.5)	0.733	0.771
Spheroid (*D/L*=2)	0.715	0.793
Cylinder (*D/L*=1)	0.726	0.758
Hexagonal Prisms (*D/L*=1)	0.732	0.714

Table 6.2. The same as Table 6.1 but compared to the CLR 2009 data.

While these numbers are close to the ideal of c_p= +1, they should be taken with a grain of salt due to the narrow range of angles and amount of reduction done to the intensity data. For both sets of data and size distributions, the spheroids have the highest correlation coefficients. This agrees with the non-sphericity made in Section 4.2.

6.2 Polarization Simulations of Single Particles

Enceladus is an icy body with a surface temperature of ~70 K [32]. However, a global liquid ocean has been detected by Cassini, meaning that the crovolcano-plume particles must change phase from liquid to solid somewhere between the bottom of the cryovolcano vent and the surface of Enceladus. Light scattering analysis of the plume data limits the average particle volume equivalent radius in the plumes to be greater than 2 μm [98]. Assuming the particles freeze at the surface means they are likely to be hexagonal prisms and will be too cold to aggregate [72].

The DoLPs of several particle shapes and sizes are listed in Fig. 6.1-6.6. We assume the particles are purely water-ice for computational simplicity and because most research in Table 3.1 agrees. The spheres, spheroids, and cylinders are simulated with the single particle orientation-averaged T-Matrix code [49]. The hexagonal prisms are simulated in ADDA [22]. Both use a refractive index of $m = 1.31 + 4.75\times 10^{-7}i$ [92] and λ =0.569 μm to match the GRN filter. The ADDA simulations use a constant dipoles per lambda (DPL) value of DPL=15 to ensure computational accuracy. The volume-equivalent radii in Figs. (6.1)-(6.4) are chosen to show the changes in DoLP at relevant sizes: $r < \lambda$, $r \approx \lambda$, $r > \lambda$, and $r >> \lambda$.

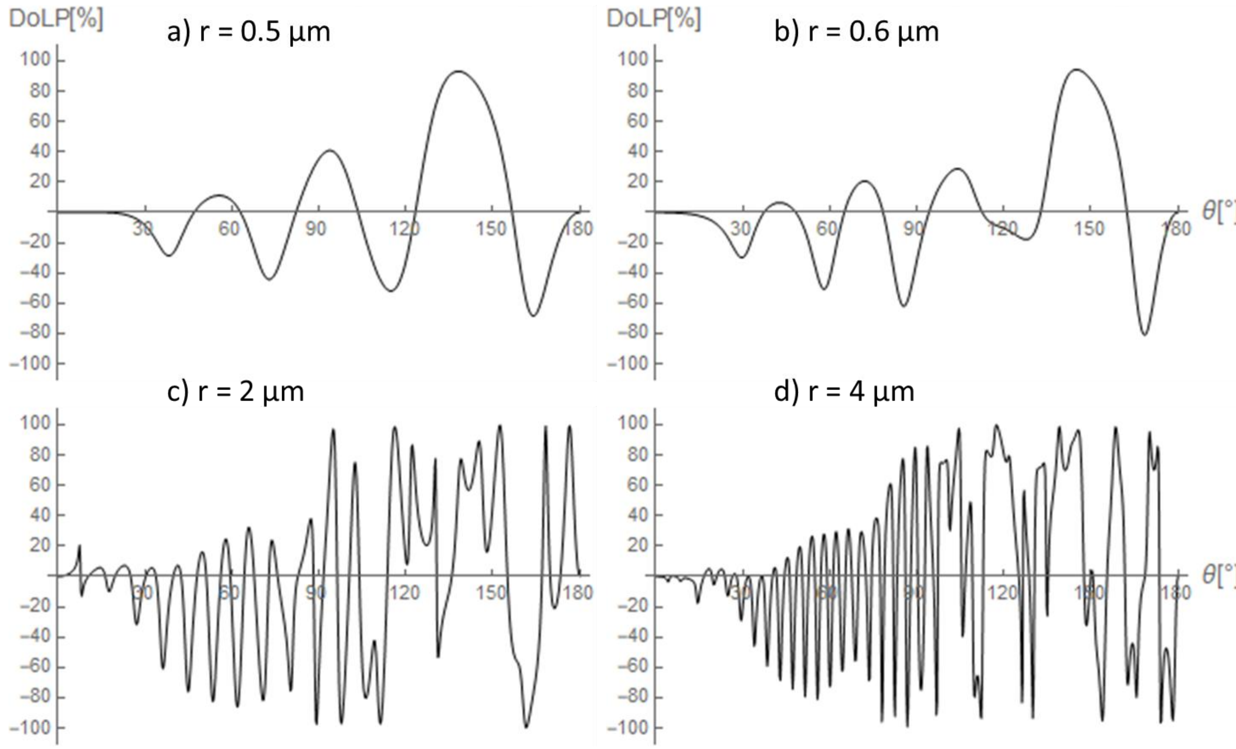

Figure 6.3. The polarization of monodisperse spheres of various sizes made of water ice, m =1.31 + 4.75× 10^{-7}i [92]. These are simulated with λ = 0.569 μm, or the Cassini GRN filter. Size increases from a)-d), starting at *r*< λ to *r*>> λ. Spheres have near-zero polarization at small scattering angles and can fully polarize the scattered light (DoLP=100%). The amount of rippling increases with increasing size.

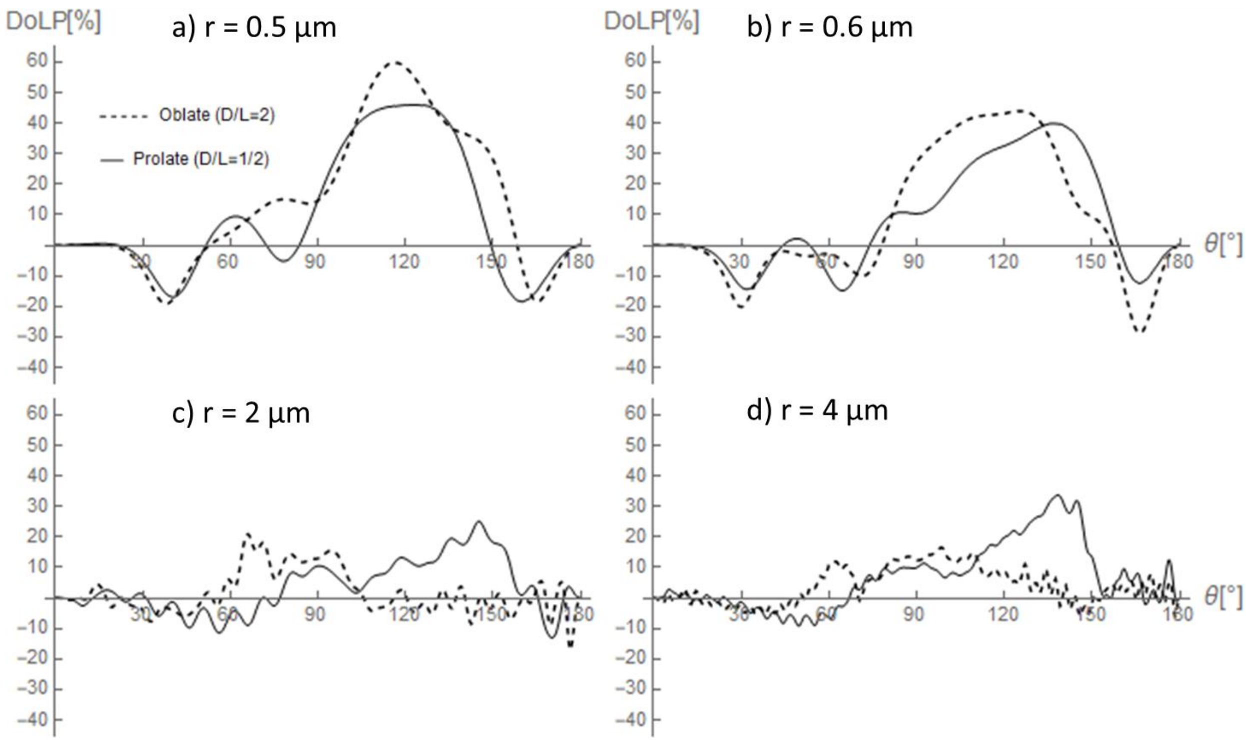

Figure 6.4. The same as Fig. 6.3 except for orientationally averaged monodisperse oblate and prolate spheroids The aspect ratios, i.e. diameter/length, *D/L*=1/2 and *D/L*=2 are chosen to show the effects of non-sphericity. A ratio of *D/L*=1 equates to a sphere. The amount of ripples increases with size. Unlike spheres, the DoLP does not oscillate as wildly between negative and positive values. Spheroids polarize light more positively than do spheres of the same size but do not polarize as strongly. However, like spheres, spheroids also have near zero-polarization at small scattering angles.

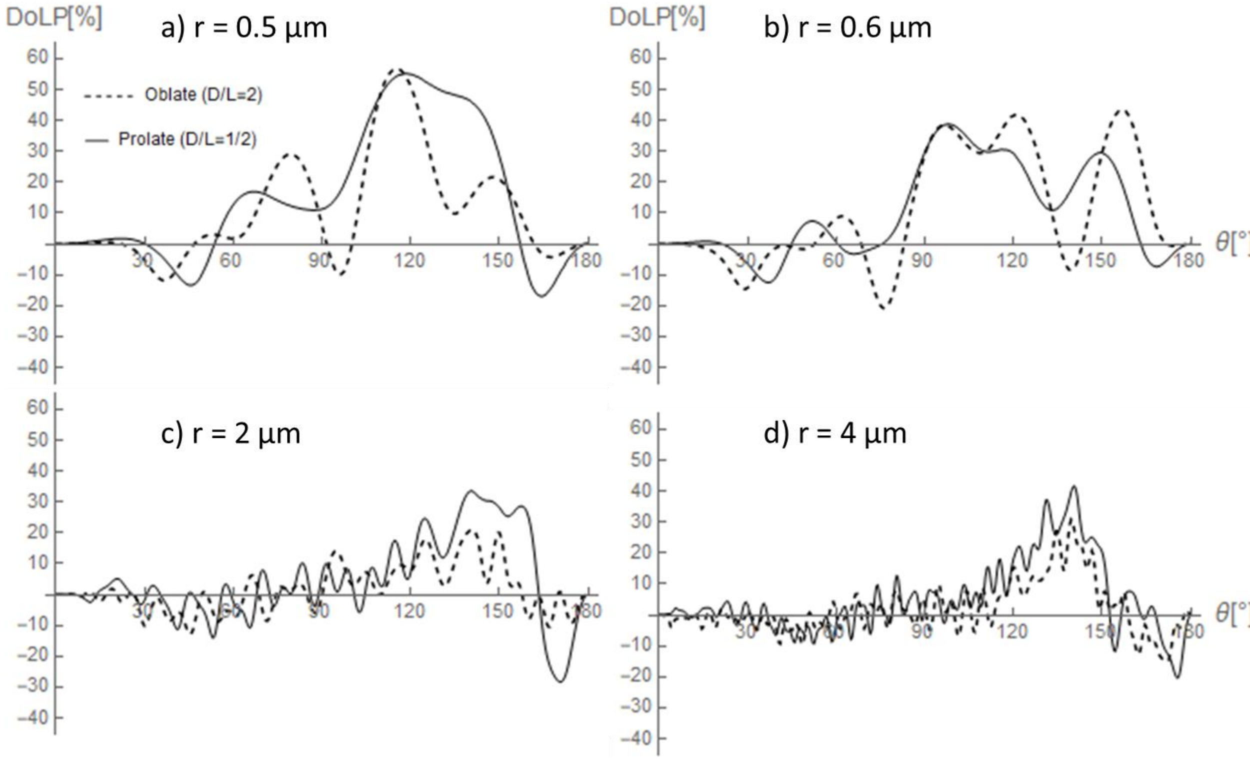

Figure 6.5. Same as Fig. 6.3 except for oblate and prolate cylinders. Note that the amount of ripples increases with size and cylinders do not polarize as strongly as spheres.

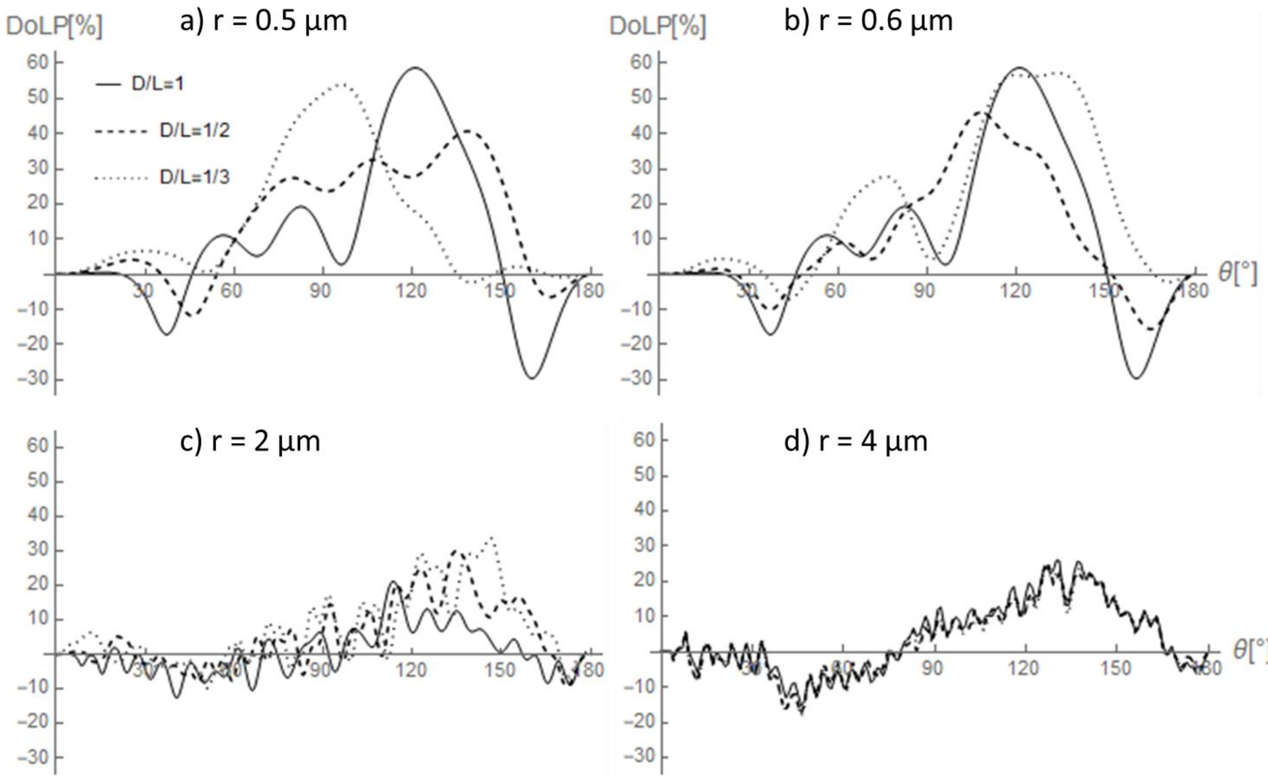

Figure 6.6. Same as Fig. 6.3 except for hexagonal prisms. These are simulated in ADDA with DPL=15 and $\lambda = 0.569$ µm. The aspect ratios D/L are chosen to show the effects of non-sphericity. The amount of ripples increases with increasing size while the maximum DoLP decreases, and it appears that the aspect ratios differ less at larger sizes.

6.3 Polarization Simulations of Size Distributions

While monodisperse particle simulations are useful to understand the behavior of the DoLP with respect to size and shape, the particles on the surface of Enceladus will be polydisperse and must be described using a size distribution. As aersosols on Earth tend to follow a log-normal size distribution [11], a log-normal distribution is chosen as the basis of this model. Since smaller particles escape to the E-ring, and larger particles fall back to the surface, a truncated log normal distribution is needed to exclude smaller sizes. The lower size limit is unknown as all that is known is that it exists. Assuming the particles are ice crystals, a halo would be seen if the particles are larger than 8-15 µm in radius for the filters used on Cassini [99]. As no halo has been detected on Enceladus, this provides an upper limit.

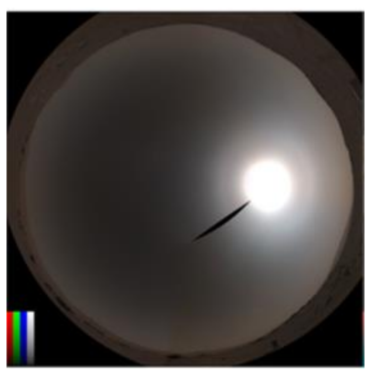

Figure 6.7. A halo as seen on Mars photographed by the perseverence rover, caused by sunlight scattering off ice in the Martian atmosphere. This image is taken from [100].

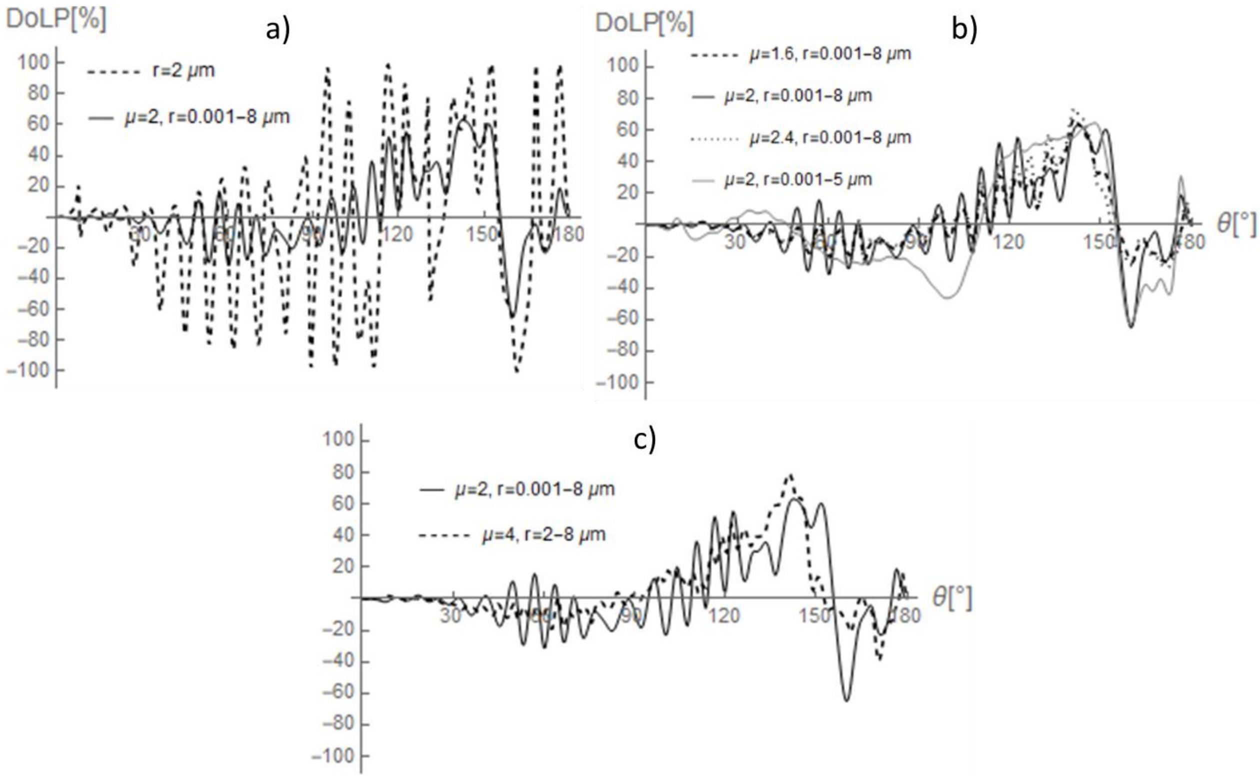

Figure 6.8. a) Simulated polarization curves for a single spherical ice particle with r=2 μm compared with a lognormal size distribution of spherical ice particles with a mean size of μ=2 μm. b) Simulated polarization curves from log-normal size distributions of spheres showing the sensitivity to a change in mean and range of the distribution. The 20% change in mean radius does not affect the overall shape of the curve as much as truncating the distribution. As shown in both plots, the size distributions have a much smaller magnitude DoLP compared to the single particle. This is likely due to interference of the ripples.

As [95] used spherical aggregates, testing was needed to ensure that the approximation held for hexagonal prisms. This is the same process as used in Section 6.1 for the S_{11} elements but for DoLP. This work uses the same metric as their work to calculate the error in the approximation. The Mean Absolute Error (MAE) is defined in Eq. (6.3):

$$\mathrm{MAE} = \frac{1}{181}\sum_{\theta=0}^{180^\circ}\left|DoLP(\theta) - \widehat{DoLP}(\theta)\right| \qquad (6.3)$$

Using the same notation as their work, $DoLP(\theta)$ is the recorded DoLP, and $\widehat{DoLP}(\theta)$ is the predicted DoLP. The differences are summed over 180° and divided by the number of points. The MAE of hexagonal prisms of various volume equivalent radii are shown in the contour plot of Fig.

6.8. The error is very small for a large number of sequence points. For each hexagonal prism in the size distribution larger than r=4 μm in this work, thirty QMC points are used.

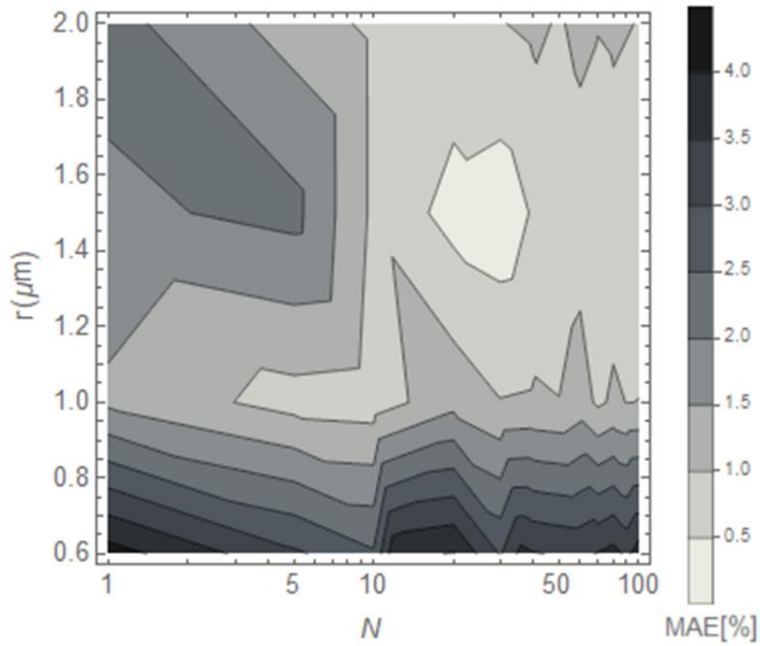

Figure 6.9. The same as Fig. 6.2 but for DoLP. This is based on Fig. 4 in [95]. Darker shading corresponds to higher error and vice versa. The MAE tends to decrease as size increases, as well as when the number of averaging points N increases for larger sizes.

6.4 Polarization Analysis

The goal of this project is to limit the scope of possibilities and find trends that may lead to information in the future. Due to computational limits, there are some possibilities that cannot be simulated with the current infrastructure. The way around this is to simulate the possibilities that require fewer resources and test ideas of trends on them and save the largest simulations for when more resources are available. Basically, test on all the cheap runs so there are fewer expensive runs needed later.

The computationally cheapest geometries are the spheres and spheroids. Although it is unlikely for the particles to be near spherical, they can be used to study the effects of changing size distribution parameters. The assumption is that the other geometries should behave similarly to the spheres about effects of distribution width, etc.

The spheroids are not as computationally cheap as the spheres but run on quick enough timescales to be useful for effects of size distribution variation as well. Spheroids are also advantageous due to being able to test the effects of different aspect ratios. The most expensive geometries are the least spherical: the cylinders and the hexagonal prisms. That is why the cylinders and hexagonal prisms have the fewest combinations of parameters as listed in the tables below.

The Pearson correlation coefficient, c_{p}, is used like in Section 6.1 to make a conclusion on which simulated particle size and morphology best matches the data. Because T-Matrix and ADDA are single scattering codes, a multiple scattering approximation is needed. This is done by normalizing the Cassini data and the simulated polarization curves of each particle to 1 by dividing by the maxium polarization value. As found in [28], going from single to multiple scattering reduces the polarization by nearly a factor of 10 and shifts the position of the maximum polarization peak. Normalizing to 1 helps remove the multiple scattering aspect (the lowering of maximum DoLP), and compares the behaviors of the curves. If the simulated data has a peak where the Cassini data has a trough, then it is clear that the simulated size, shape, or particle distribution does not agree.

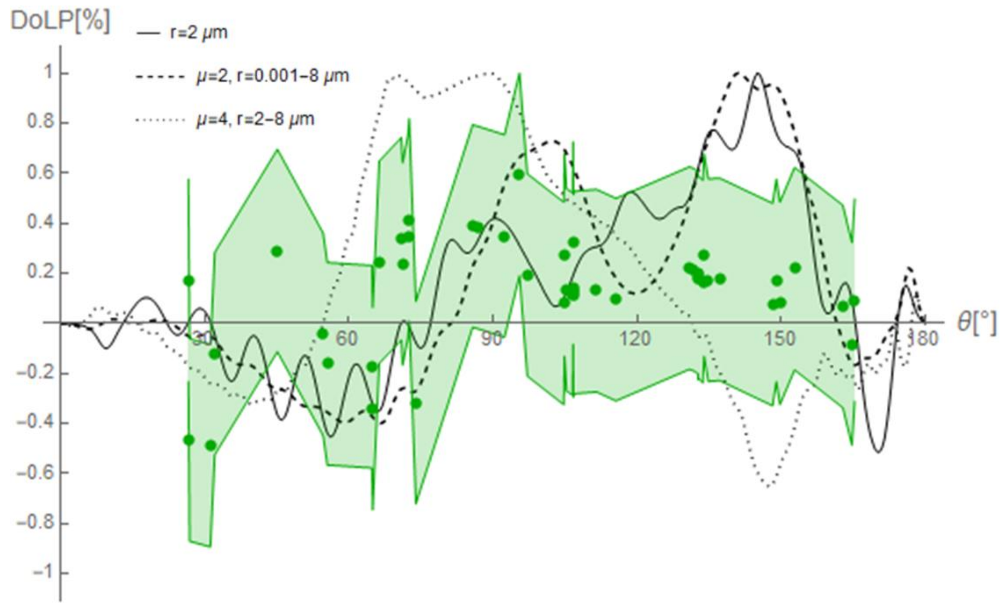

Figure 6.10. An example of the process outlined above using prolate spheroids. The spheroids are simulated in T-Matrix for water ice, m =1.31 + 4.75× $10^{-7}i$ [92] and with λ = 0.569 µm, or the GRN filter. The simulated curves and GRN data are normalized to one by dividing all points by the maximum DoLP value of each respective curve. Several of the peaks do not align with the peaks of the data, reducing the corresponding c_{p} value of the curves.

Several parameters are varied in the simulations. They are shape, size range, standard deviation, and mean of the size distributions. Not all combinations were simulated, especially not for cylinders or hexagonal prisms due to their computational cost. The changing parameter in each table is written in red.

Effects of shape:

The DoLPs of same geometries as in section 6.1 are simulated and compared via the Pearson correlation coefficient in two NAC filters, GRN and MT2. The table compares the monodisperse geometries to two size distributions for each geometry. The first size distribution (μ=2 µm, σ= 20%, r=0.001-8 µm) was a starting point as Q-space indicates a mean radius of 2 µm. The second size distribution (μ=4 µm, σ= 20%, r=2-8 µm) takes into account the fact that the smaller grains escape to the E-ring, so even if the plumes have a mean size of 2 µm, the surface should have a larger mean. It is unknown exactly what size particles fall back to the surface, so 2 μm was taken as a simple cut off. All geometries are simulated as water ice with the respective wavelength dependent refactive indices as explained in [92].

GRN	***r* = 2 μm (single)**	***μ* = 2 μm, *σ* = 20% *r* = 0.001-8 μm**	***μ* = 4 μm, *σ* = 20% *r* = 2-8 μm**
Sphere	0.131	0.114	0.203
Spheroid (*D*/*L*=0.5)	0.352	0.384	0.230
Spheroid (*D*/*L*=2)	0.269	0.275	0.230
Cylinder (*D*/*L*=1)	0.232	0.224	0.195
Hexagonal Prism (*D*/*L*=1)	0.261	0.474	0.372

Table 6.3. The Pearson correlation coefficients for geometries and size distributions as simulated in the GRN filter (0.569 μm) in T-Matrix and ADDA. These are the same distributions and geometries as Table 6.1-2.

.

MT2	***μ* = 2 μm, *σ* = 20% *r* =0.001-8 μm**	***μ* = 4 μm, *σ* = 20% *r* = 2-8 μm**
Sphere	-0.414	-0.275

Spheroid (*D/L*=0.5)	-0.548	-0.417
Spheroid (*D/L*=2)	-0.094	-0.159
Cylinder (*D/L*=1)	-0.548	-0.607
Hexagonal Prisms (*D/L*=1)	-0.708	-0.632

Table 6.4. The same as Table 6.3, but simulated in the MT2 filter (0.727 µm) in T-Matrix and ADDA. The monodisperse particles were not simulated in MT2 to save on computational time as it is unlikely the surface particles are present at all one size.

Within the two size distributions evaluated above for all shapes in two filters, it appears that the hexagonal prisms agree the best. The μ=4 µm, σ= 20%, r=2-8 µm distribution is shown in Fig. 6.9. However, the hexagonal prism size distributions are less precise, i.e. the mean and standard deviation are not exact, as they are not solved analytically like the other geometries are in T-Matrix. Taking that into account, along with the monodisperse correlation coefficients, the *D/L*=0.5 spheroid seems to work best. However, the correlation coefficients still are low compared to the ideal of +1, meaning that the best fitting geometry is likely less spherical than an aspect ratio of *D/L*=1/2 or 2/1. A high aspect ratio cylinder or a higher aspect ratio spheroid would be a good test for this idea.

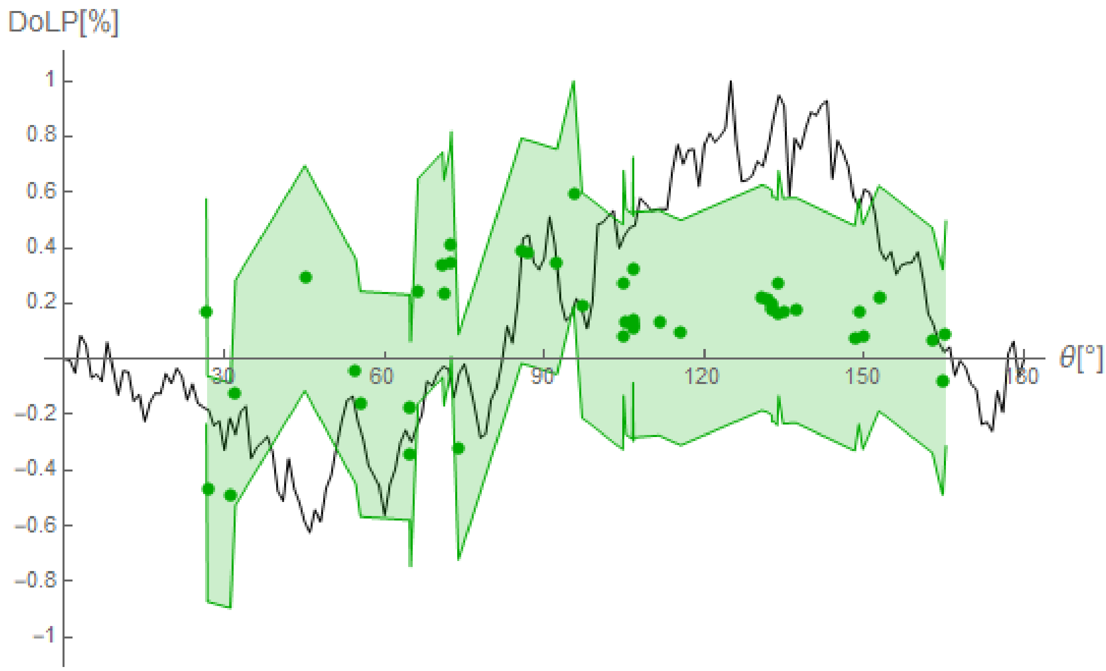

Figure 6.11. Normalized DoLP of polydisperse hexagonal prisms in a lognormal size distribution with size ranging from 2-8 μm and a mean of 4 μm compared to the GRN polarization data. These are simulated with ADDA with m =1.31 + 4.75× $10^{-7}i$ [92] and λ = 0.569 μm, and are the most computationally intensive of the study, which is why the QMC orientation averaging scheme is used. Thirty runs for each of the larger sizes in the distribution are used to reduce the error from the QMC approximation. Before normalization, the simulated curve is assumed to have an mean average error of approximately 10%, due to smaller errors being added for every large size in the size distribution.

Effects of changing the mean:

GRN	*r* = 2 μm (single)	*μ* = 2 μm σ = 20% *r*=0.001-8 μm	*μ* = 1.6 μm σ = 20% *r*=0.001-8 μm	*μ* = 2.4 μm σ = 20% *r*=0.001-8 μm
Sphere	0.131	0.114	0.144	0.039

Table 6.5. Pearson correlation coefficients of a 20% change in mean for spheres with a control of μ =2 μm and a distribution size range of r=0.001-8 μm and also compared to a monodisperse distribution as simulated for water ice, m =1.31 + 4.75× $10^{-7}i$ [92] in the GRN filter (λ =0.569 μm).

For spheres, at least, it appears that slightly decreasing the mean increases the correlation coefficient. This information by itself does not help narrow down the possibilities by much, as the correlation coefficients are still not close to +1.

Effects of increasing the standard deviation:

The effect of increasing the standard deviation is tested in both the GRN and MT2 filters, with various size distributions. Only one parameter (standard deviation σ) changes within each table, although each respective table contains results for a different control distribution.

GRN	**r = 2 µm (single)**	**μ = 2 µm, σ = 20% r = 0.001-8 µm**	**μ = 2 µm, σ = 50% r = 0.001-8 µm**
Spheroid (*D/L*=0.5)	0.352	0.384	0.420
Spheroid (*D/L*=2)	0.269	0.275	0.301
Cylinder (*D/L*=1)	0.232	0.224	0.216

Table 6.6. The effects of widening the size distributions, i.e. increasing the standard deviation from 20% to 50% of the mean, as simulated for three geometries (both spheroids and the cylinder) in the GRN filter. The distributions are also compared to the monodisperse distribution, which would technically be considered to have a standard deviation of 0%. The wider distributions increase the Pearson coefficient except for the cylinders.

GRN	**μ = 4 µm, σ = 20% r = 2-8 µm**	**μ = 4 µm, σ = 50% r = 2-8 µm**
Sphere	0.203	0.270

Spheroid (*D/L*=0.5)	0.230	0.301
Spheroid (*D/L*=2)	0.225	0.230
Cylinder (*D/L*=1)	0.195	0.194

Table 6.7. The effect on the correlation coefficient of widening the distributions by increasing the standard deviations σ from 20% to 50% of the mean as shown in the GRN filter and for μ=4 µm with size range r=2-8 µm. For spheres and spheroids of D/L=0.5 and D/L=2, increasing σ increased the correlation coefficent. However, for cylinders, the increase in σ slightly decreased the coefficient.

GRN	***μ* = 4 µm, *σ* = 50% *r* = 0.001-8 µm**	***μ* = 4 µm, *σ* = 80% *r* = 0.001-8 µm**
Spheroid (*D/L*=2)	0.244	0.253

Table 6.8. The correlation coefficients of increasing σ even more, from 50% to 80% of the mean, in a distribution of (μ=4 µm, r=0.001-8 µm) for D/L=2 spheroids in GRN. The increase in σ increases the correlation coefficient as well.

The increase in σ increased the correlation coefficients for all tested geometries except cylinders for the GRN filter simulations. For cylinders, the increase in σ only slightly reduced the correlation coefficient. The MT2 results are listed below in Tables 6.9-6.10.

MT2	***μ* = 2 µm, *σ* = 20% *r* = 0.001-8 µm**	***μ* = 2 µm, *σ* = 50% *r* = 0.001-8 µm**
Sphere	-0.414	-0.392
Spheroid (*D/L*=0.5)	-0.548	-0.410

Spheroid (*D/L*=2)	-0.209	-0.205
Cylinder (*D/L*=1)	-0.548	-0.544

Table 6. 9. The results of increasing σ from 20% to 50% of the mean in the MT2 (λ=0.727 µm) filter with distribution parameters (μ=2 µm, r=0.001-8 µm). This table should be compared to Table 6.6 for GRN, but does not include the monodisperse μ=2 µm column.

MT2	**μ = 4 µm,** **σ = 20%** **r = 2-8 µm**	**μ = 4 µm,** **σ = 50%** **r = 2-8 µm**
Sphere	-0.275	-0.406
Spheroid (*D/L*=0.5)	-0.417	-0.411
Spheroid (*D/L*=2)	-0.159	-0.200
Cylinder (*D/L*=1)	-0.607	-0.497

Table 6. 10. The same as Table 6.7 but for MT2, λ=0.727 µm.

For the MT2 filter simulations, λ=0.727 µm, increasing σ increases the correlation coefficients for each geometry for the size distribution (μ=2 µm, r=0.001-8 µm) in Table 6.9. However, for the (μ=4 µm, r=2-8 µm) distribution in Table 6.10, the correlation coefficient increased (became more positive) only for the cylinders and the D/L=2 spheroids with the increase in σ.

For most geometries in the tested distributions (Tables 6.6-6.11), increasing σ increases the correlation coefficient, i.e., causes the simulated curves to agree better with the DoLP data in the GRN and MT2 filters. However, the MT2 correlation coefficients are still negative, implying that these distributions do not agree with the surface data well. While increasing σ helps, the correlation coefficients are still too low to consider any of these distributions as a true possibility for the particles.

Effects of truncating distributions:

GRN	r = 2 µm (single)	μ = 2 µm σ = 20% r=0.001-8 µm	μ = 2 µm σ = 20% r=0.001-5 µm	μ = 2 µm σ = 50% r=0.001-8 µm	μ = 2 µm σ = 50% r=0.001-15 µm
Sphere	0.131	0.114	0.141	0.181	0.356

Table 6.11. The effect on spheres of truncating and extending the size ranges of two size distributions, as simulated in the GRN filter. The first distribution changed is the control distribution (μ=2 µm, σ=20%, r=0.001-8 µm), which is truncated at 5 µm. The truncation point of 5 µm was chosen arbitrarily. The second distribution changed is the same as the control, but with a larger standard deviation. There, the distribution was extended from 8 to 15 µm, as opposed to truncated. The change in standard deviation from 20% to 50% is due to computational limits with larger sizes.

GRN	μ = 4 µm, σ = 50% r = 0.001-8 µm	μ = 4 µm, σ = 50% r = 2-8 µm
Spheroid (*D/L*=0.5)	0.426	0.301
Spheroid (*D/L*=2)	0.244	0.225
Cylinder (*D/L*=1)	0.199	0.194

Table 6.12. The effects of truncating the size distribution, as demonstrated for three geometries (both spheroids and cylinder) for the GRN filter.

Tables 6.11-6.12 show the effects of truncating distributions. Table 6.11 shows a dramatic increase in the correlation coefficient for the size distribution with μ=2 µm, σ=50% and size range of r=0.001-15 μm. However, it also seems that limiting particles to smaller than 5 μm also increases the correlation coefficient relative to the control distribution. The increase is much more dramatic (nearly a factor of 2) for increasing the size range to 15 μm. Table 6.12 shoes that truncating the size range to exclude particles of r<2 μm decreases the correlations across the board for the spheroids and cylinders for the (μ=4 μm, σ= 50%) distibution.

These results along with the results from increasing the standard deviations may imply that the particles on Enceladus' surface are present in a larger range of sizes than were tested. Also, even though only the larger particles settle to Enceladus' surface, it is possible that capping the distributions at r>2 μm might be too extreme. Perhaps having a lower limit of 0.5 or 1 μm might be more helpful in future tests. As long as the mean of the distrbutions is μ>2 μm, this still agrees with Q-space.

Chapter 7 – Conclusion

7.1 Conclusions About Shape and Size

The results from Q-space analysis served as a starting point for the simulations, and then the simulations were refined based on the Pearson coefficients of previous ones. The results from Chapter 6 must be considered all together as the best fitting geometry or size distribution cannot be considered correct unless it agrees in all filters. Among the three color filters tested, the hexagonal prisms in the distribution with mean μ=2 µm, σ=20%, and range r=0.001-8 µm performed relatively well. Regardless of distribution, the D/L=0.5 spheroid geometry often had higher correlation coefficients than the other geometries.

As Section 4.2 gives evidence for the particles to not be spherical via Q-Space analysis, Sections 6.2-6.4 give evidence via DoLP values. Spheres polarize too strongly to be present on Enceladus' surface. The fact that the hexagonal prisms and spheroids performed the best throughout the distribution studies in Section 6.4 also gives evidence for non-sphericity.

With the distribution parameters tested (mean, standard deviation, and size range), several trends appeared. For several geometries, increasing the standard deviations to be a larger percentage of the mean increased the correlation coefficients. Increasing the size range to be more inclusive of smaller and larger particles appeared to increase the correlation coefficients as well.

These findings, in conjunction with the findings of the other groups in Table 3.1, point to the surface particles being in a larger range than between 2-8 µm, and possibly larger than those that would make a halo as well. Roughness, possibly from the ejection out of the vents or the fall to the surface, may be why there is no halo [71], [99], [100]. The limit of particles on the surface occurring at r>2 µm may be too harsh, but r>0.001 µm may be too inclusive. The particles are likely not spheres, and the success of the simulated spheroids and hexagonal prisms may imply the particles have high aspect ratios. The difference in correlation coefficients between the GRN and MT2 filter simulations may imply that there are impurities in the water ice, such as dust, silica, ammonia, or other materials. Also, because the spheres and spheroids had positive correlation coefficients in most filters and distributions, that could be a sign that amorphous ice is present. Amorphous ice has a different refractive index at the temperatures present on Enceladus (m = ~1.24+0.002i [101]), so more testing is needed.

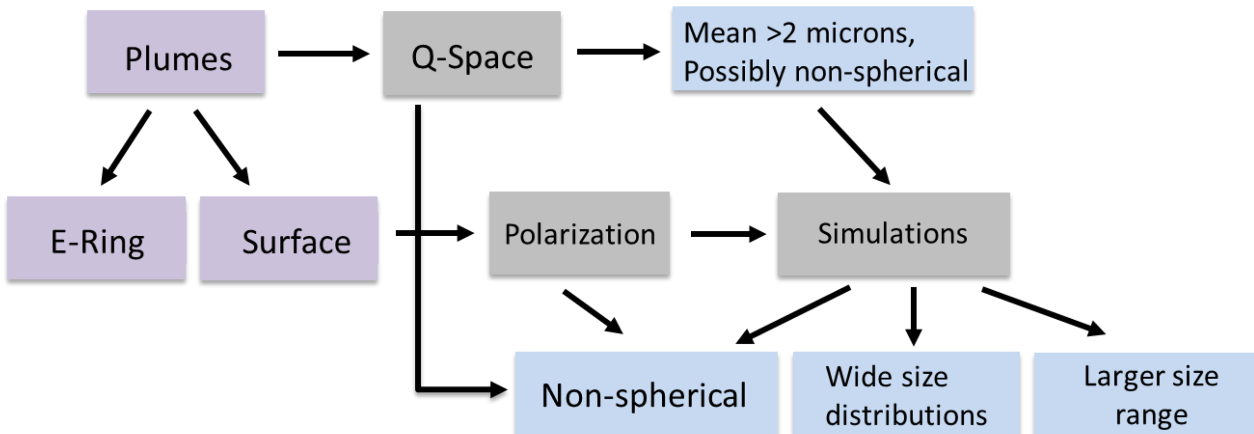

Figure 7.1. A flow chart of the results of this work. Data locations are shown in lavender, methods are shown in grey, and the results are in light blue.

The total size range analyzed in this work is r = 0.001-15 μm, but the best fitting simulations point to a size range near r = 2-8 μm for the surface particles. While many of the r = 0.001-8 μm simulations performed better than their counterparts in the GRN filter, the MT2 shows the opposite effect. However, it is likely that the lower limit for the size range is between 0.001-2 μm, and so future size ranges should not be truncated at a lower limit of 2 μm. The size range constrained by the best fitting simulations in this work is plotted on Fig. 7.2, an extension of Fig. 3.2. with a dashed purple line to represent Kansas State University. The range fits well among the ranges from other research groups.

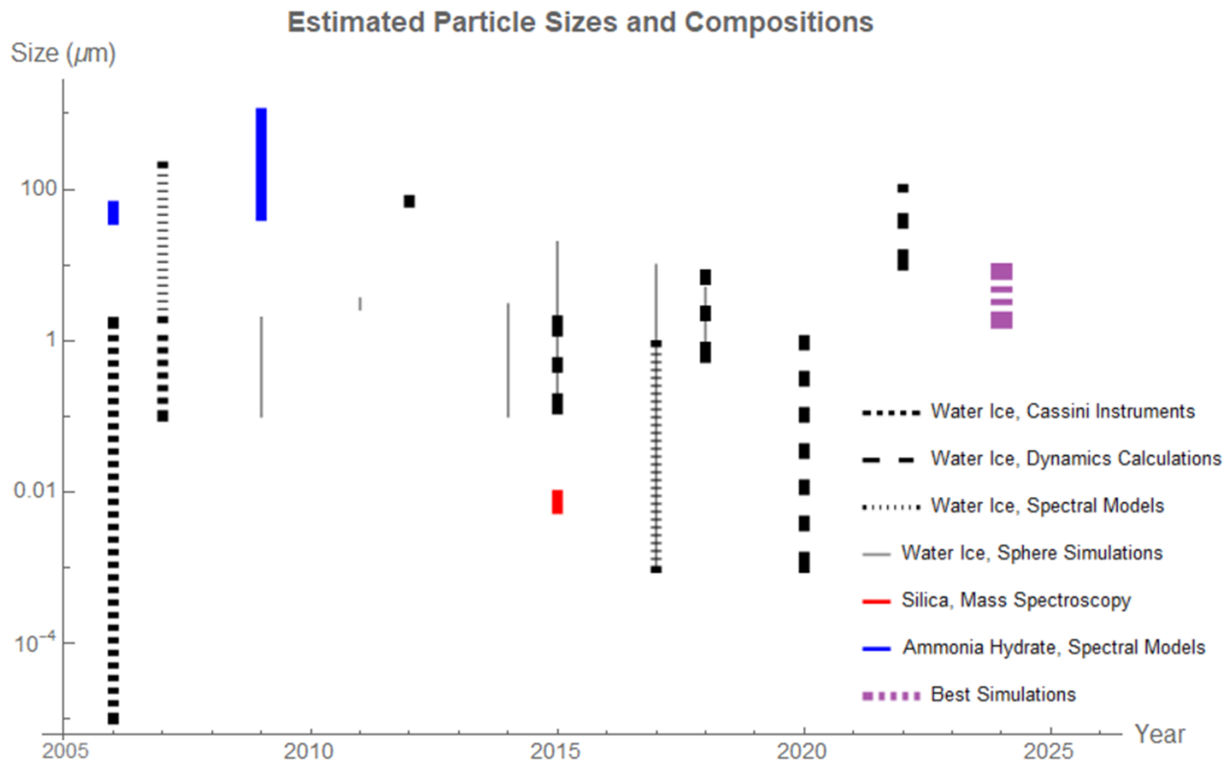

Figure 7.2: The same plot as Fig. 3.2, but with the best size distributions simulated here shown as a dashed line in Kansas State University Purple.

7.2 Mission Recommendations for the Future

The Cassini spacecraft was incredibly high-tech for its time, but as of time of writing, it was launched 26 years ago. There have been many technological advances since the 1990s and much information learned. Since the discovery of the cryovolcanoes and the subsurface ocean, many scientists have wanted to go back to Enceladus to study it more in depth. NASA's Enceladus Orbilander is a proposed convertible satellite-rover mission, which, at the earliest, will launch in 2038 and not reach Enceladus until the 2050's [65]. Unfortunately, due to budget constraints, it is very possible for this mission to be pushed back or scrapped altogether. This means that there are at least 14 years from the time of writing this dissertation to launch, which is enough time to add and change instruments on the craft.

The Orbilander's current mission plan is to orbit Enceladus for 200 days, with some of that time flying through the cryovolcano plumes and looking for safe place to land [102]. The first mission recommendation is to send a probe or rover to Enceladus' South Pole, especially one with drilling capabilities. While the ocean on Enceladus is thought to cover the entire body, landing in the South Polar Terrain (SPT) will provide the most insight. With current technology and spacecraft speeds, it would be near impossible to retrieve sediment from the surface and bring it back to Earth. Cassini took over six years to reach Saturn, and Voyager 1 and 2 took a little over three years [103]. The amount of fuel needed for a two-way journey is currently unreasonable for human space travel to the gas giants. This means the rover would have to analyze sediment in-situ or relay photographs and spectral data to Earth. A rover would also be able to go near the vents and possibly peer inside to learn about the eruption mechanism. With drilling capabilities, the rover could map the depth of Enceladus' icy crust and confirm the reason for the Tiger Stripes to only be on the SPT as inferred by [104], [105]. Testing the liquid under the surface of Enceladus would provide the most significant data of the whole mission. That way, the ocean can be studied directly and not via secondary measurements such as light scattering of the plumes. A PH balance measurement, an image of the liquid under a microscope, as well as mass spectroscopy will all be of significant help to understand Enceladus and its geological mechanisms.

While a lander is the most helpful way to study Enceladus, it poses many more challenges than a satellite does. It will be very difficult for a rover to drive near the vents with how icy and fractured the tiger stripes are. It is also currently unknown how deep the fissures go, so it is very possible for a rover to get stuck or fall in completely. This means a spacecraft that does not land may be more feasible, especially with budget constraints. As Cassini was so successful, a couple improvements to it can also provide multiple new sources of information. However, as a light scattering instrument was used to find several hydrothermal vents in the oceans on Earth [106], it is possible to use light scattering to decide on a safe spot for a lander and study the vents as well.

Assuming another satellite and not a lander, another recommendation is to put a full polarimeter on the spacecraft. That would drastically improve the resolution of the polarization data and reduce the noise. The Pioneer 10 spacecraft, which was launched in 1972 and lasted over 30 years, was the first spacecraft to travel past the asteroid belt. It had a full polarimeter present on the satellite, and was able to take the first up-close images and polarimetric data from Jupiter [107]. Even though Pioneer was launched 25 years before Cassini, it had better polarimetric resolution.

The second recommendation for a satellite flyby is to equip the satellite with a digital holography apparatus such as what was done to study Kansas fields [108]. Digital holography is currently underutilized in celestial contexts, and on Earth has been used for identifying biological weapons, pollen particles, different minerals, and types of air pollution [109], [110]. This would allow for images of the individual particles in the plumes for identification purposes. Digital holography allows for very quick snapshots of particles in-situ, without many of the issues that can happen with traditional photography. As holograms record the direction from which light came, as opposed to reducing the three dimensions of information into two dimensions like a typical photograph, full three-dimensional images of the particles can be taken. These can then be compared to a library of particle analogs from labs on Earth for plume particle identification.

7.3 Future Work

There is much that can be extrapolated from this project, as inverse problems have a near infinite number of possible solutions. Future work includes simulations varying more parameters than were discussed in this work. Only log-normal distributions were modelled here which can be expanded on as more knowledge of space particle distributions is gained. Also, the size ranges were limited due to computational resources, so larger ranges, possibly up to 100 μm can be useful. If the particles are made of crystalline ice and are that large, then it could be an effect of surface roughness [99]. Roughness has not been addressed in this work but could be a fascinating next step. The distributions here have had few changes to the mean and standard deviations, which appear to have a large impact on the results like the different geometries.

Also, other geometries such as Chebyshev particles can be simulated as a proxy for amorphous ice. The ice was assumed crystalline in this research, so testing Chebyshev particles can be helpful in identifying the plume particles. Also, other crystalline ice shapes may be simulated to account for different assumptions in where the plume particles freeze.

7.4 Summary of Contributions

In science, and this work is no exception, all work is based on the past accomplishments of others and would not be possible without their contributions. This section exists to restate the contributions of this work, and the new ideas presented heretofore.

1. The consideration of the mean anomaly's effect on particle intensity and the removal of the positional and particle-number dependence to use more of the Cassini intensity data than ever before.
2. The application of Q-space analysis to the plume particles, which set the average particle radius to be >2 μm and showed they are likely non-spherical due to the data having slopes not equal -2.

3. The analysis of the Cassini NAC polarization image data of Enceladus' surface, that before now, went untouched, showing that Enceladus has a relatively low DoLP of -7% to +7% for scattering angles of ~25° to ~165°.
    a. This is a much larger range of angles than can be studied from Earth-based telescopes due to geometry constraints.
    b. The DoLP is too low to be due to spherical particles, even with multiple scattering effects.
4. The expansion of light scattering simulations of the cryovolcano plume particles to shapes other than spheres and spheroids to now include cylinders and hexagonal prisms, and the application of said simulations to the surface DoLP.
    a. Using the Pearson correlation coefficient to compare the data and simulated curves, the particles are shown to be non-spherical, and possibly in size distributions wider than those tested in this work.
5. Recommendations for future missions to optimize the amount of data gathered and information learned based on the analysis in this paper and using light scattering techniques.

References

[1] J. Perlin, *Let It Shine: The 6,000-Year Story of Solar Energy*. New World Library, 2022.

[2] A. R. Jones, "Light scattering for particle characterization," *Progress in Energy and Combustion Science*, vol. 25, no. 1, pp. 1–53, Feb. 1999, doi: 10.1016/S0360-1285(98)00017-3.

[3] C. F. Bohren and D. R. Huffman, "Absorption and scattering of light by small particles," Jan. 1983. Accessed: Jun. 09, 2023. [Online]. Available: https://ui.adsabs.harvard.edu/abs/1983uaz..rept.....B

[4] J. C. Maxwell, "A Dynamical Theory of the Electromagnetic Field," *Philosophical Transactions of the Royal Society of London*, vol. 155, pp. 459–512, 1865.

[5] A. Lambert, "Dakar's urban pollution plume: A SAMUM-II case study on the plume structure and the influence of urban emissions on dust physico-chemical and radiative properties," 2011.

[6] G. G. Stokes, Ed., "On the Composition and Resolution of Streams of Polarized Light from different Sources," in *Mathematical and Physical Papers*, vol. 3, in Cambridge Library Collection - Mathematics, vol. 3. , Cambridge: Cambridge University Press, 1852, pp. 233–258. doi: 10.1017/CBO9780511702266.010.

[7] D. S. Kliger and J. W. Lewis, *Polarized Light in Optics and Spectroscopy*. Elsevier, 2012.

[8] "Polarization by Scattering." Accessed: Feb. 08, 2024. [Online]. Available: https://sciencedemonstrations.fas.harvard.edu/presentations/polarization-scattering

[9] C. M. Sorensen, *Light Scattering and Absorption by Particles: The Q-space approach*. IOP Publishing, 2022. Accessed: Feb. 01, 2024. [Online]. Available: https://iopscience.iop.org/book/mono/978-0-7503-5157-7

[10] R. A. West and P. H. Smith, "Evidence for aggregate particles in the atmospheres of Titan and Jupiter," *Icarus*, vol. 90, no. 2, pp. 330–333, Apr. 1991, doi: 10.1016/0019-1035(91)90113-8.

[11] M. I. Mishchenko, L. D. Travis, and A. A. Lacis, *Scattering, Absorption, and Emission of Light by Small Particles*. Cambridge University Press, 2002.

[12] M. G. Tomasko, L. R. Doose, L. E. Dafoe, and C. See, "Limits on the size of aerosols from measurements of linear polarization in Titan's atmosphere," *Icarus*, vol. 204, no. 1, pp. 271–283, Nov. 2009, doi: 10.1016/j.icarus.2009.05.034.

[13] H. C. van de Hulst, "Light scattering by small particles," *John Wiley and Sons*, vol. 84, no. 360, pp. 198–199, 1958, doi: 10.1002/qj.49708436025.

[14] G. Mie, "Beiträge zur Optik trüber Medien, speziell kolloidaler Metallösungen," *Annalen der Physik*, vol. 330, no. 3, pp. 377–445, 1908, doi: 10.1002/andp.19083300302.

[15] L. V. Lorenz, "Lysbevægelser i og uden for en af plane Lysbølger belyst Kugle," in *Det kongelige danske Videnskabernes Selskabs Skrifter*, 1890, pp. 1–62.

[16] J. R. Frisvad and H. Kragh, "On Ludvig Lorenz and his 1890 treatise on light scattering by spheres," *EPJ H*, vol. 44, no. 2, pp. 137–160, Aug. 2019, doi: 10.1140/epjh/e2019-100022-y.

[17] M. Abramowitz and I. A. Stegun, Eds., *Handbook of Mathematical Functions: with Formulas, Graphs, and Mathematical Tables*, 0009-Revised edition ed. New York, NY: Dover Publications, 1965.

[18] T. Väisänen, J. Martikainen, and K. Muinonen, “Scattering of light by dense particulate media in the geometric optics regime,” *Journal of Quantitative Spectroscopy and Radiative Transfer*, vol. 241, p. 106719, Jan. 2020, doi: 10.1016/j.jqsrt.2019.106719.

[19] C. M. Sorensen and D. J. Fischbach, “Patterns in Mie scattering,” *Optics Communications*, vol. 173, no. 1, pp. 145–153, Jan. 2000, doi: 10.1016/S0030-4018(99)00624-0.

[20] C. M. Sorensen, “Q-space analysis of scattering by particles: A review,” *Journal of Quantitative Spectroscopy and Radiative Transfer*, vol. 131, pp. 3–12, Dec. 2013, doi: 10.1016/j.jqsrt.2012.12.029.

[21] M. A. Yurkin and A. G. Hoekstra, “The discrete dipole approximation: An overview and recent developments,” *Journal of Quantitative Spectroscopy and Radiative Transfer*, vol. 106, no. 1, pp. 558–589, Jul. 2007, doi: 10.1016/j.jqsrt.2007.01.034.

[22] M. A. Yurkin and A. G. Hoekstra, “The discrete-dipole-approximation code ADDA: Capabilities and known limitations,” *Journal of Quantitative Spectroscopy and Radiative Transfer*, vol. 112, no. 13, pp. 2234–2247, Sep. 2011, doi: 10.1016/j.jqsrt.2011.01.031.

[23] M. A. Yurkin and A. G. Hoekstra, “User manual for the discrete dipole approximation code ADDA 1.4.0.” 2020. Accessed: Feb. 02, 2024. [Online]. Available: https://github.com/adda-team/adda/blob/master/doc/manual.pdf

[24] M. I. Mishchenko and P. A. Martin, “Peter Waterman and T-matrix methods,” *Journal of Quantitative Spectroscopy and Radiative Transfer*, vol. 123, pp. 2–7, Jul. 2013, doi: 10.1016/j.jqsrt.2012.10.025.

[25] Wolfram Research, Inc, “Mathematica.” Wolfram Research, Inc, 2023. [Online]. Available: https://www.wolfram.com/mathematica

[26] “LiteBil.” Accessed: Jan. 10, 2024. [Online]. Available: https://scattport.org/index.php/programs-menu/volume-integral-menu/418-litebil

[27] P. Laven, “MiePlot.” Accessed: Aug. 04, 2023. [Online]. Available: http://www.philiplaven.com/mieplot.htm

[28] R. A. West, P. Dumont, R. Hu, V. Natraj, J. Breckinridge, and P. Chen, “Spectropolarimetry as a Means to Address Cloud Composition and Habitability for a Cloudy Exoplanetary Atmosphere in the Habitable Zone,” *ApJ*, vol. 940, no. 2, p. 183, Dec. 2022, doi: 10.3847/1538-4357/ac9b42.

[29] “Log-Normal Distribution: Definition, Uses, and How To Calculate,” Investopedia. Accessed: Feb. 09, 2024. [Online]. Available: https://www.investopedia.com/terms/l/log-normal-distribution.asp

[30] “The Basics of Probability Density Function (PDF), With an Example,” Investopedia. Accessed: Feb. 08, 2024. [Online]. Available: https://www.investopedia.com/terms/p/pdf.asp

[31] “numpy.random.lognormal — NumPy v1.26 Manual.” Accessed: Feb. 08, 2024. [Online]. Available: https://numpy.org/doc/stable/reference/random/generated/numpy.random.lognormal.html

[32] “Enceladus,” NASA Solar System Exploration. Accessed: Jun. 09, 2023. [Online]. Available: https://solarsystem.nasa.gov/moons/saturn-moons/enceladus/in-depth

[33] A. Nakajima, S. Ida, J. Kimura, and R. Brasser, “Orbital evolution of Saturn’s mid-sized moons and the tidal heating of Enceladus,” *Icarus*, vol. 317, pp. 570–582, Jan. 2019, doi: 10.1016/j.icarus.2018.08.030.

[34] S. J. Peale, “Tidally Induced Volcanism,” *Celestial Mechanics and Dynamical Astronomy*, vol. 87, no. 1, pp. 129–155, Sep. 2003, doi: 10.1023/A:1026187917994.

[35] S. Vance *et al.*, “Distributed Geophysical Exploration of Enceladus and Other Ocean Worlds,” *Bulletin of the AAS*, vol. 53, no. 4, Mar. 2021, doi: 10.3847/25c2cfeb.a07234f4.
[36] C. C. Porco *et al.*, “Cassini Observes the Active South Pole of Enceladus,” *Science*, vol. 311, no. 5766, pp. 1393–1401, Mar. 2006, doi: 10.1126/science.1123013.
[37] T. W. Hill, “Saturn’s E ring,” *Advances in Space Research*, vol. 4, no. 9, pp. 149–157, Jan. 1984, doi: 10.1016/0273-1177(84)90020-6.
[38] C. Porco, D. DiNino, and F. Nimmo, “How the Geysers, Tidal Stresses, and Thermal Emission Across the South Polar Terrain of Enceladus are Related,” *AJ*, vol. 148, no. 3, p. 45, Jul. 2014, doi: 10.1088/0004-6256/148/3/45.
[39] C. J. Mitchell, C. C. Porco, and J. W. Weiss, “Tracking the Geysers of Enceladus into Saturn’s E-Ring,” *AJ*, vol. 149, no. 5, p. 156, Apr. 2015, doi: 10.1088/0004-6256/149/5/156.
[40] C. C. Porco, L. Dones, and C. Mitchell, “Could It Be Snowing Microbes on Enceladus? Assessing Conditions in Its Plume and Implications for Future Missions,” *Astrobiology*, vol. 17, no. 9, pp. 876–901, Sep. 2017, doi: 10.1089/ast.2017.1665.
[41] A. P. Ingersoll and S. P. Ewald, “Total particulate mass in Enceladus plumes and mass of Saturn’s E ring inferred from Cassini ISS images,” *Icarus*, vol. 216, no. 2, pp. 492–506, Dec. 2011, doi: 10.1016/j.icarus.2011.09.018.
[42] R. Jaumann *et al.*, “Distribution of icy particles across Enceladus’ surface as derived from Cassini-VIMS measurements,” *Icarus*, vol. 193, no. 2, pp. 407–419, Feb. 2008, doi: 10.1016/j.icarus.2007.09.013.
[43] J. H. Waite *et al.*, “Cassini Ion and Neutral Mass Spectrometer: Enceladus Plume Composition and Structure,” *Science*, vol. 311, no. 5766, pp. 1419–1422, Mar. 2006, doi: 10.1126/science.1121290.
[44] H.-W. Hsu *et al.*, “Ongoing hydrothermal activities within Enceladus,” *Nature*, vol. 519, no. 7542, Art. no. 7542, Mar. 2015, doi: 10.1038/nature14262.
[45] A. R. Hendrix and C. J. Hansen, “The surface composition of Enceladus: clues from the Ultraviolet,” *Proc. IAU*, vol. 5, no. S263, pp. 126–130, Aug. 2009, doi: 10.1017/S1743921310001626.
[46] A. J. Verbiscer *et al.*, “Near-infrared spectra of the leading and trailing hemispheres of Enceladus,” *Icarus*, vol. 182, no. 1, pp. 211–223, May 2006, doi: 10.1016/j.icarus.2005.12.008.
[47] B. R. Scharringhausen, “A Photometric Model of the Inclined F Ring of Saturn.” Cornell University, Jan. 2007. [Online]. Available: https://ecommons.cornell.edu/bitstream/handle/1813/3707/main.pdf?sequence=1&isAllowed=y
[48] A. P. Ingersoll, S. P. Ewald, and S. K. Trumbo, “Time variability of the Enceladus plumes: Orbital periods, decadal periods, and aperiodic change,” *Icarus*, vol. 344, p. 113345, Jul. 2020, doi: 10.1016/j.icarus.2019.06.006.
[49] D. W. Mackowski and M. I. Mishchenko, “A multiple sphere T-matrix Fortran code for use on parallel computer clusters,” *Journal of Quantitative Spectroscopy and Radiative Transfer*, vol. 112, no. 13, pp. 2182–2192, Sep. 2011, doi: 10.1016/j.jqsrt.2011.02.019.
[50] M. J. V. Kranendonk, V. Bennett, and H. R. H. Smithies, *Earth’s Oldest Rocks*. Elsevier, 2007.

[51] S. Hurwitz and M. Manga, "The Fascinating and Complex Dynamics of Geyser Eruptions," *Annu. Rev. Earth Planet. Sci.*, vol. 45, no. 1, pp. 31–59, Aug. 2017, doi: 10.1146/annurev-earth-063016-015605.

[52] "How Do Volcanoes Erupt? | U.S. Geological Survey." Accessed: Sep. 20, 2023. [Online]. Available: https://www.usgs.gov/faqs/how-do-volcanoes-erupt

[53] G. V. Tychnonis, *Astronomia nova Aitiologitis, seu Physica Coelestis tradita Commentariis de Motibus stellae Martis ex observationibus*. Prague: Engl. tr. W.H. Donahue, Cambridge, 16091992.

[54] "Orbital elements," *Wikipedia*. Jan. 11, 2024. Accessed: Jan. 12, 2024. [Online]. Available: https://en.wikipedia.org/w/index.php?title=Orbital_elements&oldid=1194857595

[55] "Mean anomaly," *Wikipedia*. Sep. 27, 2023. Accessed: Jan. 11, 2024. [Online]. Available: https://en.wikipedia.org/w/index.php?title=Mean_anomaly&oldid=1177361499#cite_note-1

[56] G. Filacchione *et al.*, "Saturn's icy satellites and rings investigated by Cassini–VIMS: III – Radial compositional variability," *Icarus*, vol. 220, no. 2, pp. 1064–1096, Aug. 2012, doi: 10.1016/j.icarus.2012.06.040.

[57] A. P. Ingersoll and S. P. Ewald, "Decadal timescale variability of the Enceladus plumes inferred from Cassini images," *Icarus*, vol. 282, pp. 260–275, Jan. 2017, doi: 10.1016/j.icarus.2016.09.018.

[58] T. A. Hurford, P. Helfenstein, G. V. Hoppa, R. Greenberg, and B. G. Bills, "Eruptions arising from tidally controlled periodic openings of rifts on Enceladus," *Nature*, vol. 447, no. 7142, Art. no. 7142, May 2007, doi: 10.1038/nature05821.

[59] J. Meyer and J. Wisdom, "Tidal evolution of Mimas, Enceladus, and Dione," *Icarus*, vol. 193, no. 1, pp. 213–223, Jan. 2008, doi: 10.1016/j.icarus.2007.09.008.

[60] A. Vienne and L. Duriez, "A general theory of motion for the eight major satellites of Saturn. III - Long-period perturbations," *Astronomy and Astrophysics*, vol. 257, pp. 331–352, Apr. 1992.

[61] J. Wisdom *et al.*, "Loss of a satellite could explain Saturn's obliquity and young rings." Accessed: Jun. 09, 2023. [Online]. Available: https://www.science.org/doi/10.1126/science.abn1234

[62] C. C. Porco *et al.*, "Cassini Imaging Science: Instrument Characteristics And Anticipated Scientific Investigations At Saturn," *Space Sci Rev*, vol. 115, no. 1, pp. 363–497, Nov. 2004, doi: 10.1007/s11214-004-1456-7.

[63] R. West *et al.*, "In-flight calibration of the Cassini imaging science sub-system cameras," *Planetary and Space Science*, vol. 58, no. 11, pp. 1475–1488, Sep. 2010, doi: 10.1016/j.pss.2010.07.006.

[64] W. Martin, J. Baross, D. Kelley, and M. J. Russell, "Hydrothermal vents and the origin of life," *Nat Rev Microbiol*, vol. 6, no. 11, Art. no. 11, Nov. 2008, doi: 10.1038/nrmicro1991.

[65] "Meet Orbilander, a Mission to Search for Life on Enceladus," The Planetary Society. Accessed: Sep. 11, 2023. [Online]. Available: https://www.planetary.org/articles/meet-orbilander-enceladus-mission

[66] W. Martin, J. Baross, D. Kelley, and M. J. Russell, "Hydrothermal vents and the origin of life," *Nat Rev Microbiol*, vol. 6, no. 11, Art. no. 11, Nov. 2008, doi: 10.1038/nrmicro1991.

[67] "Life at the hydrothermal vents | AMNH," American Museum of Natural History. Accessed: Jan. 09, 2024. [Online]. Available:

https://www.amnh.org/exhibitions/permanent/planet-earth/why-is-the-earth-habitable/life-that-lives-off-the-earth-s-energy/life-at-the-hydrothermal-vents

[68] G. Filacchione *et al.*, “Saturn’s icy satellites investigated by Cassini -- VIMS. V. Spectrophotometry,” *Icarus*, vol. 375, p. 114803, Mar. 2022, doi: 10.1016/j.icarus.2021.114803.

[69] P. Gao, P. Kopparla, X. Zhang, and A. P. Ingersoll, “Aggregate Particles in the Plumes of Enceladus,” *Icarus*, vol. 264, pp. 227–238, Jan. 2016, doi: 10.1016/j.icarus.2015.09.030.

[70] F. Nimmo, C. Porco, and C. Mitchell, “Tidally Modulated Eruptions on Enceladus: Cassini ISS Observations and Models,” *AJ*, vol. 148, no. 3, p. 46, Jul. 2014, doi: 10.1088/0004-6256/148/3/46.

[71] O. Poch, R. Cerubini, A. Pommerol, B. Jost, and N. Thomas, “Polarimetry of Water Ice Particles Providing Insights on Grain Size and Degree of Sintering on Icy Planetary Surfaces,” *J. Geophys. Res. Planets*, vol. 123, no. 10, pp. 2564–2584, Oct. 2018, doi: 10.1029/2018JE005753.

[72] P. Connolly *et al.*, “Aircraft observations of the influence of electric fields on the aggregation of ice crystals,” *Quarterly Journal of the Royal Meteorological Society*, vol. 131, no. 608, pp. 1695–1712, Apr. 2005, doi: 10.1256/qj.03.217.

[73] L. A. Raymond, *Petrology: The Study of Igneous, Sedimentary and Metamorphic Rocks*. Dubuque, IA: William C Brown Pub, 1995.

[74] F. Postberg *et al.*, “The E-ring in the vicinity of Enceladus: II. Probing the moon’s interior—The composition of E-ring particles,” *Icarus*, vol. 193, no. 2, pp. 438–454, Feb. 2008, doi: 10.1016/j.icarus.2007.09.001.

[75] S. W. Kieffer, X. Lu, G. McFarquhar, and K. H. Wohletz, “A redetermination of the ice/vapor ratio of Enceladus’ plumes: Implications for sublimation and the lack of a liquid water reservoir,” *Icarus*, vol. 203, no. 1, pp. 238–241, Sep. 2009, doi: 10.1016/j.icarus.2009.05.011.

[76] F. Scipioni *et al.*, “Deciphering sub-micron ice particles on Enceladus surface,” *Icarus*, vol. 290, pp. 183–200, Jul. 2017, doi: 10.1016/j.icarus.2017.02.012.

[77] B. S. Southworth, S. Kempf, and J. Spitale, “Surface deposition of the Enceladus plume and the zenith angle of emissions,” *Icarus*, vol. 319, pp. 33–42, Feb. 2019, doi: 10.1016/j.icarus.2018.08.024.

[78] M. M. Hedman *et al.*, “Photometric Analyses of Saturn’s Small Moons: Aegaeon, Methone, and Pallene Are Dark; Helene and Calypso Are Bright,” *AJ*, vol. 159, no. 4, p. 129, Apr. 2020, doi: 10.3847/1538-3881/ab659d.

[79] B. Jabaud, R. Artoni, G. Tobie, E. L. Menn, and P. Richard, “The icy regoliths of Enceladus and Europa : experimental and numerical study,” Copernicus Meetings, EPSC2022-466, Jul. 2022. doi: 10.5194/epsc2022-466.

[80] J. Tyndall, “IV. On the blue colour of the sky, the polarization of skylight, and on the polarization of light by cloudy matter generally,” *Proceedings of the Royal Society of London*, vol. 17, pp. 223–233, Jan. 1997, doi: 10.1098/rspl.1868.0033.

[81] Y. W. Heinson, J. B. Maughan, J. Ding, A. Chakrabarti, P. Yang, and C. M. Sorensen, “Q-space analysis of light scattering by ice crystals,” *Journal of Quantitative Spectroscopy and Radiative Transfer*, vol. 185, pp. 86–94, Dec. 2016, doi: 10.1016/j.jqsrt.2016.08.021.

[82] C. Sorensen, Y. Heinson, W. Heinson, J. Maughan, and A. Chakrabarti, “Q-Space Analysis of the Light Scattering Phase Function of Particles with Any Shape,” *Atmosphere*, vol. 8, no. 4, p. 68, Mar. 2017, doi: 10.3390/atmos8040068.

[83] S. G. Warren and R. E. Brandt, "Optical constants of ice from the ultraviolet to the microwave: A revised compilation," *J. Geophys. Res.*, vol. 113, no. D14, p. D14220, Jul. 2008, doi: 10.1029/2007JD009744.

[84] X. A. Zhang *et al.*, "Ordered 3D Thin-Shell Nanolattice Materials with Near-Unity Refractive Indices," *Advanced Functional Materials*, vol. 25, no. 42, pp. 6644–6649, 2015, doi: 10.1002/adfm.201502854.

[85] S. V. Zaitsev, N. N. Kiselev, V. K. Rosenbush, S. V. Kolesnikov, and D. N. Shakhovskoy, "Polarimetry of Saturnian satellite Enceladus," *Advances in Astronomy and Space Physics*, 2015.

[86] B. Knowles, R. West, P. Helfenstein, A. Verbiscer, D. Wilson, and C. Porco, "End-of-mission calibration of the Cassini Imaging Science Subsystem," *Planetary and Space Science*, vol. 185, p. 104898, Jun. 2020, doi: 10.1016/j.pss.2020.104898.

[87] SETI Institute, "Ring-Moon Systems Node Home." Accessed: Dec. 04, 2023. [Online]. Available: https://pds-rings.seti.org/

[88] H.-S. Chen and C. R. N. Rao, "Polarization of light on reflection by some natural surfaces," *J. Phys. D: Appl. Phys.*, vol. 1, no. 9, pp. 1191–1200, Sep. 1968, doi: 10.1088/0022-3727/1/9/312.

[89] M. Wolff, "Polarization of light reflected from rough planetary surface," *Appl. Opt., AO*, vol. 14, no. 6, pp. 1395–1405, Jun. 1975, doi: 10.1364/AO.14.001395.

[90] E. Zubko, G. Videen, N. Zubko, and Y. Shkuratov, "The Umov effect in application to an optically thin two-component cloud of cosmic dust," *Monthly Notices of the Royal Astronomical Society*, vol. 477, no. 4, pp. 4866–4873, Jul. 2018, doi: 10.1093/mnras/sty938.

[91] C. Morello and M. J. Berg, "A Light Scattering Analysis of the Cryovolcano Plumes on Enceladus," *Journal of Quantitative Spectroscopy and Radiative Transfer*, 2024.

[92] S. G. Warren and R. E. Brandt, "Optical constants of ice from the ultraviolet to the microwave: A revised compilation," *J. Geophys. Res.*, vol. 113, no. D14, p. D14220, Jul. 2008, doi: 10.1029/2007JD009744.

[93] A. Bravais, *Analyse mathématique sur les probabilités des erreurs de situation d'un point*. Impr. Royale, 1844.

[94] E. W. Weisstein, "Cross-Correlation." Accessed: Nov. 16, 2023. [Online]. Available: https://mathworld.wolfram.com/

[95] A. Penttilä and K. Lumme, "Optimal cubature on the sphere and other orientation averaging schemes," *Journal of Quantitative Spectroscopy and Radiative Transfer*, vol. 112, no. 11, pp. 1741–1746, Jul. 2011, doi: 10.1016/j.jqsrt.2011.02.001.

[96] J. G. van der Corput, "Proceedings of the section of sciences," *N.V. Noord-Hollandsche Uitgeversmaatschappi*, 1935.

[97] L. Kuipers, "Uniform distribution of sequences," *Pure and Applied Mathematics*, 1974, Accessed: Nov. 07, 2023. [Online]. Available: https://zbmath.org/?format=complete&q=an:0281.10001

[98] C. Morello and M. J. Berg, "Polarization Analysis of Enceladus' Surface," *Journal of Quantitative Spectroscopy and Radiative Transfer*, 2024.

[99] L. Bi and P. Yang, "Accurate simulation of the optical properties of atmospheric ice crystals with the invariant imbedding T-matrix method," *Journal of Quantitative Spectroscopy and Radiative Transfer*, vol. 138, pp. 17–35, May 2014, doi: 10.1016/j.jqsrt.2014.01.013.

[100] M. T. Lemmon *et al.*, “Hexagonal Prisms Form in Water-Ice Clouds on Mars, Producing Halo Displays Seen by Perseverance Rover,” *Geophys Res Lett*, vol. 49, no. 17, p. e2022GL099776, Sep. 2022, doi: 10.1029/2022GL099776.
[101] V. Kofman, J. He, I. L. ten Kate, and H. Linnartz, “The Refractive Index of Amorphous and Crystalline Water Ice in the UV–vis,” *ApJ*, vol. 875, no. 2, p. 131, Apr. 2019, doi: 10.3847/1538-4357/ab0d89.
[102] “Enceladus Orbilander | APL Civil Space.” Accessed: Sep. 11, 2023. [Online]. Available: https://space.jhuapl.edu/initiatives/enceladus-orbilander
[103] S. Kuthunur, “How Far Away Is Saturn? And, How Long Does It Take To Get There?” Accessed: Sep. 11, 2023. [Online]. Available: https://lovethenightsky.com/how-far-away-is-saturn/
[104] A. Berne, M. Simons, J. T. Keane, and R. S. Park, “Inferring the Mean Thickness of the Outer Ice Shell of Enceladus From Diurnal Crustal Deformation,” *Journal of Geophysical Research: Planets*, vol. 128, no. 6, p. e2022JE007712, 2023, doi: 10.1029/2022JE007712.
[105] J. R. Spencer *et al.*, “Cassini encounters Enceladus: background and the discovery of a south polar hot spot,” *Science*, vol. 311, no. 5766, pp. 1401–1405, Mar. 2006, doi: 10.1126/science.1121661.
[106] C. R. German *et al.*, “Hydrothermal plumes above the East Scotia Ridge: an isolated high-latitude back-arc spreading centre,” *Earth and Planetary Science Letters*, vol. 184, no. 1, pp. 241–250, Dec. 2000, doi: 10.1016/S0012-821X(00)00319-8.
[107] NASA, “The Pioneer Missions,” NASA. Accessed: Sep. 11, 2023. [Online]. Available: http://www.nasa.gov/centers/ames/missions/archive/pioneer.html
[108] O. Kemppinen, J. C. Laning, R. D. Mersmann, G. Videen, and M. J. Berg, “Imaging atmospheric aerosol particles from a UAV with digital holography,” *Sci Rep*, vol. 10, no. 1, Art. no. 1, Sep. 2020, doi: 10.1038/s41598-020-72411-x.
[109] J. A. Arnold, A. Kalume, H. Yu, C. L. Wirth, G. Videen, and Y.-L. Pan, “Measurements of elastic light-scattering patterns and images of single, oriented, optically trapped particles,” *Journal of Quantitative Spectroscopy and Radiative Transfer*, vol. 287, p. 108223, Sep. 2022, doi: 10.1016/j.jqsrt.2022.108223.
[110] R. Giri and M. J. Berg, “The color of aerosol particles | Scientific Reports,” *Scientific Reports*, 2022, Accessed: Sep. 11, 2023. [Online]. Available: https://www.nature.com/articles/s41598-023-28823-6

Appendix A - Images Used in Polarization Analysis

Image names: Cassini ISS NAC GRN

P0	P60	P120
co-iss-n1487334437	co-iss-n1487334509	co-iss-n1487334581
co-iss-n1487334751	co-iss-n1487334791	co-iss-n1487334831
co-iss-n1696148154	co-iss-n1696148187	co-iss-n1696148220
co-iss-n1484578175	co-iss-n1484578208	co-iss-n1484578241
co-iss-n1656975401	co-iss-n1656975434	co-iss-n1656975467
co-iss-n1867018939	co-iss-n1867018972	co-iss-n1867019005
co-iss-n1489087420	co-iss-n1489087453	co-iss-n1489087486
co-iss-n1606891864	co-iss-n1606891897	co-iss-n1606891930
co-iss-n1584036191	co-iss-n1584036246	co-iss-n1584036301
co-iss-n1606884842	co-iss-n1606884875	co-iss-n1606884908
co-iss-n1820444440	co-iss-n1820444473	co-iss-n1820444506
co-iss-n1604151971	co-iss-n1604152004	co-iss-n1604152037
co-iss-n1602264220	co-iss-n1602264253	co-iss-n1602264286
co-iss-n1597176014	co-iss-n1597176047	co-iss-n1597176080
co-iss-n1484532637	co-iss-n1484532670	co-iss-n1484532703
co-iss-n1820439524	co-iss-n1820439557	co-iss-n1820439590
co-iss-n1569843427	co-iss-n1569843482	co-iss-n1569843537
co-iss-n1862049045	co-iss-n1862049078	co-iss-n1862049111
co-iss-n1593502265	co-iss-n1593502324	co-iss-n1593502384
co-iss-n1597222447	co-iss-n1597222480	co-iss-n1597222513
co-iss-n1602294702	co-iss-n1602294735	co-iss-n1602294768
co-iss-n1569849963	co-iss-n1569850018	co-iss-n1569850073
co-iss-n1604187027	co-iss-n1604187060	co-iss-n1604187093
co-iss-n1604181768	co-iss-n1604181801	co-iss-n1604181834
co-iss-n1597197052	co-iss-n1597197085	co-iss-n1597197118
co-iss-n1484519362	co-iss-n1484519395	co-iss-n1484519428
co-iss-n1602286467	co-iss-n1602286500	co-iss-n1602286533
co-iss-n1597194538	co-iss-n1597194571	co-iss-n1597194604
co-iss-n1600380688	co-iss-n1600380721	co-iss-n1600380754
co-iss-n1584052989	co-iss-n1584053044	co-iss-n1584053099
co-iss-n1855839066	co-iss-n1855839099	co-iss-n1855839132
co-iss-n1855840729	co-iss-n1855840762	co-iss-n1855840795
co-iss-n1855842144	co-iss-n1855842177	co-iss-n1855842210
co-iss-n1824727844	co-iss-n1824727877	co-iss-n1824727910
co-iss-n1489029729	co-iss-n1489029762	co-iss-n1489029795
co-iss-n1500051292	co-iss-n1500051325	co-iss-n1500051358
co-iss-n1637479767	co-iss-n1637479800	co-iss-n1637479833
co-iss-n1500046660	co-iss-n1500046693	co-iss-n1500046726
co-iss-n1500041260	co-iss-n1500041293	co-iss-n1500041326
co-iss-n1516171123	co-iss-n1516171140	co-iss-n1516171157

co-iss-n1660446226	co-iss-n1660446243	co-iss-n1660446260
co-iss-n1516170018	co-iss-n1516170051	co-iss-n1516170084
co-iss-n1823501712	co-iss-n1823501745	co-iss-n1823501778
co-iss-n1710060177	co-iss-n1710060210	co-iss-n1710060243
co-iss-n1696191350	co-iss-n1696191383	co-iss-n1696191416
co-iss-n1561728566	co-iss-n1561728601	co-iss-n1561728636

Table A.1. The list of images used in this work for the DoLP analysis for Cassini's NAC GRN filter (0.569 μm) as shown in Fig. 4.2. There are 46 sets of 3 images.

Image names: Cassini ISS NAC UV3

P0	P60	P120
co-iss-n1484578046	co-iss-n1484578094	co-iss-n1484578142
co-iss-n1694598465	co-iss-n1694598543	co-iss-n1694598621
co-iss-n1489088933	co-iss-n1489088981	co-iss-n1489089029
co-iss-n1867018793	co-iss-n1867018849	co-iss-n1867018905
co-iss-n1489087291	co-iss-n1489087339	co-iss-n1489087387
co-iss-n1584025552	co-iss-n1584025622	co-iss-n1584025692
co-iss-n1606891735	co-iss-n1606891783	co-iss-n1606891831
co-iss-n1584035896	co-iss-n1584035966	co-iss-n1584036086
co-iss-n1604151842	co-iss-n1604151890	co-iss-n1604151938
co-iss-n1820444295	co-iss-n1820444351	co-iss-n1820444407
co-iss-n1602264025	co-iss-n1602264095	co-iss-n1602264165
co-iss-n1597176152	co-iss-n1597176224	co-iss-n1597176296
co-iss-n1484532524	co-iss-n1484532564	co-iss-n1484532604
co-iss-n1820439395	co-iss-n1820439443	co-iss-n1820439491
co-iss-n1862048900	co-iss-n1862048956	co-iss-n1862049012
co-iss-n1604181639	co-iss-n1604181687	co-iss-n1604181735
co-iss-n1484519249	co-iss-n1484519289	co-iss-n1484519329
co-iss-n1597194652	co-iss-n1597194700	co-iss-n1597194748
co-iss-n1584053169	co-iss-n1584053239	co-iss-n1584053309
co-iss-n1824727958	co-iss-n1824728006	co-iss-n1824728054
co-iss-n1500051163	co-iss-n1500051211	co-iss-n1500051259
co-iss-n1500046774	co-iss-n1500046822	co-iss-n1500046892
co-iss-n1500041374	co-iss-n1500041422	co-iss-n1500041470
co-iss-n1516170124	co-iss-n1516170186	co-iss-n1516170248
co-iss-n1699260605	co-iss-n1699260675	co-iss-n1699260745
co-iss-n1696186883	co-iss-n1696186931	co-iss-n1696186979
co-iss-n1710060048	co-iss-n1710060096	co-iss-n1710060144
co-iss-n1710055824	co-iss-n1710055872	co-iss-n1710055920
co-iss-n1696191221	co-iss-n1696191269	co-iss-n1696191317
co-iss-n1561728678	co-iss-n1561728707	co-iss-n1561728736

Table A.2. The same as Table A.1 but for Cassini's NAC UV3 filter (0.343 μm). There are 30 sets of 3 images.

Image names: Cassini ISS NAC MT2

P0	P60	P120
co-iss-n1484578289	co-iss-n1484578337	co-iss-n1484578385
co-iss-n1489089176	co-iss-n1489089224	co-iss-n1489089272
co-iss-n1489088355	co-iss-n1489088403	co-iss-n1489088451
co-iss-n1489087534	co-iss-n1489087582	co-iss-n1489087630
co-iss-n1606891978	co-iss-n1606892026	co-iss-n1606892074
co-iss-n1602264334	co-iss-n1602264382	co-iss-n1602264430
co-iss-n1597176368	co-iss-n1597176440	co-iss-n1597176512
co-iss-n1484532751	co-iss-n1484532799	co-iss-n1484532847
co-iss-n1604187141	co-iss-n1604187189	co-iss-n1604187237
co-iss-n1484519468	co-iss-n1484519516	co-iss-n1484519564
co-iss-n1604181882	co-iss-n1604181930	co-iss-n1604181978
co-iss-n1597194796	co-iss-n1597194844	co-iss-n1597194892
co-iss-n1600380835	co-iss-n1600380883	co-iss-n1600380931
co-iss-n1584053379	co-iss-n1584053449	co-iss-n1584053519
co-iss-n1489029835	co-iss-n1489029897	co-iss-n1489029967
co-iss-n1824728235	co-iss-n1824728283	co-iss-n1824728331
co-iss-n1500051398	co-iss-n1500051446	co-iss-n1500051494
co-iss-n1637479881	co-iss-n1637479929	co-iss-n1637479977
co-iss-n1500046962	co-iss-n1500047010	co-iss-n1500047058
co-iss-n1500041518	co-iss-n1500041566	co-iss-n1500041614
co-iss-n1516170310	co-iss-n1516170372	co-iss-n1516170434
co-iss-n1561728765	co-iss-n1561728794	co-iss-n1561728823

Table A.3. The same as Table A.1 but for Cassini's NAC MT2 filter (0.727 μm). There are 22 sets of 3 images.